ABSTRACT

PARTICLE RESPONSE FUNCTION IN SAMARIUM AND EUROPIUM ISOTOPES

By

James Edward Duffy

The reactions (α,t) and (α,^{3}He) have been performed with 100-MeV α-particles on targets of ^{144,148,152,154}Sm to investigate high lying proton strength distribution in ^{145,149,153,155}Eu and neutron strength distribution in ^{145,149,153,155}Sm, respectively. The emitted particles were identified in the S-320 spectrograph using two ΔE gas counters and an E plastic scintillator. Some differences were observed in the spectra depending on the nuclear deformation. Strong transitions to high-lying proton and neutron states up to about 15 MeV excitation energy were observed. Angular distributions were measured from 2° to 25° for both (α,t) and (α,^{3}He) reactions. The extreme forward angle data points were necessary to determine the ℓ-transfers. A smooth background, calculated using the α-breakup model, was subtracted from the spectra for

excitation energies above 3 MeV. The background-subtracted spectra were divided into 520-keV wide bins and the angular distribution for each bin was fitted with DWBA calculations to obtain a strength distribution for each ℓ-value. The excitation energies, angular distributions, and strengths of the high-lying transitions suggest that they arise from proton and neutron stripping to high-spin outer subshells, e.g. $1h_{9/2}$ and $1i_{13/2}$ in ^{145,149,153,155}Eu and $1h_{9/2}$, $1i_{13/2}$ and $1j_{15/2}$ in ^{145,149,153,155}Sm. The deduced proton and neutron strength distributions are compared with predictions from the quasiparticle-phonon model and the interacting boson-fermion approximation model.

PARTICLE RESPONSE FUNCTION IN SAMARIUM AND EUROPIUM ISOTOPES

By

James Edward Duffy

A DISSERTATION

Submitted to
Michigan State University
in partial fulfillment of the requirements
for the degree of

DOCTOR OF PHILOSOPHY

Department of Physics and Astronomy

1986

To my wife

Andrea Rose Micallef

ACKNOWLEDGMENTS

I would like to thank my advisor Gary Crawley for his guidance and direction. His constant support and inspiration provided the insight necessary to complete this Thesis.

I would also like to thank Raman Anantaraman for his charitable time and friendship.

There are several people to whom I owe acknowledgement: for serving on my committee, Aaron Galonsky and Alex Brown; for their recomendations regrding to this thesis topic, Sydney Galès, Patricia Massolo, V.G. Soloviev, Olaf Scholten and George Bertsch; members of the computer group, Barbara Pollack, Ron Fox, Skip Vandermolen, Lori Fedewa and Richard Au; for members of the mechanical design group, Mike Fowler, Al Gavalya and Craig Snow; Gary Westfall, who provided emotional support; and those individuals who participated and volunteered long hours to assist in my experiments, Hans van der Plicht, Bob Tickle, John Winfield, Joe Finck and Silvana Angius; and to the dedicated staff, students and faculty of the NSCL.

With any project one endeavors, there are those individuals whose professional affiliation evolves into a social association. Special thanks for the many times

shared with racketball buddies Don Lawton and Jack Ottarson. Through Pacman and prelims, marrage and moving, for countless fond memories I thank Mark, Mary, Mike and Pat Curtin. Many thanks to Virginia Crawford, Ellen Prost and Tom Warren. Lastly, much love and appreciation to my parents James and Rosemary Duffy, my wife's parents Vincent and Claudette Micallef and my loving wife Andrea Micallef.

TABLE OF CONTENTS

LIST OF TABLES

LIST OF FIGURES

CHAPTER I

INTRODUCTION

The study of elementary modes of excitation, particularly in many-body systems, is of great interest in several areas of physics. In nuclear physics, there are numerous examples of such simple structures, including isobaric analogue states, giant resonances and single-particle and single-hole states. The concept of single-particle motion in the mean field of the nucleus is perhaps the most fundamental idea in nuclear structure physics and is the basis for the highly successful nuclear shell model.

Experimentally, single-nucleon transfer reactions [Au70] have been the probes most extensively used to study the properties of single-particle and single-hole states. These reactions are of two types: stripping and pickup. In stripping, a nucleon is transferred from the projectile to an unoccupied single-particle state in the target, thereby probing the distribution of particle strength in the final nucleus. In pickup, a nucleon is transferred to the projectile from an occupied state in the target, thereby probing the distribution of hole strength in the final nucleus.

Since the early 1960's, many single-nucleon transfer reaction studies have been performed on nuclei throughout the periodic table, with low energy light-ion projectiles (p, d, t, ^{3}He, ^{4}He), to examine low excitation energies (less than 5 MeV) of the nucleus. Only recently, with the help of higher energy beams, have such studies been extended to explore single-particle and single-hole strength at higher excitation energies. This Thesis describes the investigation of single-particle states at high excitation energies (up to 15 MeV) in a set of samarium isotopes whose shapes range from spherical to deformed, using the (α,t) and (α,^{3}He) reactions. The α-particle beam was chosen because it provides the lightest projectile with which both proton and neutron stripping can be studied using the methods of charged-particle spectroscopy.

In this Chapter, the techniques that have been developed over the years to investigate particle and hole states by means of single-nucleon transfer reactions will first be presented. Next, brief reviews of the results of pickup and stripping reactions on medium-heavy targets will be given, including the use of nuclear structure models to understand the results. Finally, the goals of this Thesis -- the investigation of particle states in the samarium isotopes -- will be discussed.

In reality, nuclear states are seldom true single-particle states. Most commonly, as sketched in Figure I.1, a given single-particle (or single-hole) excitation spreads over many states of the final nucleus. Transfer reactions then study the distribution of the single-particle strength over a finite energy interval. Such mixing of simple states with more complicated underlying states is a problem even at low excitation energies, and it becomes worse with increasing excitation.

In a single-nucleon transfer reaction, each state in the final nucleus is populated with a strength proportional to the square of the amplitude of the single-particle component of that state. This strength is usually expressed in terms of the spectroscopic factor S for that state. The precise mathematical definition of S will be given in Chapter III, in equation (III.13). Qualitatively, the spectroscopic factor $S_{n\ell j}$ for a state $|J_B, M_B\rangle$ in the residual nucleus B, of angular momentum J_B, is the probability that $|J_B, M_B\rangle$ "looks like" the target ground state $|J_A, M_A\rangle$ plus a particle p (or hole) in the single particle state $|n\ell j\rangle$. Here B=A+p. The angular momenta satisfy the relation $\vec{J}_B = \vec{J}_A + \vec{j}$.

The technique used to extract the spectroscopic factor S of a state is the following. From spectra taken at various angles, the experimental angular distribution for

<u>Figure I.1</u>

Fragmentation of a single-particle excitation.

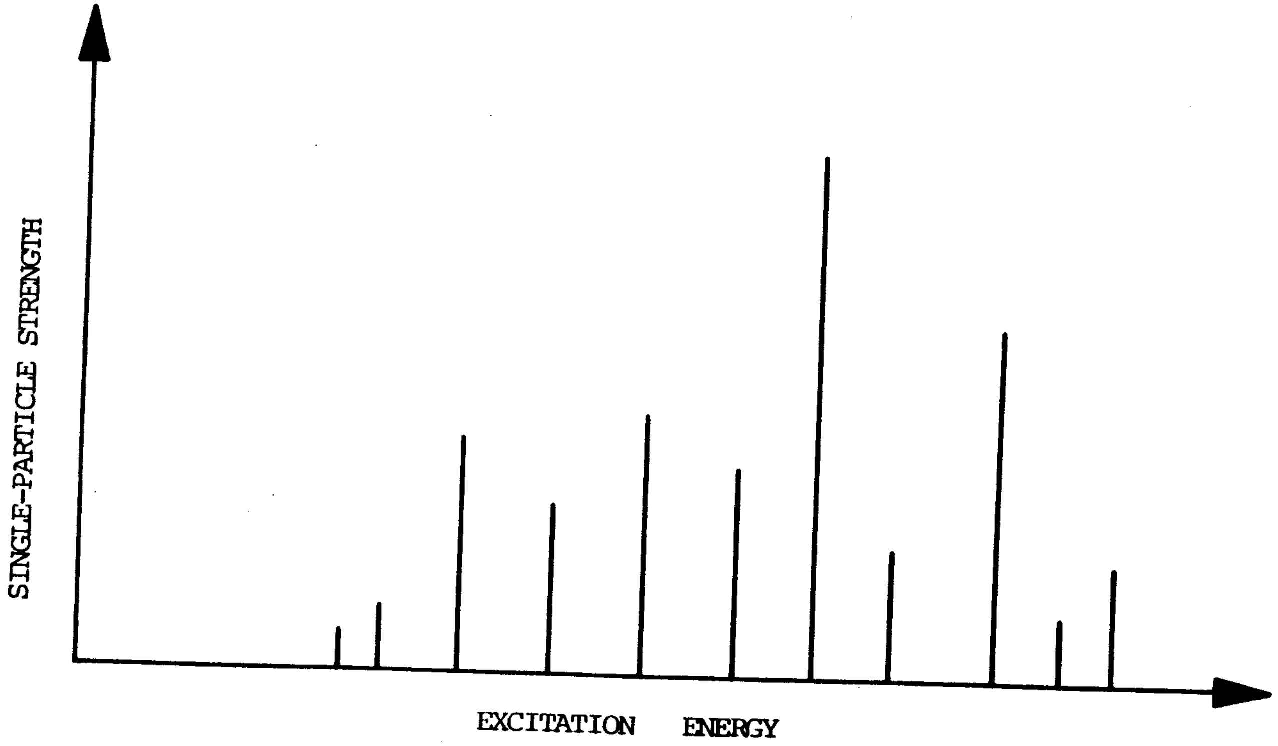

Figure I.1

the state is obtained. It is characteristic of the orbital angular momentum (ℓ) of the transferred particle; the j must be inferred from other considerations, such as the use of polarized beams. This angular distribution is compared with a theoretical one calculated in the Distorted Wave Born Approximation (DWBA) in which it is assumed that the entire spectroscopic strength is concentrated in that one state. The ratio of the experimental to the theoretical angular distribution then gives the actual S for that state. By studying different states, the distribution of S is mapped out. At higher excitation energies the level density becomes so large that individual states cannot be resolved in the transfer reactions. It is still possible to study the single-particle (and single-hole) excitations by the envelope of the strength distribution, which appears as a broad bump in a low resolution experiment. The details of this procedure and its uncertainties are discussed in Chapters III and IV.

This distribution of S as a function of excitation energy in the final nucleus contains a lot of nuclear structure information. The *centroid* of the distribution, for all fragments $|J_B,M_B\rangle$ of a given single-particle (or single-hole) excitation $|n\ell j\rangle$, gives the energy of that excitation. The *width* of the distribution is a measure of the spreading of the single-particle (or single-hole) excitation. The *sum* of the spectroscopic factors of all fragments of a given single-particle (or single-hole) excitation measures the extent to which that excitation is empty (or occupied) in the target ground state.

The total width of a nuclear state is the sum of two parts: the decay width and the spreading width. The decay width or escape width of a state is a measure of the probability that the state decays to a lower energy state either in the same nucleus (by γ emission) or in another nucleus (by particle emission). The spreading width is the probability that the state decays through the development of more complex excitations such as vibrational states, compound nuclear states, etc. In this mixing, the angular momentum of the initial single-particle is preserved: a state of angular momentum j mixes only with background states having the same total angular momentum.

When the lifetime of a state is known, its decay width can be easily calculated using the uncertainty principle. This is given by the following.

$$\Gamma = \frac{\hbar}{t} = \frac{\hbar c}{ct} = \frac{197\ (\mathrm{MeV\ \ fm})}{3\times 10^{23}(\mathrm{fm/sec})\times t(\mathrm{sec})} \qquad (\mathrm{I.1})$$

Here t is the mean lifetime in seconds, which is related to the half life by the expression $t=1.44t_{1/2}$.

In this Thesis, we shall concentrate on the spreading width of the single-particle excitation, which is measured by the width of the distribution of all the complex states (shown in Figure I.1) into which the excitation fragments.

Each of these complex states has a width which arises from its decay to lower-lying states (the decay width). When the state is bound with respect to particle emission so that it decays only by γ-ray emission, it has a negligible decay width. For example, the first excited state of ^{145}Sm has a half life of 36×10^{-12} seconds [Tu80] and decays by γ-ray emission to the ground state with an energy of 0.883 MeV. Its decay width, calculated using equation (I.1), is 1.3×10^{-8} keV. When the state is unbound with respect to particle emission, the decay width is much larger. It depends on the energy available for the decay, on the angular momentum in the decay channel, and on whether the decay is by proton or neutron emission, and can be estimated by performing a potential barrier penetration calculation. Normally, the decay is by neutron emission, since the Coulomb barrier inhibits charged particle emission. A typical value [Be86] for the single-particle decay width ($\Gamma_{s.p.}$) is 1 MeV when the decay energy is a few MeV. The decay width for any of the individual complex states will be reduced from this value depending on its spectroscopic factor, and may typically be 0.1 MeV for an unbound state. The spreading width for the single-particle excitation, on the other hand, is typically several MeV. Thus, for the situation of interest to us, the decay width can be ignored in comparison with the spreading width.

Many light ions at different incident energies have been used in pickup reactions, such as (p,d) and (^{3}He,α), to investigate single-hole strength in medium - heavy nuclei [G1-1]. The beam energies have ranged from about 22 MeV for deuterons [Co69] to 283 MeV for ^{3}He [La82]. Some of the studies have involved polarized proton beams and the use of the $(\vec{p},d)$ reaction [Cr80]. Deep-lying neutron-hole states, i.e. neutron orbits deeply bound below the Fermi surface, in different isotopes of Zr, Sn, Sm and Pb have been studied by means of the (p,d) reaction at 42 MeV [Ga81] and the (^{3}He,α) reaction at 70 MeV [Ga83]. These studies probed neutron-hole strength in the excitation energy range from about 4 to 15 MeV. Also the ^{90}Zr$(\vec{p},d)^{89}$Zr reaction [Cr80] was used to extract the j-values of deep hole states using analyzing power measurements.

In all these cases, an underlying background was found in the spectra. In most cases, the background was drawn by hand to connect low points in the spectra. This rather arbitrary method led to uncertainties in the experimental cross sections, which were usually obtained by assuming specific peak shapes for gross structures. A series of different gaussian shapes spanned the entire energy region of the background-subtracted spectra and experimental cross sections were calculated using these gaussian shapes. Experimental angular distributions were plotted and compared with the theoretical angular distributions to yield the amount of strength for an individual ℓ-transfer in that energy region. The strengths of various ℓ-transfers were then calculated for the complete energy spectrum.

This gave the spreading of strength of deep hole states in medium and heavy nuclei over the excitation energy range investigated experimentally. Attempts were then made to understand the reasons for this spreading, by comparing the observed strength distribution with theoretical models. Such comparisons show that, at low excitation energies, the only important source of the spreading of single-hole states is the coupling to surface vibrations; the single-hole (and single-particle) mode decays by exciting these vibrations [Be79,So80,Be83a,Be83b,Sc85]. At higher excitation energies, the nucleons in the interior of the nucleus absorb energy more effectively from the simple modes. A model commonly used to treat this behavior is the quasi-particle phonon model [So80], which considers mixing with both low-lying and high-lying phonon states.

The hole state results for the samarium isotopes with neutron number larger than N=82 show a picture that is different from the one seen in the Cd, Pd, Sn and Te isotopes [Ga81,Sc80,We77,Ge80,Ga82a]. They show that the disappearance of the N=82 shell gap, as the deformation increases, leads to overlapping of the $h^{-1}_{11/2}$ hole strength with the strengths corresponding to the lower subshells, $2d^{-1}_{5/2}$ and $1g^{-1}_{9/2}$.

Since background subtraction in hole state analysis is a difficult problem, the more complicated particle-gamma coincidence reaction (^{3}He,$\alpha\gamma$) was carried out on targets of ^{102,106,108}Pd and ^{112,118}Sn using a 70-MeV beam of ^{3}He particles [Sa81,Sa85]. Here it was found that a large fraction of the $g_{9/2}^{-1}$ hole state strength in ^{101}Pd occurred as a single state at E_x= 2.396 MeV with a width of 2.5 keV. The remaining $g_{9/2}^{-1}$ strength occurred in a 1-MeV wide bump at about 4 MeV excitation energy, which decayed statistically.

The information obtained from the extensive measurements of deep-lying hole states in nuclei is useful both because it helps in the development of models of nuclear structure and because the empirical values of the position and the width of particular hole states can be used as input for predictions of other nuclear phenomena such as giant resonances. Giant resonances are simple, usually collective excitations in nuclei which are excited in inelastic scattering processes as a superposition of particle - hole states [Be79]. In order to calculate their position and spreading width, information on the individual hole and particle states is useful [Be83a].

We next turn to measurements of the particle strength. This provides valuable information which is complementary to that on the hole strength. While it is possible to obtain information on hole states from knockout reactions like (p,2p), there are no analogous reactions to populate particle states. Such states are generally studied by stripping reactions. (If the state is unbound, it can also be studied by the direct scattering of nucleons, but this technique is useful only over a limited range of excitation energies.) Unlike the situation with deep-hole states, until recently there has been little or no comparable information on highly excited particle states in medium and heavy nuclei [G1-2]. Understanding the potential of stripping reactions to provide information on high-lying particle states is an additional important motivation of this work.

Studies of particle states in spherical nuclei were recently carried out at Orsay [Ga82b,Ga83,Ga85a,b]. The stripping reactions used were ^{90}Zr, ^{120}Sn, ^{144}Sm, ^{208}Pb(^{3}He,d) and ^{120}Sn, ^{144}Sm, ^{208}Pb(α,t) for proton particle states and ^{90}Zr, ^{120}Sn, ^{208}Pb(α,^{3}He) for neutron particle states. A 240 MeV beam of ^{3}He particles and 80 MeV and 183 MeV beams of α particles were used to investigate particle state strength from about 4 to 15 MeV of excitation energy. The techniques used were essentially similar to those used to analyze the hole state strength [Ga81,Ga82a], but with some differences.

Two of the differences were the use of a plane wave breakup calculation to predict the underlying background and of a "slicing" method instead of the gaussians to extract the cross sections. The plane wave breakup calculation reproduced the spectral cross section at high excitation energy for the 240 MeV ^{3}He and 183 MeV α particle beam cases but failed to do so for the 80 MeV α induced reactions. This was later found to be due to the fact that the 80 MeV α

beam energy is too low for the plane-wave approximation to be valid, and so an empirical solution was developed using the shape of the breakup calculation.

Experimental cross sections were deduced using gaussian shaped peaks for the case of the 240 MeV ^{3}He beam and using both gaussian shaped peaks and "slicing" the corrected spectra into bins for the 80 MeV and 183 MeV α particle beams. Experimental angular distributions were obtained using both the gaussian shapes and the "sliced" bins. Comparisons of the experimental and theoretical (DWBA) angular distributions yielded the amount of strength which each individual ℓ-transfer had in a particular energy region. The strengths of various ℓ-transfers were obtained for the complete energy spectrum measured.

The strength distributions were compared with theoretical models, in particular the quasi-particle phonon model [So80,St83]. These comparisons suggested that the spreading of states is due to surface vibrations interacting with the particle states in spherical nuclei, similar to the mechanism for the hole states.

The present work is an extension of such particle-strength studies to deformed nuclei, for which no information on high-lying particle strength has been available until now. Since the spreading of the states is predicted to depend on the phonon structure of the nucleus, studies of deformed nuclei, in which the phonon structure is quite different from that in spherical nuclei, provide a useful test of the theory. In addition, this will also provide us with a complete set of both proton and neutron particle states for an isotope chain that changes its phonon structure. We elected to use the even-even samarium isotopes as targets because they range from spherical, as in the ^{144}Sm case, to very deformed, as in ^{154}Sm. The deformation of the samarium isotopes, estimated from the variation of the B(E2) values of the first 2^+ state in these nuclei, ranges from $\beta_2=0.0$ for ^{144}Sm to $\beta_2=0.27$ for ^{154}Sm [Go72].

The goal of this investigation is to obtain information on the single particle strength distribution as a function of the deformation of the target nucleus. The overlapping of high lying proton strength distributions will be compared with the lower energy work mentioned above, for the spherical nucleus ^{144}Sm. Finally, comparisons of data to theory, will be carried out where possible.

This Thesis is divided into six chapters and two appendices. Chapter II: The experimental procedure that was used to obtain the stripping data is discussed. With a beam of 100-MeV α particles, the stripping reactions (α,t) and (α,^{3}He) were used to investigate the proton and neutron particle states, respectively, in the isotopes of samarium. Targets of ^{144,148,152,154}Sm were used. The α-particle energy (100 MeV) was selected to be high enough to excite high ℓ-transfers.

Chapter III: A presentation of the DWBA theory is given in this chapter.

Chapter IV: This chapter explains the technique used to extract spectroscopic information from the stripping reaction data. First, a background is calculated and subtracted from the spectra. The background is taken to consist of two parts: a breakup part, calculated in the plane wave model, and a compound nuclear emission part. Next, a "slicing" technique is used on the background-subtracted spectra to extract the experimental cross sections.

Chapter V: Experimental angular distributions are plotted and compared with the theoretical DWBA calculations to yield the strength. The results obtained using this technique are presented.

Chapter VI: The experimental results are compared with the theoretical calculations that exist for five of the eight final nuclei studied here. The conclusions of this investigation are also presented.

Appendix I: This appendix lists the (α,t) and $(\alpha,{}^3He)$ cross sections as a function of angle for the low lying states populated in the reactions on

^{144}Sm and ^{208}Pb, the low lying peaks populated in the reactions on ^{148,152,154}Sm and the elastic scattering cross sections for ^{144,148,152,154}Sm(α,α).

Appendix II: This appendix outlines, in an algorithm style format, two of the main programs developed for this Thesis: the calibration program SPECCAL and the analysis program SMASHER. Sample input files to run these and other programs used in this Thesis are also given.

CHAPTER II

EXPERIMENTAL PROCEDURE

The measurements of (α,t) and (α,^{3}He) reactions described in this Thesis were carried out using an α-particle beam from the K500 cyclotron at the National Superconducting Cyclotron, Michigan State University. The experiment required three runs which spanned about one and a half years. During this time many improvements in the data taking system were developed. Specific changes in the detector equipment and the data acquisition system will be referred to throughout this Chapter.

II.1 EXPERIMENTAL SETUP

The beam energy used was 100 MeV, with beam intensities on target ranging from 25 to 200 particle nanoamperes. The targets used were 0.88 mg/cm^2 Mylar $(C_{10}H_8O_4)_n$, 1.0 mg/cm^2 ^{144}Sm (96.47% isotopic enrichment), 3.0 mg/cm^2 ^{148}Sm (90.70%), 4.7 mg/cm^2 ^{152}Sm (98.29%), 3.9 mg/cm^2 ^{154}Sm (98.69%) and 6.0 mg/cm^2 ^{208}Pb. The samarium targets were purchased from the company Micromatter, Inc. of Seattle, Washington. Elastic cross sections were used to obtain the thicknesses of the Sm targets. The elastic cross section measurements were carried out at lab angles of 2°, 4° and 6° using the 100 MeV α-beam. The calculated elastic to Rutherford scattering cross section ratio using the code DWUCK4 [Ku69] has values of 1.01, 1.02 and 1.14, respectively, at lab angles of 2°, 4° and 6° for ^{144}Sm and similar values for the other three targets. The target thicknesses were determined by matching the calculated to the measured cross sections. Uncertainties in the target thickness for the samarium isotopes ^{144,148,152,154}Sm are respectively 7%, 7%, 20% and 6%. The measurement for ^{152}Sm has the largest uncertainty because the cross section at one of the angles (4°) was about 20% above the fitted theoretical angular distribution curve, making the normalization uncertain.

The stripping cross section measurements were carried out at lab angles from 2° to 25°, generally in 1° to 2° steps at the forward angles (below 9°) and in 3° steps at the backward angles (above 11°). The energy resolution of our experiment was limited by the S320 spectrograph system and not by the target thicknesses. The resolution was tested using the elastic peak in the focal plane of the S320 spectrograph. Adjustments of the x-quadrupole, sextupole and octupole magnets, the gas pressure in the focal plane detector, and the electronic gains were carried out with the elastic peak at various positions in the focal plane of the spectrograph, to achieve the best resolution possible. This was found to be 280 keV at small angles and up to 320 keV at the larger angles for the (α,t) reactions. A somewhat better resolution ($\approx$200keV) was found for the (α,^{3}He) reactions, probably because the extrapolation of the spectrometer parameters from the elastic scattering settings was smaller in this case than in the (α,t) case.

The tritons and ^{3}He particles were detected in the focal plane of the S320 spectrograph. A view of this spectrograph is given in Figure II.1 [Be83b]. The S320 system consists of a scattering chamber, the five magnets of the spectrograph (two quadrupoles, a dipole, an octupole, and a sextupole) and a focal plane detector. One quadrupole focuses in the y-direction and the other in the x-direction. The dipole magnet enables one to measure the magnetic rigidity (p/q) of the emitted particles, where p is the linear momentum and q the charge of the emitted particle. The octupole and sextupole magnets are used to focus the particles at the focal plane of the detector and to compensate for higher order aberrations.

The detector consists of two position sensitive wire chambers (one in the front part and one in the middle part of the detector), two ion chambers (one in the front and one in the back part), a grid and a 3-inch thick piece of plastic scintillator located at the end of the detector. A diagram of the detector box is displayed in Figure II.2 [Sh85].

Figure II.1

View of the NSCL S320 spectrograph [Be83b].

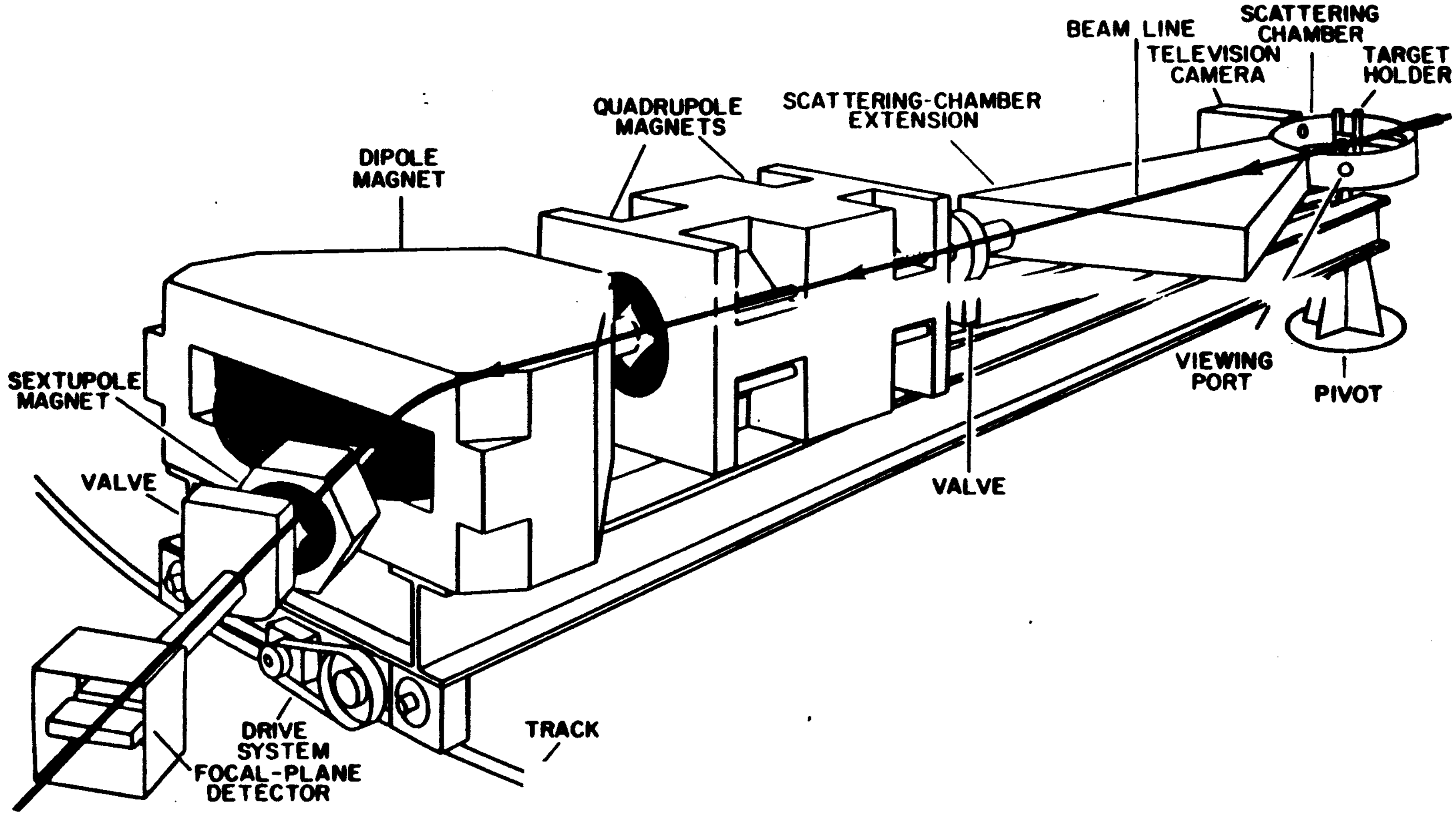
BEAM LINE
SCATTERING CHAMBER
TELEVISION CAMERA
TARGET HOLDER
QUADRUPOLE MAGNETS
SCATTERING-CHAMBER EXTENSION
DIPOLE MAGNET
SEXTUPOLE MAGNET
VALVE
VIEWING PORT
PIVOT
VALVE
DRIVE SYSTEM
FOCAL-PLANE DETECTOR
TRACK

<u>Figure II.1</u>

Figure II.2

View of the NSCL S320 detector box.

FWPC => Front wire proportional counter.

FIC => Front ion chamber.

BIC => Back ion chamber.

BWPC => Back wire proportional counter.

SC => Scintillator.

PM => Photo multiplier tube.

MSU-84-627

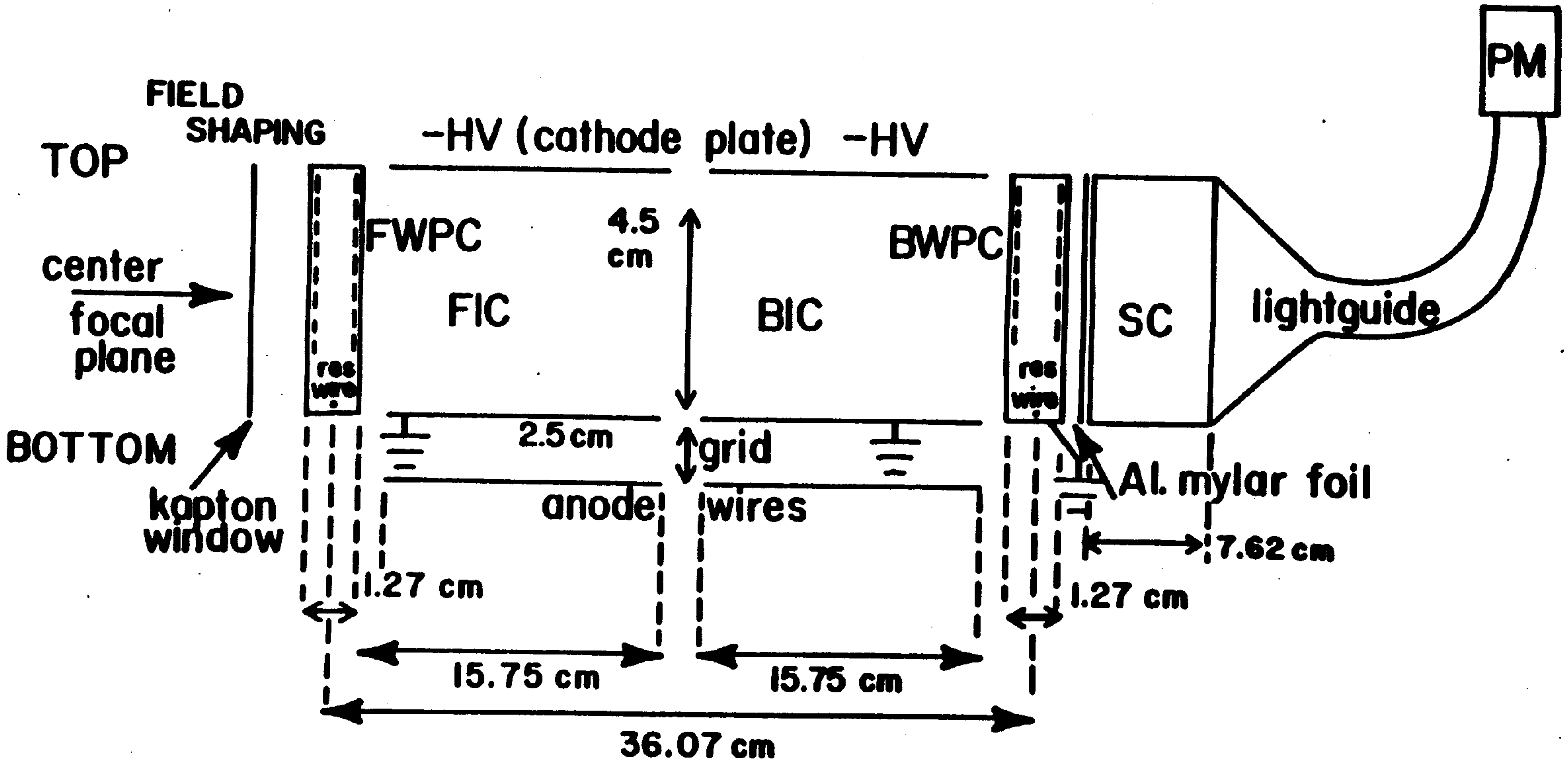

Figure II.2

Typical settings of the spectrograph magnets used for the (α,t) and (α,^{3}He) reactions of interest are given in Table II.1, in terms of both potentiometer and digital voltmeter (DVM) readings. These settings were used to focus the highest energy tritons or ^{3}He onto the focal plane of the S320, which is at the position of the front position sensitive wire chamber. The highest energy particles emitted were focused near one end of the focal plane because this enabled the examination of the excitation energy range from 0 to 15 MeV. The settings were obtained from a program called S320 [Va85a]. A more detailed description of the S320 spectrograph is given in another NSCL Thesis [Sh85].

Two collimators of different sizes, one narrow and one wide, were used during the experiment. The narrow one was used to decrease the count rate at the forward angle of 2° and the wide one was used for the other angles. The narrow collimator was made of copper, with a thickness of 0.125 inches (enough to stop 90 MeV ^{3}He) and an aperture of 1.0 by 2.0 inches. The wide collimator, which was the most frequently used one, was made of brass with a thickness of 0.25 inches (enough to stop 90 MeV tritons) and had an opening of 1.6 by 1.6 inches. Both were located 78.5 inches from the target ladder.

A number of different Faraday cups were used in the experiment. In the first two runs, two Faraday cups were

Table II.1

Typical S320 magnet settings for ^{148}Sm(α,t) and ^{148}Sm(α,^{3}He) reactions at T_α= 100 MeV and Θ_{lab}= 6°.

S320	Reaction			Reaction		
Magnet	^{148}Sm(α,t)			^{148}Sm(α,^{3}He)		
	Pot	DVM		Pot	DVM	
Q_{20} (Y)	12.48	1.221	V	5.72	0.559	V
Q_{21} (X)	3.001	-27.835	V	1.375	-12.752	V
Dipole	7.34	13.407	kG	3.25	6.142	kG
Octupl.	297.	12.638	V	136.	5.790	V
Sext.	390.	15.508	V	179.	7.105	V

used for different angles of the spectrograph. One cup was located in the target chamber and was designed to measure charge for scattering angles of 12° and larger. This Faraday cup did not have an electron suppressor, thus posing a problem with normalization. The other cup was located in the wedge and had an electron suppressor. This cup was used to measure the charge for scattering angles from 2° to 9°. In the third run, we used a single Faraday cup with an electron suppressor. This was located in the target chamber and was designed to measure the charge for scattering angles of 4° and larger. It was called the zero degree Faraday cup. It did not fulfill all of our needs, due to its inability to allow the particles of interest to travel freely to the focal plane of the spectrograph for angles of 2° and 3°. To obtain spectra at 2° and 3°, we removed the zero degree Faraday cup and normalized using the wedge Faraday cup.

All of the measurements carried out for this Thesis were normalized using the zero degree Faraday cup. Short runs of spectra at the larger angles ($\geq$ 12°) for the (α,t) reactions and at all angles for the $(\alpha,{}^3\mathrm{He})$ reactions were taken using this Faraday cup, and these were used to normalize the spectra taken before the third run. Errors in this relative normalization are included in all the cross sections quoted in this Thesis.

Because of the problem in measuring the charge during the first run, a monitor detector was used to check the normalization in the second run. The monitor detector was used before the zero degree Faraday cup was installed and so was the only means available at the time to check the normalization. It was a simple device, consisting of a single piece of plastic scintillator, as displayed in Figure II.3. It had dimensions of 0.25 by 0.25 inches by 0.75 inches thick and was made of NE102. The light pulses from the NE102 were transferred through a fiber optic cable to a photomultiplier tube. The monitor was positioned at 18° in the plane of the beam and subtended a solid angle of about 0.4 msr. We chose the angle of 18° because the angular distribution of $\sigma_{el}/\sigma_{Ruth}$ for the elastic cross section on the Sm isotopes is predicted to be flat at 18°.

Typical spectra from the monitor are displayed in Figure II.4. Note the difference between the monitor spectra when the S320 spectrograph was at 7° and at 12°. When the S320 angle was 12° or larger, the monitor spectra showed some background. At the time, as mentioned before, there were two different Faraday cups to read the charge: a wedge Faraday cup and a target chamber Faraday cup. At an angle of 12°, the latter was only about an inch away from the monitor. The background in the monitor spectrum was presumed to be due to γ-rays and neutrons emitted from the

Figure II.3

A view of the monitor detector.

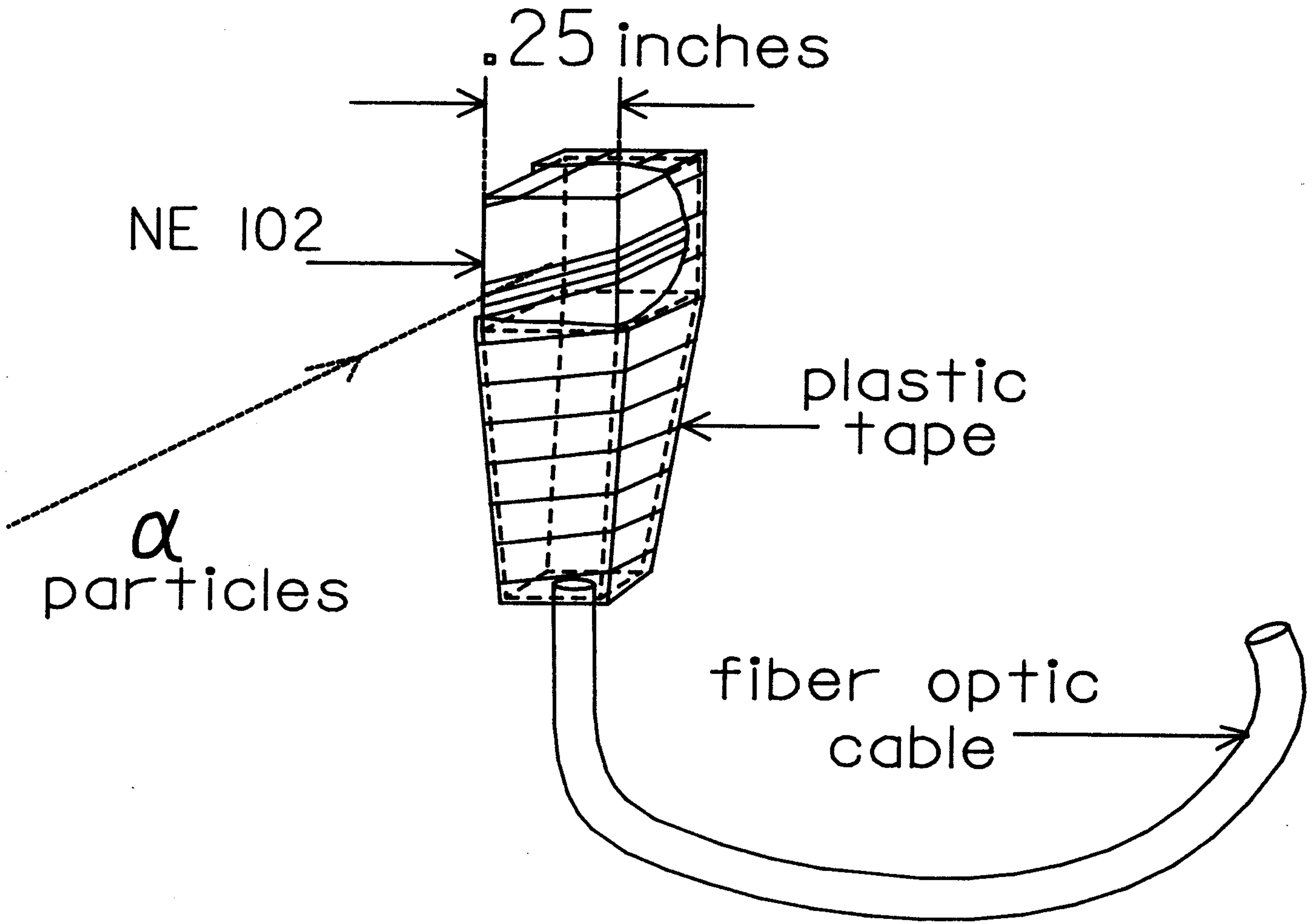

Figure II.3

Figure II.4

Typical spectra from the monitor detector. The ^{148}Sm(α,^{3}He) monitor events with the S320 scattering angles at 7° and 12° are displayed on the left. The blank frame [empty(α,^{3}He)] monitor events with the S320 scattering angles at 7° and 12° are displayed on the right.

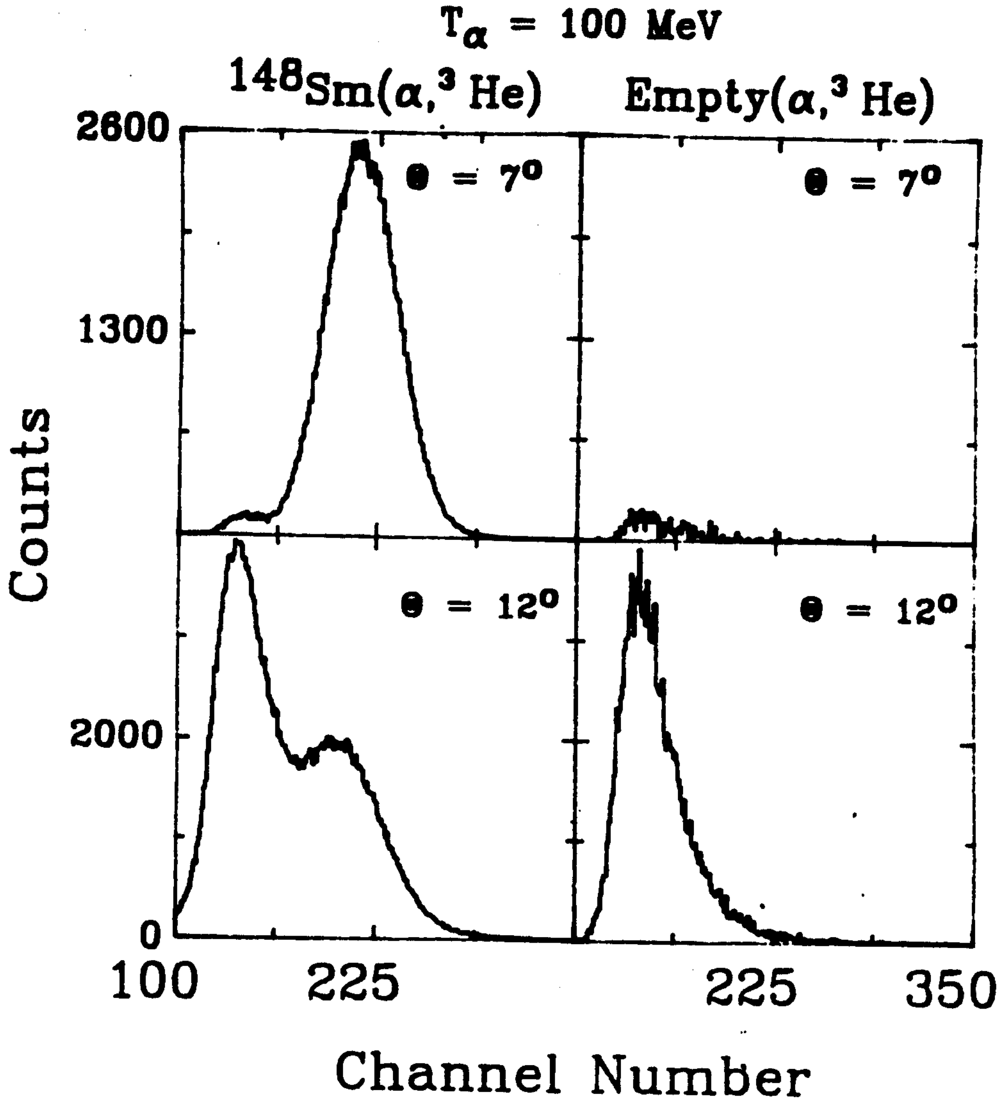
T_α = 100 MeV
^{148}Sm(α,^{3}He)
Empty(α,^{3}He)
2600
1300
2000
0
Counts
θ = 7°
θ = 7°
θ = 12°
θ = 12°
100
225
225
350
Channel Number

Figure II.4

Faraday cup. This was confirmed by putting a blank frame in place of the target and measuring the monitor spectra when the S320 spectrograph was at 7° and 12°; see the right half of Figure II.4. In view of this, we concluded that the added background was due to the Faraday cup in the target chamber.

A schematic view of the electronic setup for the S320 focal plane detector system is given in Figure II.5. The signals from the electronic modules were digitized with an ORTEC AD811 12bit analog to digital converter (ADC) and were read by a program called ROUTER [Sh85] in the LSI-11 microcomputer as part of the data acquisition system. Two different data acquisition systems were used, the first being the CAMAC system [Sh85] and the second being the 68K data acquisition system [Va85b]. The latter was used for the third run, with a series of reads and clears for each of the ADC and QDC modules used. An example of the setup program for the 68K is given in Appendix II. The example is appropriate for the measurements described in this Thesis. Both data acquisition systems needed an LSI-11 microcomputer to communicate with, and transmit data to, the Vax 11/750. Then the computer program Router [Sh85] sent the data to the tape drive unsampled and to an on-line (and off-line) data analysis program called SARA [Sh85].

Among the signals recorded for each detected particle, one was its time of flight (TOF) through the system, which

<u>Figure II.5</u>

A schematic view of the electronic set up for the S320.

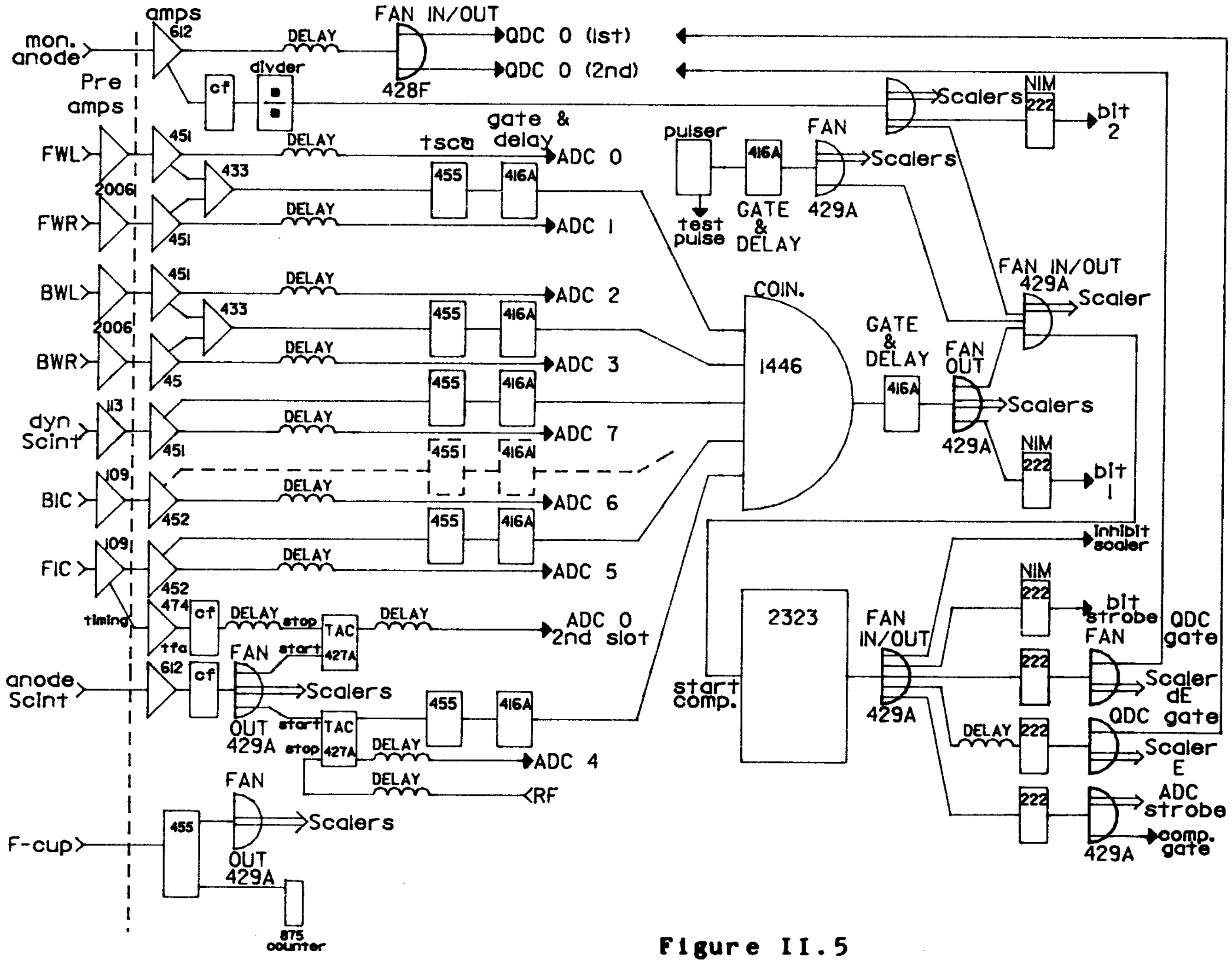
mon. anode
Pre amps
amps
612
DELAY
FAN IN/OUT
428F
QDC 0 (1st)
QDC 0 (2nd)
cf
divder
Scalers
NIM
222
bit 2
FWL
FWR
2006
451
433
DELAY
tsca
gate & delay
455
416A
ADC 0
ADC 1
pulser
test pulse
416A
GATE & DELAY
FAN
429A
Scalers
BWL
BWR
2006
451
433
45
ADC 2
ADC 3
FAN IN/OUT
429A
Scaler
COIN.
1446
GATE & DELAY
416A
FAN OUT
429A
Scalers
NIM
222
bit 1
dyn Scint
113
451
ADC 7
BIC
109
452
ADC 6
FIC
109
452
ADC 5
timing
474
tfa
cf
stop
start
TAC
427A
ADC 0 2nd slot
anode Scint
612
FAN
OUT
429A
Scalers
ADC 4
RF
inhibit scaler
2323
start comp.
FAN IN/OUT
429A
NIM
222
bit strobe
FAN
QDC gate
Scaler dE
QDC gate
Scaler E
ADC strobe
comp. gate
F-cup
455
875 counter

Figure II.5

is inversely proportional to the velocity (v) of the particle. Another signal was the energy loss of the particle due to the gas in the ion chambers; this is proportional to Z^2/mv^2, where Z is the charge and m is the mass. Hardware gates on the TOF and ion chamber signals were set such that we had a "clean" particle identification (no other types of particles in the vicinity of the group of interest). These were supplemented by software gates (called contours in 2-dimensional plots), which were set to isolate the particular outgoing particles of interest (t or ^{3}He); see Figure II.6a. SARA produced a position spectrum corresponding to these software gates (Figure II.6b). During the experiment, only a fraction of the total data was copied to the memory of the computer for display and on-line monitoring, but all of the data was copied to tape. The tapes were later played back to analyze the entire data taken during the experiment.

II.2 ENERGY CALIBRATION

Two methods were used for the energy calibration of the position spectra taken with the S320 spectrograph. One way was by identifying known levels in the final nuclei in triton and ^{3}He spectra taken with a Mylar ($(C_{10}H_8O_4)_n$) target, with all other parameters of the experiment kept the

Figure II.6

Figure II.6a

The top figures display the particle identification for the reaction $^{144}Sm(\alpha,t)$ at 2° and $^{144}Sm(\alpha,^3He)$ at 3.5°. The axes are labeled TOF (time of flight) for the y-axis and ENERGY (total energy loss in both ion chambers) for the x-axis.

Figure II.6b

The bottom figures display the typical spectrum for the reaction $^{144}Sm(\alpha,t)$ at 2° and $^{144}Sm(\alpha,^3He)$ at 3.5°.

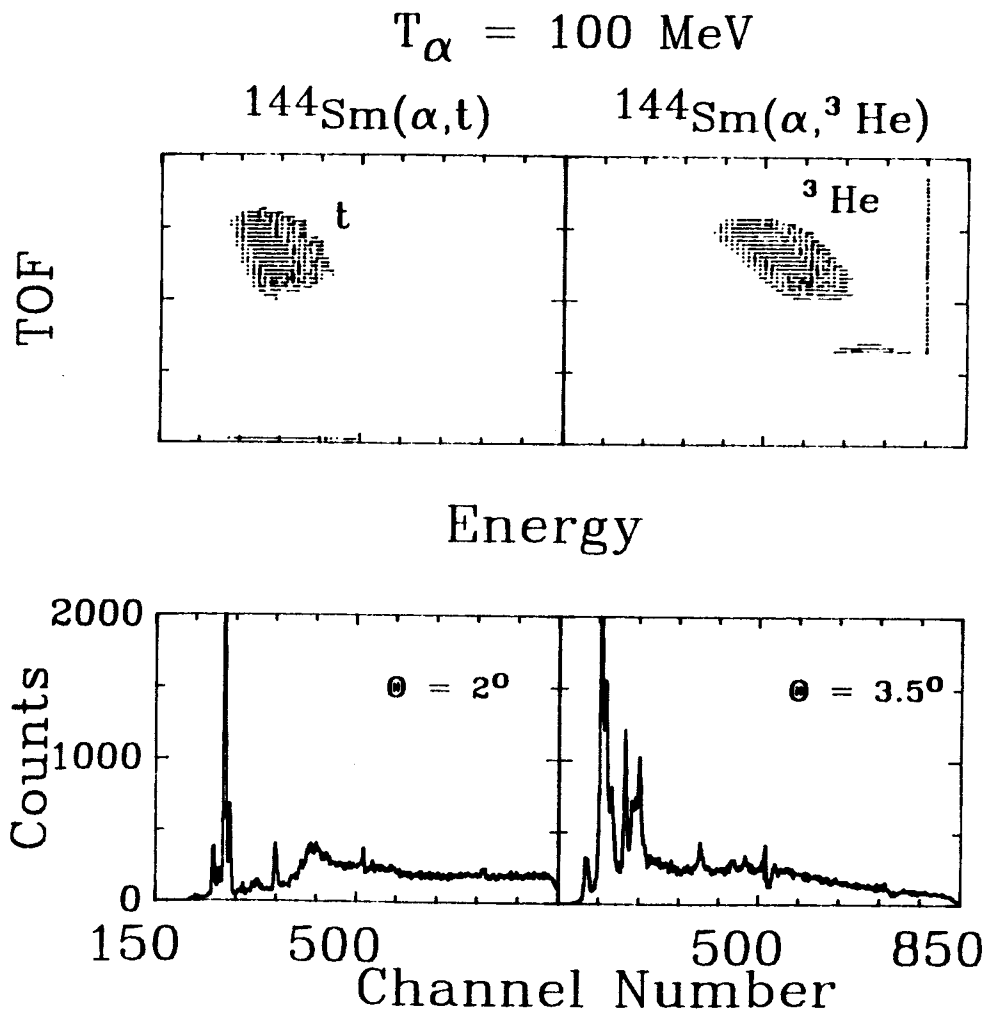

T_α = 100 MeV
^{144}Sm(α,t)
^{144}Sm(α,^{3}He)
t
^{3}He
TOF
Energy
2000
1000
0
Counts
Θ = 2°
Θ = 3.5°
150
500
500
850
Channel Number

Figure II.6

same as for a Sm target. The second way was by moving an elastic peak through the counter by changing the dipole field B.

The first method was the one used most often. Identification of peaks in the spectra was carried out using the kinematic shift in the centroids of different peaks as the scattering angle was changed. Examples of this shift are evident in the ^{13}N and ^{17}F ground state peaks shown in Figure II.7. A peak corresponding to a heavier-mass target will move a smaller distance across the focal plane as the scattering angle changes. Once we were confident about the identification of peaks in the mylar and samarium spectra with particular levels in carbon, oxygen and samarium, we then determined a best-fit calibration curve. The calibration curve is an equation expressing the kinetic energy T of the outgoing particle in terms of channel number, the relation used being a quadratic one:

$$T = a + b \times \text{channel number} + c \times (\text{channel number})^2 \quad \text{(II.1)}$$

The parameters a, b and c were calculated by a program called SPECCAL. A typical fit is shown in Figure II.8. To complete the calibration, the excitation energies in the different residual nuclei were expressed in terms of channel numbers, using the following expression.

Figure II.7

Mylar(α,t) spectra are displayed from 2° to 12°.

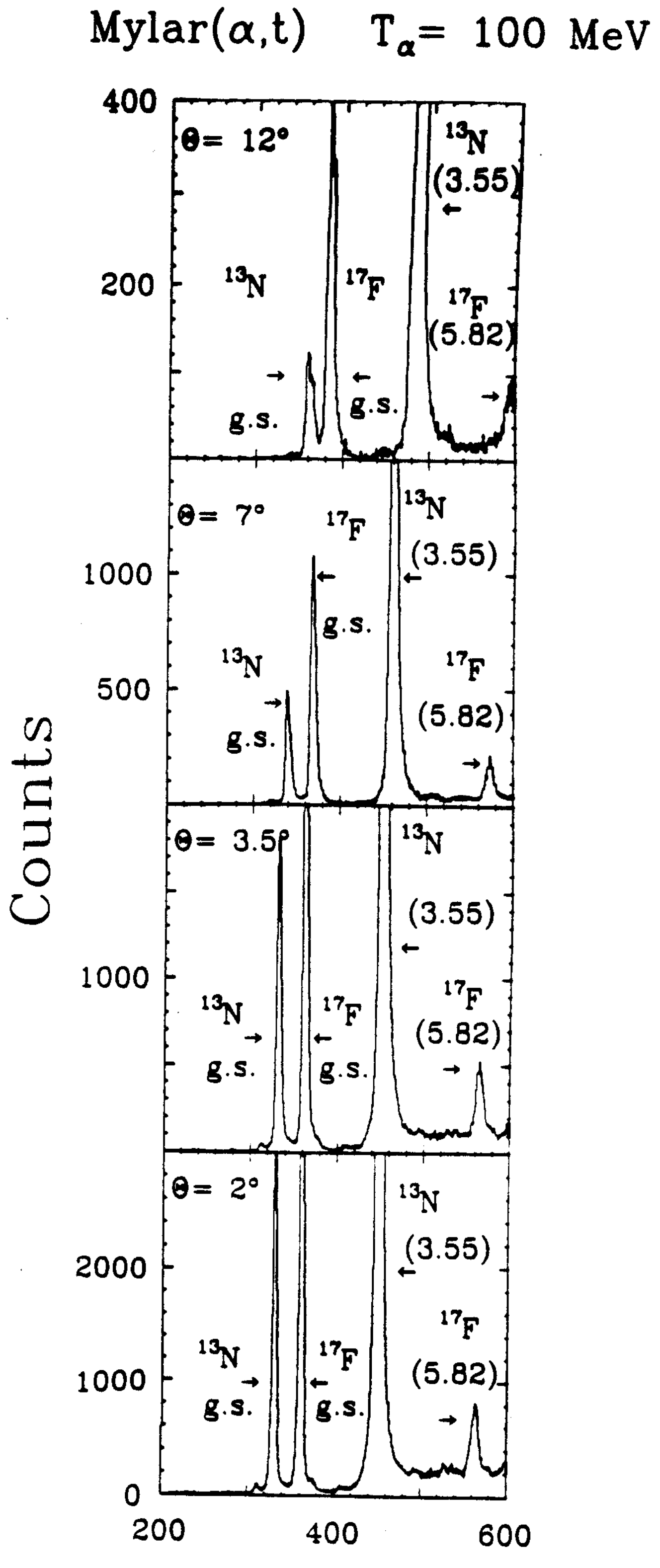
Mylar(α,t) T_α= 100 MeV
θ= 12°
^{13}N (3.55)
^{13}N g.s.
^{17}F g.s.
^{17}F (5.82)
θ= 7°
^{17}F g.s.
^{13}N (3.55)
^{13}N g.s.
^{17}F (5.82)
θ= 3.5°
^{13}N (3.55)
^{13}N g.s.
^{17}F g.s.
^{17}F (5.82)
θ= 2°
^{13}N (3.55)
^{17}F (5.82)
^{13}N g.s.
^{17}F g.s.
400
200
1000
500
1000
2000
1000
0
200
400
600
Counts
Channel Number

Figure II.7

Figure II.8

Energy calibration for the triton spectrum from the ^{144}Sm(α,t)^{145}Eu reaction. The arrows point to known states in ^{145}Eu, ^{13}N and ^{17}F. The ^{13}N and ^{17}F states were obtained by the mylar(α,t) reaction.

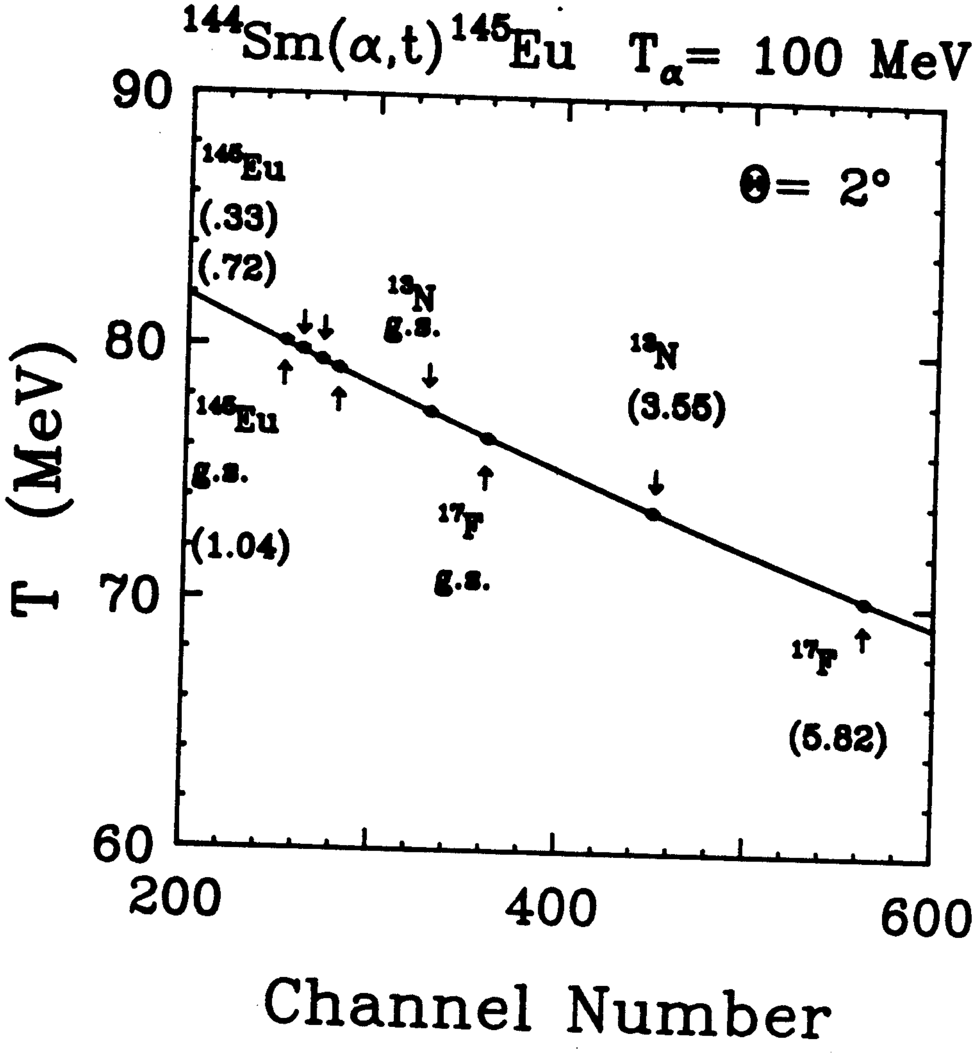

^{144}Sm(α,t)^{145}Eu T_α= 100 MeV
θ= 2°
T (MeV)
90
80
70
60
200
400
600
Channel Number
^{145}Eu
(.33)
(.72)
^{145}Eu
g.s.
(1.04)
^{13}N
g.s.
^{13}N
(3.55)
^{17}F
g.s.
^{17}F
(5.82)

Figure II.8

$$E_x = u + v \times \text{channel number} + w \times (\text{channel number})^2 \quad \text{(II.2)}$$

The terms u, v and w were also calculated by the program SPECCAL using the relation (II.1) and are related to a, b and c by a straight-forward kinematic relationship. Finally the spectrum, which to begin with was expressed in terms of counts versus channel number, was converted to a spectrum of counts versus excitation energy by the program WRITECHEX. The calibration process discussed above may be summarized in the following three steps.

1) We identified peaks of carbon and oxygen in the mylar spectra. We also identified known peaks in the samarium isotopes whenever possible.
2) The program, SPECCAL, was used to obtain the equation for excitation energy versus channel number.
3) The equation of excitation energy versus channel number was used in the program, WRITECHEX, to convert a spectrum of counts versus channel number to a spectrum of counts versus excitation energy.

A description of the SPECCAL program is given in Appendix I and a sample input file for this program is given in Appendix II.

The second method of calibrating the spectra involved moving the elastic peak across the focal plane of the S320 spectrograph as a function of the dipole field B at a fixed angle. We plotted B versus the channel number for the elastic peak. The equation,

$$p=\rho qB \tag{II.3}$$

relates the momentum p (MeV) of the emitted particle to the radius of curvature ρ (meters), the magnetic field B (kG), and the charge q (MeV/(m•kG)) of the emitted particle (units are in c=1). The equation,

$$\rho = \rho_0 + \kappa x \tag{II.4}$$

expresses the radius of curvature, ρ (meters), in terms of a constant ρ_0 and the channel number x (κ is in meters/channel number). The equation

$$p = (T(T + 2 m))^{1/2} \tag{II.5}$$

relates the kinetic energy T with the momentum p, m being the mass of the emitted particle (all units are in MeV since c=1). From equations (II.3), (II.4) and (II.5), we deduced a relation between the kinetic energy T and the channel number x. We then proceeded, as we did in the mylar case, to acquire a spectrum of counts versus excitation energy.

The two methods gave excitation energies which agreed with each other to within 50-100 keV, depending upon the position in the detector. The closest agreement (50 keV) was at the center of the detector.

Triton and ^{3}He spectra from the (α,t) and (α,^{3}He) reactions on the Sm isotopes are shown in Chapter V.

CHAPTER III

DWBA CALCULATIONS

In this section, we will discuss the Distorted Wave Born Approximation (DWBA) calculations used to analyze the stripping reactions (α,t) and (α,^{3}He) employed in this work. In both reactions, a nucleon is removed from the projectile: a proton in the (α,t) case and a neutron in the (α,^{3}He) case. We therefore discuss first the DWBA formalism of single-nucleon transfer reactions, including a definition of the spectroscopic factor already introduced in Chapter I. Then we discuss the application of this formalism, using the DWBA program DWUCK4 [Ku69], to the specific cases of interest to us. Reasons for our particular choice of optical parameters will be given, followed by details of the calculation of the DWBA angular distributions for different excitation energies and different ℓ-transfers.

III.1 DWBA FORMALISM

Let us consider the reaction A(α,β)B, where A is the target nucleus, α the projectile, β the emitted particle and B the residual nucleus. If particle α consists of β+x then the reaction (α,β) is a stripping reaction which strips the particle x. For our cases, x is a proton (p) when β is a triton (t) and x is a neutron (n) when β is a ^{3}He particle. If β consists of α+x, then the reaction (α,β) is a pickup reaction in which the projectile picks up a particle x from the target. We will concentrate on stripping reactions here. This direct reaction process allows one to investigate the excitation energy levels of the residual nucleus B and determine the extent to which they are single-particle states built on the ground state of the target A.

The DWBA involves three basic physical assumptions listed below [Ma69]:

1) Nucleon transfer occurs directly between two active channels (A,α) and (B,β),
2) Optical-model wave functions for $A+\alpha$ and $B+\beta$ are correct in all relevant regions of the configuration space,
3) The transfer process is weak enough to permit a first-order treatment.

To find an expression for the angular distributions of such direct reactions one must first consider the transition amplitude, which may be expressed as

$$T = J \int d^3r_{\beta B} \int d^3r_{\alpha A} \; \phi^-_{\beta B}(\vec{k}_{\beta B},\vec{r}_{\beta B}) \langle \beta B | W | \alpha A \rangle \phi^+_{\alpha A}(\vec{k}_{\alpha A},\vec{r}_{\alpha A}) \tag{III.1}$$

Here J signifies the Jacobian that transforms the center of momentum system to the lab system. $\langle \beta B|W|\alpha A\rangle$ is the matrix element for the transition from the state $|\alpha A\rangle$ to the state $|\beta B\rangle$ through the potential W.

$\phi^{\pm}(\vec{k},\vec{r})$ are the $\binom{\text{incoming}}{\text{outgoing}}$ distorted waves (plane wave plus spherical scattered wave) describing the motion of α in the entrance channel and of β in the exit channel. The ϕ are assumed to depend only on the separation of the centers of mass of the colliding pairs and to be independent of the spins. In DWBA, they are taken to be the distorted waves which describe the observed elastic scattering. They are solutions to

$$(\nabla^2 + k^2 - \frac{2\mu}{\hbar^2} V(r))\ \phi(\vec{k},\vec{r}) = 0 \qquad \text{(III.2)}$$

where V(r) is the optical potential.

Let L_α and L_β denote the orbital angular momenta in the incoming and outgoing channels of the reaction A(α,β)B and let ℓ denote the transferred angular momentum. These angular momenta must satisfy the conservation laws for angular momentum and parity

$$\vec{L}_\alpha + \vec{\ell} = \vec{L}_\beta . \qquad \text{(III.3a)}$$

$$(-1)^{L_\alpha + \ell} = (-1)^{L_\beta} \qquad \text{(III.3b)}$$

The elastic scattering in the channels (A,α), (B,β) is dominated by a few partial waves

$$\begin{aligned} L_\alpha &\approx k_\alpha R \\ L_\beta &\approx k_\beta R \end{aligned} \qquad \text{(III.4)}$$

close to those whose classical impact parameters correspond to a grazing collision with the surface of the nucleus. Higher partial waves give no contribution to the cross section because the centrifugal barrier excludes them from the region of the interaction, while lower partial waves are completely absorbed and do not reappear in the elastic channel.

If conditions in case of the transfer reaction are such that the conservation laws (III.3) are satisfied for angular momenta close to those favored in elastic scattering, that is, if

$$|k_\alpha R - k_\beta R| \approx \ell \qquad \text{(III.5)}$$

then the transfer cross sections are dominated by partial waves that are well determined by the elastic scattering. Under such circumstances, most of the contribution to the transfer cross section comes from the nuclear surface region and DWBA works well.

The wave functions $\phi^{+}_{\alpha A}(\vec{k}_{\alpha A},\vec{r}_{\alpha A})$ and $\phi^{-}_{\beta B}(\vec{k}_{\beta B},\vec{r}_{\beta B})$ can be written as the partial wave expansion,

$$\phi^{+}_{\alpha A}(\vec{k}_{\alpha A},\vec{r}_{\alpha A}) = \frac{4\pi}{k_{\alpha A} r_{\alpha A}} \sum_{L_\alpha M_\alpha} Y^{M_\alpha}_{L_\alpha}(\hat{r}_{\alpha A})\, Y^{M_\alpha}_{L_\alpha}(\hat{k}_{\alpha A})^{*}\, i^{L_\alpha} \times \chi^{(\alpha)}_{L_\alpha}(k_{\alpha A} r_{\alpha A}) \tag{III.6}$$

$$\phi^{-}_{\beta B}(\vec{k}_{\beta B},\vec{r}_{\beta B}) = \frac{4\pi}{k_{\beta B} r_{\beta B}} \sum_{L_\beta M_\beta} Y^{M_\beta}_{L_\beta}(\hat{r}_{\beta B})\, Y^{M_\beta}_{L_\beta}(\hat{k}_{\beta B})^{*}\, i^{L_\beta} \times \chi^{(\beta)}_{L_\beta}(k_{\beta B} r_{\beta B})$$

where $\hat{k}$ and $\hat{r}$ are the unit vectors in polar coordinates.

From equations (III.2) and (III.6) we find that the $\chi^{(\gamma)}_{L_\gamma}(kr)$ are solutions of the radial equation with the central potential V(r),

$$\left[\frac{d^2}{dr^2} + k^2 - \frac{L_\gamma(L_\gamma+1)}{r^2} - \frac{2\mu}{\hbar^2} V(r)\right] \chi^{(\gamma)}_{L_\gamma}(kr) = 0 \tag{III.7}$$

V(r), the optical model potential mentioned above, is of the form

$$V(r)=V_C(r) + V_N(r) + V_{\ell\cdot s}(r) \tag{III.8}$$

where $V_C(r)$ is the Coulomb potential and $V_N(r)$ and $V_{\ell \cdot s}(r)$ are the central and spin-orbit parts, respectively, of the nuclear potential.

We turn now to the crux of the matter - form factors and spectroscopic factors. These are contained in (III.1) in the matrix element $\langle B,\beta|W|A,\alpha\rangle$ integrated over the internal co-ordinates of the core nucleus A and of the lighter projectile β. If the effective transition operator W is taken to be the interaction $V_{\beta x}$ between projectile β and the transferred nucleon, the effective matrix element separates into a product of two disjoint form factors

$$\langle B,\beta|V_{\beta x}|A,\alpha\rangle_A = \langle B|A\rangle_A \langle \beta|V_{\beta x}|\alpha\rangle_\beta, \qquad \text{(III.9)}$$

with the nuclear form factor $\langle B|A\rangle_A$ independent of $V_{\beta x}$.

The projectile form factor $\langle \beta|V_{\beta x}|\alpha\rangle_\beta$ is evaluated using suitable internal wavefunctions for α and β and with suitable assumptions about the range of $V_{\beta x}|\alpha\rangle$ as a function of $\vec{r}_x - \vec{r}_\beta$. We shall use the zero-range approximation

$$f(r_{\beta x}) = \delta(r_{\beta x}) \qquad \text{(III.10)}$$

for the projectile form factor, since past work by Gales et al [Ga85a] has shown that the DWBA angular distributions calculated within the zero-range approximation and the finite-range approximation have the same shape.

We have now isolated the single-nucleon form factor

$$\Phi_{BA}(x) = \langle B|A\rangle_A = \langle B|a^\dagger(x)|A\rangle \qquad \text{(III.11)}$$

It is an overlap integral (integrated only over the internal coordinates of the core nucleus A) or, equivalently, a matrix element of the operator $a^\dagger(\vec{x})$ that creates a nucleon with co-ordinates $\vec{x}$. Its angular momentum decomposition is

$$\Phi_{BA}(\vec{x}) = \sum_j F^{\ell j}_{BA}(x)\, Y^{\ell j}_m(\hat{x})\, \langle J_A M_A j m | J_B M_B\rangle \qquad \text{(III.12)}$$

where Y is a spin-angle function and $\langle J_A M_A j m | J_B M_B\rangle$ is a Clebsh-Gordon coefficient. The radial form factors F are unnormalized; the normalization constants necessary to introduce normalized form factors f

$$F^{\ell j}_{BA}(x) = \left(S^{\ell j}_{BA}\right)^{1/2} f^{\ell j}_{BA}(x) \qquad \text{(III.13)}$$

are the spectroscopic amplitudes $\left(S^{\ell j}_{BA}\right)^{1/2}$. $S^{\ell j}_{BA}$ is the spectroscopic factor.

The differential cross section for the reaction $A(\alpha,\beta)B$ may be expressed in terms of the transition amplitude T as

$$\frac{d\sigma}{d\Omega} = \frac{\mu_\alpha \mu_\beta}{(2\pi\hbar^2)^2} \frac{k_\beta}{k_\alpha} \frac{1}{2J_A + 1} \frac{1}{2s_\alpha + 1} \sum_{M_A M_B m_\alpha m_\beta} |T|^2 = \sum_{\ell s j} \frac{d\sigma}{d\Omega}^{\ell s j}$$

(III.14)

where

$$\frac{d\sigma}{d\Omega}^{\ell sj} = \frac{2J_B+1}{(2J_A+1)(2j+1)} \, N \, C^2 S_{\ell j} \, \frac{d\sigma}{d\Omega}^{\ell sj}_{DWBA} \qquad \text{(III.15)}$$

$\frac{d\sigma}{d\Omega}^{\ell sj}_{DWBA}$ is the reduced differential cross section which the program DWUCK4 [Ku84] calculates using (III.1) through (III.9). C is a Clebsh-Gordon coefficient which describes the isospin coupling between the target, transferred nucleon and residual nucleus:

$$C \equiv \langle T_A T_{z_A} \, t \, t_z | T_B T_{z_B} \rangle$$

The literature is marred by a good deal of confusion between the use of S and C^2S. In the case of neutron stripping reactions C^2 has the value of unity, but not in general for proton stripping reactions. As equation (III.15) shows, C^2S is the quantity directly entering in the cross section. In this Thesis, we shall present results for C^2S, which we call the spectroscopic strength. Since the Sm targets used in this study are all even-even nuclei, they have $J_A=0$; so j must equal J_B and the spin statistical weight factor $(2J_B+1)/(2J_A+1)(2j+1)$ in equation (III.15) is unity. Thus knowledge of the j value is not needed for obtaining C^2S.

N is a normalization factor which incorporates the effect of the zero-range approximation for the light-ion vertex. Its value depends on the specific light ions, α and β, involved in the reaction, but is independent of the target A. A value of N=36 had been calculated previously [Fr77,Ga85a] for the (α,t) and $(\alpha,{}^3He)$ reactions, with an error of 15% due mainly to the uncertainty in the optical model potentials [Fr77]. This value of N will be used to determine C^2S values for low-lying states populated by the (α,t) and $(\alpha,{}^3He)$ reactions on ${}^{208}Pb$; we shall compare them with C^2S values from previous work. The same value of N will be used for both the (α,t) and $(\alpha,{}^3He)$ reactions. This is because the bonding potentials for the two reactions are very similar: the mass difference for (α,t) is $m_\alpha-(m_t+m_p)$ = -19.81 MeV and that for $(\alpha,{}^3He)$ is $m_\alpha-(m_{{}^3He}+m_p)$ = -20.58 MeV.

Equation (III.15) provides us with the means to extract from experiment the spectroscopic strengths $C^2S_{\ell j}$, by comparing the experimental cross section $\frac{d\sigma}{d\Omega}^{\ell sj}$ with $\frac{d\sigma}{d\Omega}^{\ell sj}_{DWBA}$, which is the calculated DWBA cross sections for a state ℓsj which has the full single-particle strength. In Chapter IV we shall describe in more detail this method of extracting the experimental spectroscopic strengths. The sum of the spectroscopic strengths of all fragments in the residual nucleus for a given single-particle (or single-hole) excitation $n\ell j$ measures the extent to which orbit $n\ell j$ is empty (or occupied) in the target ground state $|A\rangle$. In the case of neutron (proton) stripping reactions, the sum of spectroscopic strengths for a particular orbit $(n\ell j)$ over the entire excitation energy region is equal to unity or less depending upon whether the ground state of the target nucleus is empty or partially occupied with neutrons (protons) in that orbit. This is clear from (III.13) and it is expressed by the inequality

$$\sum_{\varepsilon} C^2 S_{\ell j}(\varepsilon) \leq 1 \qquad \text{(III.16)}$$

The limited range of excitation energies which can be studied experimentally may also contribute to this inequality. Chapter VI will be devoted to the predictions of the spectroscopic strength using two models and their comparison with the experimental spectroscopic strengths extracted from this experiment.

III.2 APPLICATION TO (α,t) AND $(\alpha,{}^3He)$ REACTIONS ON SM ISOTOPES

The program DWUCK4 requires an input of optical model parameters to calculate the angular distributions. Parameters obtained from elastic scattering experiments as described in the literature were used. The entrance channel $(\alpha+A)$ and the exit channel $(\beta+B)$ each has its own optical model set. The former was obtained from the elastic scattering of 81.4 MeV α-particles on Pb [Pe81,Ga85a]. The exit channel parameters were those determined from the elastic scattering of ^{3}He beams of 130 MeV on Pb [Dj77,Pe81]. There are no data for elastic scattering of triton beams at high energies and so the triton exit channel parameters were chosen to be the same as the ^{3}He parameters. The justification for this is that both t and ^{3}He are mass-3 particles and also there is very little difference between the energies for stripping a proton or a neutron from an α-particle (see above). The difference in the Coulomb potentials for the two particles was of course taken into account.

There are three parts to the optical potential, as given in equation (III.8). The Coulomb part is expressed as

$$V_C(r) = \begin{cases} (Z_p\ Z_T\ e^2)/(2R_C)(3 - r^2/R_C^2), & r \leq R_C \\ Z_p\ Z_T\ e^2 / r, & r > R_C \end{cases} \qquad \text{(III.17a)}$$

with $R_C = r_C\ A^{1/3}$. The central nuclear potential is expressed as a Woods-Saxon shape with a volume absorption part:

$$V_N(r) = \frac{V_0}{1 + \exp(\frac{r - R}{a})} + \frac{iW_0}{1 + \exp(\frac{r - R}{a}i)} \qquad \text{(III.17b)}$$

The spin-orbit part of the potential is expressed as

$$V_{\ell \cdot s}(r) = V_{so} \frac{\ell \cdot s}{r} \frac{d}{dr} \frac{1}{1 + \exp\left(\frac{r - R_{so}}{a_{so}} \right)} \qquad \text{(III.17c)}$$

where $R_i = r_o^i A^{1/3}$ and $R_{so} = r_{so} A^{1/3}$.

Different sets of optical model parameters were tested by comparing the corresponding DWBA angular distributions with experimental angular distributions for low-lying states (with known ℓ-transfers) from the ^{144}Sm(α,t) reaction measured in our experiment. The set given in Table III.1 [Ga85a] is the one that best reproduces the measured angular distributions. Figures showing the quality of the fits of the DWBA calculations to the experimental angular distributions are given in Chapter V.

Bound-state wave functions are also needed in the DWBA calculation, to describe the binding of the transferred nucleon x to the core nucleus A. They were calculated in a bound-state potential for which a Woods-Saxon shape was used. The radius and diffuseness parameters of this potential are given in Table III.1 and the depth was adjusted to fit the empirical binding energy of the transferred nucleon [Pe81].

Using these optical-model and bound-state parameters, DWBA angular distributions were calculated for various

Table III.1

Optical model potential parameters used for the (α,t) and (α,^{3}He) reactions on samarium and lead targets for a 100 MeV α-particle incident energy.

Channel	V_0 (MeV)	r_0 (fm)	a (fm)	W_0 (MeV)	r' (fm)	a' (fm)	V_{so} (MeV)	r_{so} (fm)	a_{so} (fm)	r_c (fm)
α	158.4	1.32	0.62	30.02	1.35	0.85	-	-	-	1.4
t	125.4	1.18	0.86	17.20	1.55	0.77	-	-	-	1.4
^{3}He	125.4	1.18	0.86	17.20	1.55	0.77	-	-	-	1.4
				Bound state parameters						
p	V_n	1.25	0.65				λ=25	1.25	0.65	

In the case of proton particle states in ^{209}Bi a different geometry was used, with r_o= 1.28 fm, a_o= 0.76 fm, r_{so}= 1.09 fm and a_{so}= 0.60 fm.

excitation energies from 0 to 20 MeV. For a given ℓ-transfer, they change in shape and magnitude as a function of excitation energy. This is evident from Figure III.1, in which the $\ell=3$ angular distributions at excitation energies of 2.0 MeV and 10.0 MeV for the case of ^{144}Sm(α,t) are compared. The angular distributions changed in magnitude by about 4% when the excitation energy changed from 2 MeV to 3 MeV. In order to keep the the error in the DWBA calculations less than 4%, an interpolation scheme was set up as follows. The DWBA angular distributions were calculated in one MeV steps from 0 MeV to 20 MeV and the angular distribution at any intermediate excitation energy was obtained by linearly interpolating between adjacent integer excitation energies.

Additionally, the DWBA calculations showed that, for a fixed spectroscopic strength, there were large variations in the cross sections for different ℓ-transfers at the same excitation energy. This can be seen in Figure III.2. Generally we observed that with increasing ℓ, the cross section also increased. This favoring of high-ℓ transfer is a result of the fact that the angular momentum matching condition (III.5) picks out high ℓ values for single-nucleon transfer reactions induced by 100-MeV α particles. For the same C^2S, the ℓ = 6 or 7 cross sections are two orders of magnitude larger than the $\ell=0$ or 1 cross sections. This has the consequence that the reactions studied are not sensitive

Figure III.1

Calculated angular distributions for the case of $\ell=3$ transition in the ^{144}Sm(α,t)^{145}Eu reaction at excitation energies of 2.0 and 10.0 MeV, for a beam energy of 100 MeV. The calculations were done using the code DWUCK4 [Ku84].

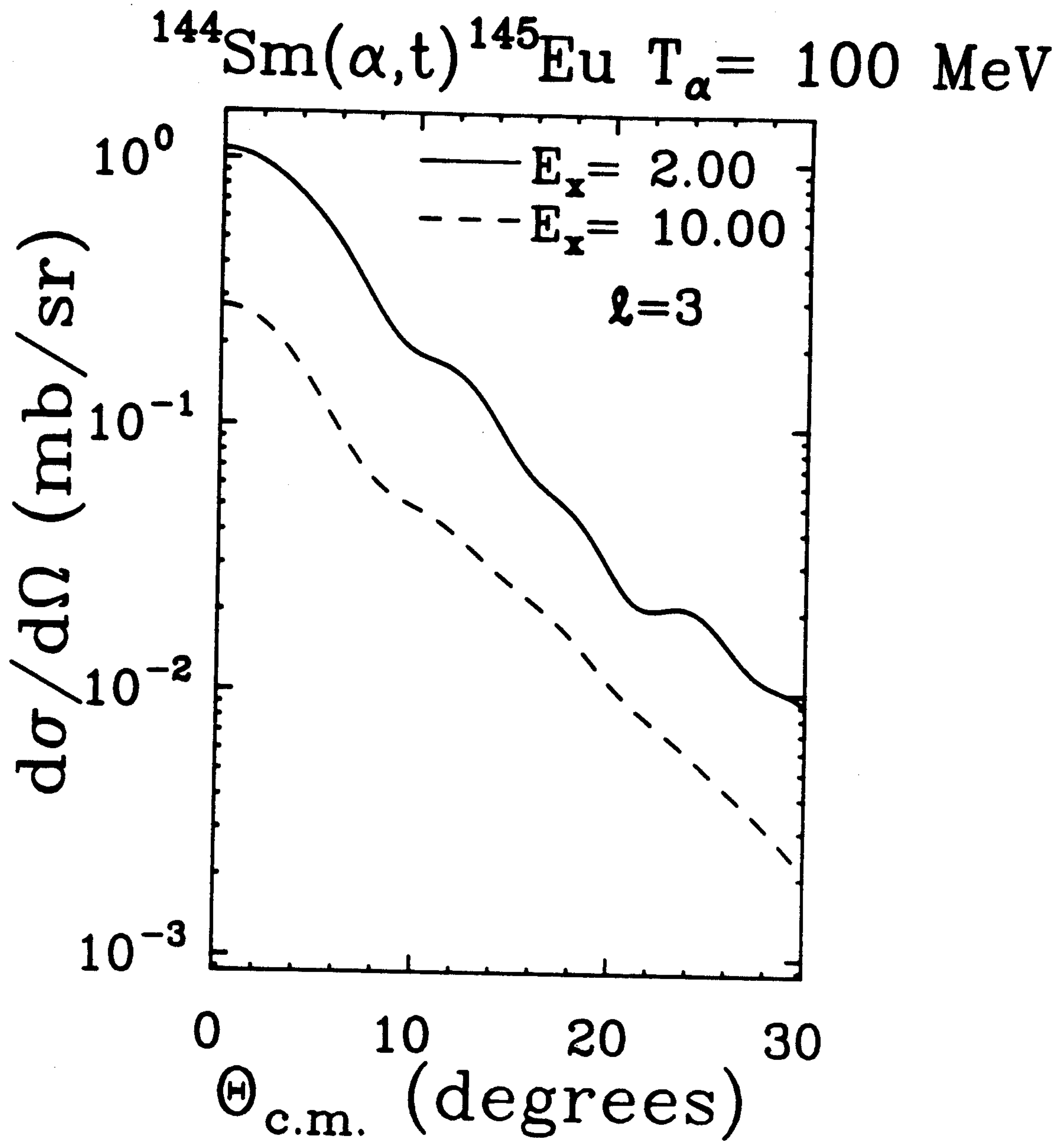
^{144}Sm(α,t)^{145}Eu T_α= 100 MeV
E_x= 2.00
E_x= 10.00
ℓ=3
10^0
10^{-1}
10^{-2}
10^{-3}
$d\sigma/d\Omega$ (mb/sr)
0
10
20
30
$\Theta_{c.m.}$ (degrees)

Figure III.1

Figure III.2

Calculated angular distributions for ℓ-transfers of 0, 1, 2, 3, 4, 5, 6 and 7 in the ^{144}Sm(α,t)^{145}Eu reaction at an excitation energy of 8.0 MeV, for a beam energy of 100 MeV. The full single-particle strength ($C^2S=1$) was used for each ℓ-transfer. The calculations were done using the code DWUCK4 [Ku84].

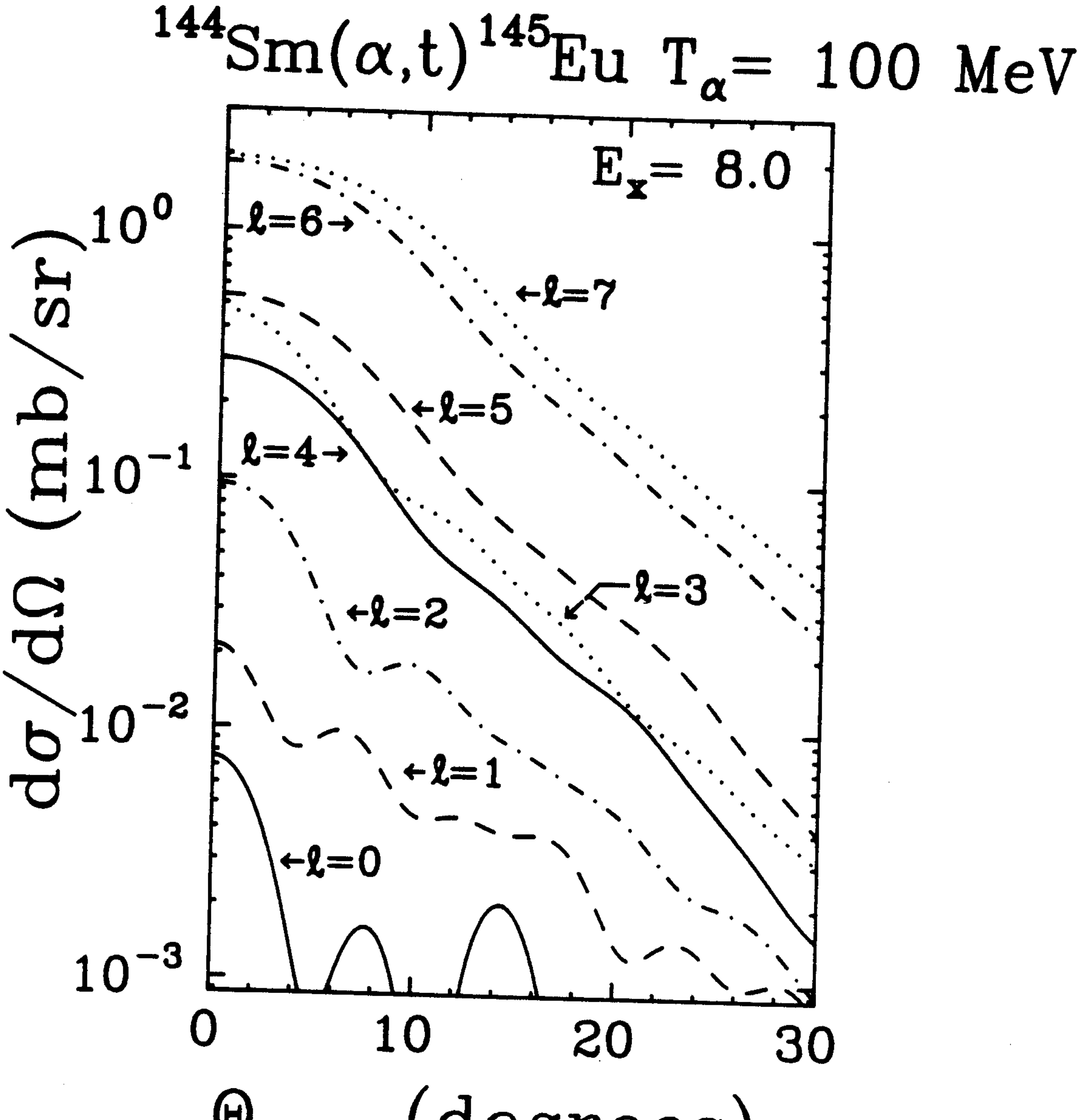
$^{144}Sm(\alpha,t)^{145}Eu$ T_α= 100 MeV
E_x= 8.0
ℓ=6→
←ℓ=7
←ℓ=5
ℓ=4→
←ℓ=3
←ℓ=2
←ℓ=1
←ℓ=0
10^0
10^{-1}
10^{-2}
10^{-3}
$d\sigma/d\Omega$ (mb/sr)
0
10
20
30
$\Theta_{c.m.}$ (degrees)

Figure III.2

to low ℓ in the presence of high ℓ, even though the two may be present with comparable spectroscopic strengths. It must also be noted that the shapes of the angular distributions are distinctive for low ℓ-values (ℓ=0, 1 and 2) but become rather similar for ℓ≥3. Thus identification of ℓ values (for ℓ≥3) on the basis of angular distribution shapes alone was very difficult.

The DWBA code was used to calculate angular distributions for both bound and unbound states. An unbound state is one whose excitation energy is greater than the separation energy of the transferred nucleon. The separation energy is the amount of energy necessary to separate a particle from a nucleus. For instance, the separation energy for a proton in the ^{145}Eu nucleus is 3.25 MeV. So states in ^{145}Eu at excitation energies greater than 3.25 MeV populated in the ^{144}Sm(α,t)^{145}Eu reaction are unbound to proton emission.

To calculate angular distributions for unbound states, the DWBA program used the Vincent-Fortune method [Vi70]. The form factor distribution was used to monitor the convergence of the calculated solution for all the ℓ-transfers considered and for all excitation energies above the separation energy. If the form factor does not converge at some excitation energy, then the angular distribution cannot be calculated by DWUCK4 for the given ℓ-transfer. All excitation energies above this one will also not be calculable for the given $n\ell j$ (one must increase the number of nodes n to regain the convergence, like $(n+1)\ell j$).

The lack of convergence is associated with the onset of the inability of the centrifugal-plus-Coulomb barrier to hold the nucleon inside the nucleus. Since the barrier increases with increasing ℓ and is higher for protons than for neutrons, the cutoff excitation energy is higher for high ℓ's than for low ℓ's and, for a given ℓ, is higher for protons than for neutrons. Thus, for instance, for the case of proton states in Eu, the ℓ-transfer of 3 ($2f_{7/2}$) cannot be calculated by DWUCK4 above an excitation energy of 12 MeV; the corresponding form factor distribution does not converge and has a large magnitude for oscillations at distances of 15 to 25 fm from the nucleus. But higher ℓ-transfers can be calculated. Similarly, for neutron states in the samarium isotopes, ℓ-transfers of 3 ($2f_{7/2}$) and 4 ($2g_{9/2}$) cannot be calculated above the excitation energy of 7 MeV, whereas the cutoff for an ℓ-transfer of 6 ($1i_{13/2}$) is 12 MeV.

Chapter IV

DATA REDUCTION AND ANALYSIS

In many previous studies of single-nucleon transfer reactions, the extraction of information from experimental spectra seemed to be somewhat arbitrary and subjective. For example, one would hand draw a background and use gaussians to fit gross structures. Angular distributions obtained from the gaussian fits depended on the background drawn. The widths of the gaussians used to fit the gross structures were rather arbitrary. One rather extreme example of these procedures is illustrated in Figure IV.1 [Ga81].

In the present work, in an attempt to be more systematic in the analysis than was generally the case in the past, the background was estimated by a calculation instead of by hand drawing it. Also, a slicing technique was used instead of gaussians to calculate angular distributions. Both these techniques have been used in recent work on particle states [Ga82b,Ga83,Ga85a,b].

The goal of our analysis was to determine the single-particle strength as a function of excitation energy using the angular distributions obtained from the systematic

Figure IV.1

Energy spectra of residual nuclei ^{143,147,151}Sm from the ^{144,148,152}Sm(^{3}He,α)^{143,147,151}Sm reactions at a beam energy of 70 MeV, taken from Gales et al. [Ga81]. The dashed lines that appear under the spectra are hand drawn backgrounds. Also shown are the gross structure gaussians A and B which were used to fit the spectra.

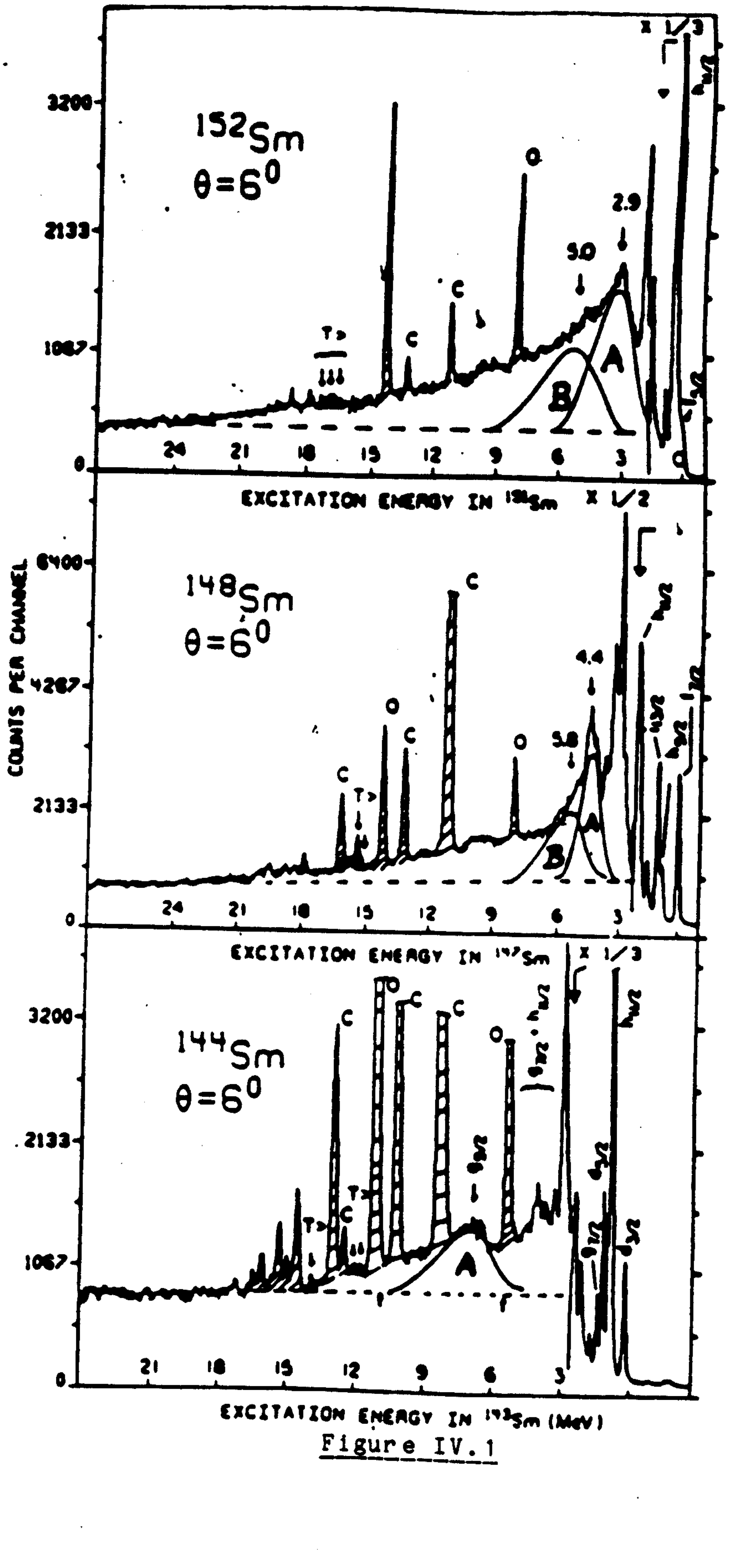
^{152}Sm
$\theta=6^0$
^{148}Sm
$\theta=6^0$
^{144}Sm
$\theta=6^0$
COUNTS PER CHANNEL
3200
2133
1067
0
6400
4267
2133
0
3200
2133
1067
0
24
21
18
15
12
9
6
3
21
18
15
12
9
6
3
X 1/3
X 1/2
X 1/3
2.9
3.0
4.4
5.8
A
B
A
B
A
C
O
T>
$h_{11/2}$
$g_{9/2}$
$d_{5/2}$
EXCITATION ENERGY IN ^{151}Sm
EXCITATION ENERGY IN ^{147}Sm
EXCITATION ENERGY IN ^{143}Sm (MeV)

Figure IV.1

procedure mentioned above.

IV.1 BACKGROUND

Cross sections obtained from a measured spectrum clearly depend on the background which is subtracted from the spectrum. In order to try to be less arbitrary than in earlier analyses, an attempt was made to treat the background systematically and calculate it with few arbitrary assumptions. The model used for the calculation was the plane wave breakup model (PWBM) applied to the case of α-particle breakup [Wu79]. Work carried out by Wu et al. [Wu 79] has shown that, when fast α particles (80 and 160 MeV) are scattered from medium-heavy nuclei, the breakup process yields a significant contribution to the reaction cross section.

The α-breakup model is analogous to the deuteron [Se47] and ^{3}He [Me85] breakup models. In the deuteron breakup model, the proton and neutron are scattered and in the ^{3}He breakup model, the deuteron and proton are scattered. In the α-breakup model, the projectile (an α particle) peripherally collides with the target nucleus and then divides into two constituents. The constituents are a triton and a proton or a ^{3}He and a neutron. The (α,tp) or (α,^{3}He n) reaction can leave the target nucleus either in its ground state or in an excited state. These two processes are called elastic and inelastic breakup, respectively.

Schematic illustrations of these processes are given in Figure IV.2 [Me85].

The S320 spectrograph was set up to detect either the tritons or ^{3}He's in the singles mode. A coincidence experiment to study the breakup processes, although interesting, would have been very difficult and time consuming, in view of the small solid angle of the S320 spectrograph ($\leq$ 0.6 msr).

Recent ^{3}He breakup work has been carried out by Aarts et al. and Meijer et al. [Aa82,Aa84,Me85], using a 52-MeV beam of ^{3}He bombarding ^{28}Si. Coincidence experiments were used to study the breakup of ^{3}He by the ^{28}Si(^{3}He,dp) reaction and various models were developed to explain the data. These experiments show that the elastic breakup process is more dominant than the inelastic process [Me85].

α breakup coincidence experiments do not exist at the present time. Our procedure then was to use the ^{3}He breakup model as a guide to develop a parallel α-break up model. In view of the ^{3}He results, we considered only the elastic breakup in our model. The elastic breakup cross section is given by the expression [Wu79,Me85]

$$\partial^2\sigma/\partial\Omega\partial E = c\ \sigma(xA)\ \langle\phi(q)\rangle^2\ \rho \qquad \text{(IV.1)}$$

Here, c is a constant. $\sigma(xA)$ is the total reaction cross

Figure IV.2

A schematic representation of two projectile breakup processes, sketch (1) being the elastic breakup and (2) the inelastic breakup.

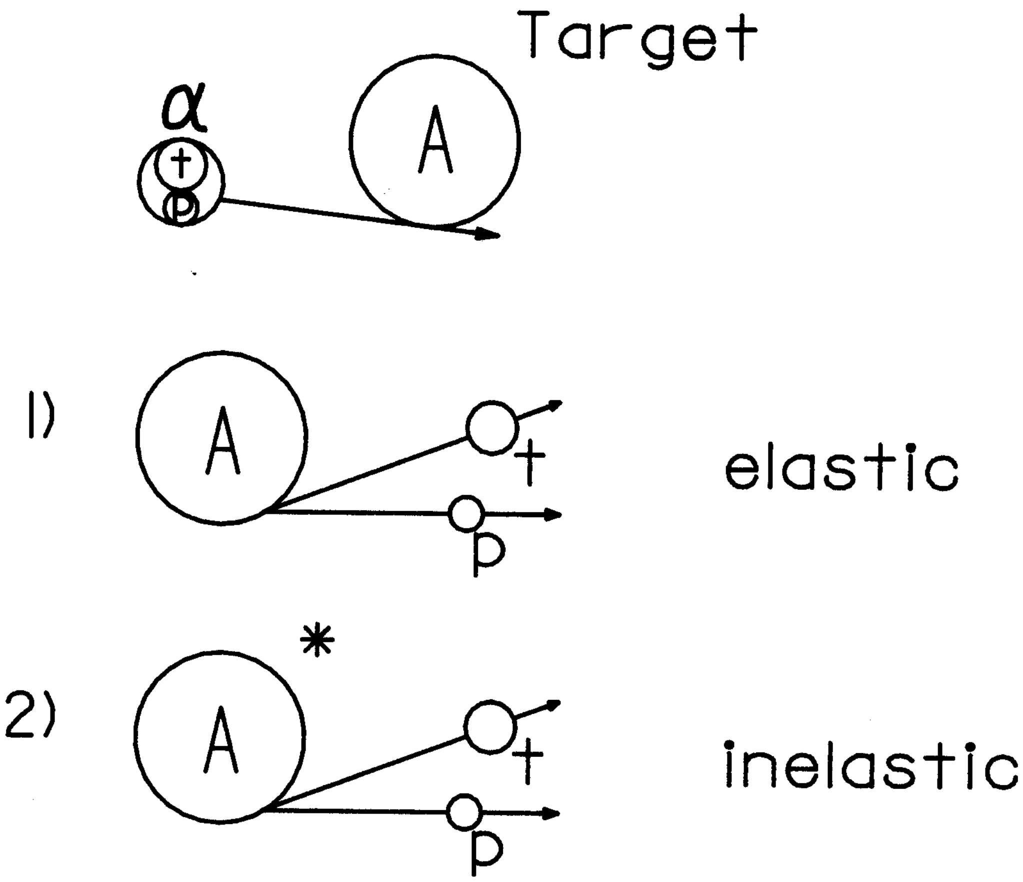

Figure IV.2

section for the interaction of the transferred nucleon x with the target A. A sharp cut-off geometrical model [B153] was used for $\sigma(xA)$. $\phi(q)$ is the wave function of the constituents of the projectile, q being the internal momentum in the projectile. We used a wave function of the Eckart form [Wu79] for $\phi(q)$. ρ is the phase space factor, for which an analytic expression [O165] was used. The constant c was determined by normalizing the elastic α-breakup calculation to the measured spectrum from the ^{148}Sm(α,t) reaction at a small scattering angle (5°) and a high excitation energy (28 MeV).

The high excitation energy parts of our spectra do not display any significant structure or peaks. This featureless character was confirmed up to especially high excitation energies ($\geq$ 35 MeV) in the case of the ^{148,154}Sm(α,t) reactions by measuring spectra with two (sometimes three) dipole field settings and then joining them together. The elastic breakup calculation gave an acceptable fit to the shape and magnitude over the entire high-excitation (E_x> 28 MeV) region of these spectra. In fact, it fitted the high-excitation regions of all the forward-angle spectra from the (α,t) reactions on all the Sm targets. (The (α,^{3}He) reactions were not measured for excitation energies above $\approx$15 MeV.)

It was found that the elastic α breakup calculation was not sufficient to account for the observed cross section at large angles (Θ= 18°-25°). So we also considered compound nucleus evaporation, which was found to be an important process at backward angles for ^{3}He-induced reactions [Aa84,Me85]. Such an evaporation process would give rise to an isotropic angular distribution in the center of momentum system, as was shown to be the case for ^{3}He [Aa84]. A Fermi-gas model was used by Aarts et al. [Aa84] to predict the compound nucleus evaporation in (^{3}He,dp) reactions. It was further shown through kinematics that the phase space for the evaporation process is the same as for the ^{3}He breakup. However, when the Fermi-gas model was used to calculate our stripping reaction background with a Fermi energy parameter of 42 MeV [Mo71] and a temperature of 8 MeV, it did not predict the shape or the magnitude of the cross section in the high-lying region of the spectrum.

So for the evaporation contribution to the background we arbitrarily used the magnitude of the background observed at 25° (corrected for the small α-breakup contribution at this angle). At high excitation energy, all of the cross section at 25° was assumed to be due to the evaporation and α-breakup processes. The evaporation cross section thus determined was taken to have the same magnitude and shape at all angles. At forward angles it was small compared with the elastic α-breakup yield.

A comparison of the full background calculation with spectra from the ^{148}Sm(α,t) reaction at various scattering angles is shown in Chapter V (Figure V.2). It is demonstrated there that the background calculation, which includes the large angle evaporation contribution, predicts the spectral shape as well as the magnitude of the cross section at high excitation energy reasonably well at all angles studied.

IV.2 SLICING AND FITTING

In extracting cross sections we again used a more systematic approach than had been the case in earlier work. In most previous analyses, it was assumed that the spectra consisted of a few broad structures which were then fitted by gaussian shaped peaks, generally of different widths [Ga81,Ga83]. An example of this approach is displayed in Figure IV.1. The peaks labeled A and B are gaussian peaks chosen by the authors to fit the gross structure at excitation energies above 3 MeV in the ^{144,148,152}Sm(^{3}He,α) [Ga81] reactions. This same fitting procedure was carried out at various scattering angles. The gaussian fits yielded cross sections. For the regions where the gaussians were fitted, angular distributions were produced by plotting the cross sections as a function of scattering angle.

The spectra from the present experiment may be divided into two regions, one where discrete distinguishable peaks were present and another where no distinguishable peaks could be observed. On the average, the discrete distinguishable peaks were in the excitation energy range of 0 to 2 MeV. By fitting them with gaussians, their angular distributions were obtained. The rest of the spectra, from about 2 to 15 MeV excitation energy, was analyzed using a "slicing" method to deduce cross sections. The slicing was in bins of 520 keV excitation energy, corresponding to twice the width of the experimental resolution. (Figure IV.3 displays bins of 1 MeV width for the sake of clarity.) Cross sections were obtained for each bin and the angular distributions were plotted. Other choices for the bin width were investigated and the results were checked with one another. Results of this comparison are given in Chapter V.

As discussed in Chapter III, the number by which one must multiply the DWBA calculation to fit a particular experimental angular distribution is called the spectroscopic strength C^2S; see equation (III.15). The goal is to obtain strength distributions (C^2S as a function of excitation energy) over a large excitation energy range (from ~2 to 15 MeV) for different ℓ-transfers. This was achieved by fitting the experimental angular distributions with the contributions from various ℓ-transfers calculated using DWBA. Because of the overlapping nature of the single-particle resonances, in general more than one ℓ-transfer contributed in each energy slice.

The fitting procedure was carried out by minimizing the following quantity [Be69,Ge70]:

$$e^2 = \alpha \sum_{j=1}^{N} \left((y(x_j) - y_j)/\Delta y_j\right)^2 \qquad \text{(IV.2)}$$

Figure IV.3

Illustration of the slicing of spectra into bins. A bin width of 1 MeV is used for clarity. The spectrum displayed is the triton spectrum from the ^{148}Sm(α,t)^{149}Eu reaction at 5°. The dotted curve is the total background that is obtained by the procedure described in the text.

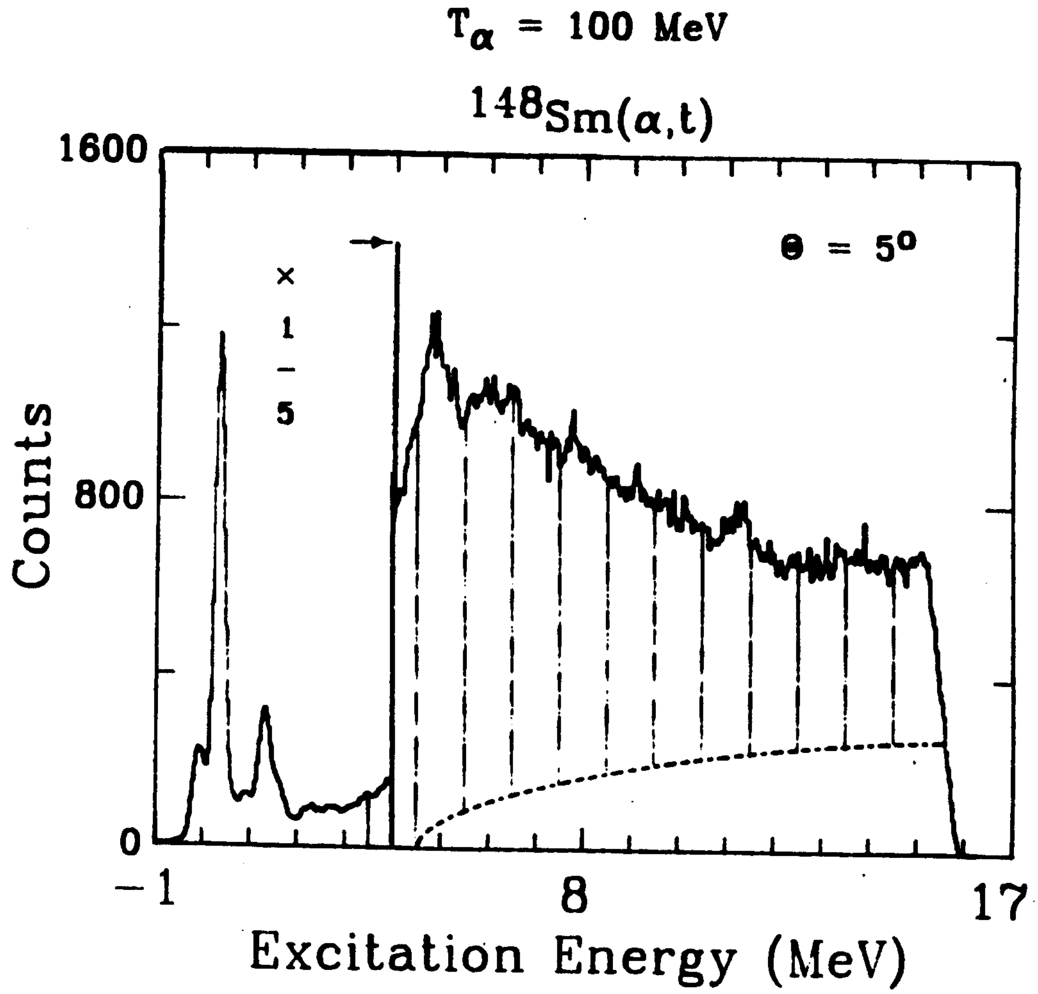

T_α = 100 MeV
$^{148}Sm(\alpha,t)$
1600
800
0
Counts
× 1/5
θ = 5°
−1
8
17
Excitation Energy (MeV)

Figure IV.3

Here, Δy_j is the error in the data point y_j; N is the number of data points, and $y(x_j)$ is defined such that

$$y(x_j) = \sum_{\ell_1=0}^{\ell_{max}} a(\ell_1,E_x)\ f(\ell_1,x_j,E_x) \qquad \text{(IV.3)}$$

$f(\ell_1,x_j,E_x)$ are the DWBA cross sections (calculated with the DWUCK4 [Ku84] code) at position x_j (where x_j may be either scattering angle or, equivalently, momentum transfer) for angular momentum transfer ℓ_1 and excitation energy E_x. The quantities $a(\ell_1,E_x)$ are free fitting parameters which contain the spectroscopic strength information. They are determined by minimizing (IV.2). The minimization procedure is carried out by finding the extremum of (IV.2) which is,

$$\partial e^2/\partial a_l = \alpha \sum_{j=1}^{N} 2(\ y(x_j) - y_j)/\Delta y_j^2\{f(l,x_j,E_x)\} = 0 \quad \text{(IV.4)}$$

To be sure that e^2 is a minimum, one must show that $\partial^2 e^2/\partial a_k \partial a_j > 0$ at the point where (IV.4) is true. Note that

$$\partial^2 e^2/\partial a_{l_1} \partial a_{l_2} = \alpha \sum_{i=1}^{N} 2f(l_1,x_i,E_x)f(l_2,x_i,E_x)/\Delta y_i^2 > 0 \quad \text{(IV.5)}$$

since $f(l,x_i,E_x) > 0$. This means that the extremum at (IV.4) is a minimum. So the solution of (IV.4) is

$$\sum_{i=1}^{N} \sum_{l_1=0}^{l_{max}} a(l_1,E_x)f(l_1,x_i,E_x)f(l_2,x_i,E_x)/\Delta y_i^2$$
$$= \sum_{i=1}^{N} y_i f(l_2,x_i,E_x) \qquad \text{(IV.6)}$$

(IV.6) is a matrix equation in which the known quantities are the data points y_i and the DWBA cross sections $f(\ell_i,x_j,E_x)$ at angles x_j for various ℓ-transfers and excitation energies. One can determine the parameters $a(\ell_1,E_x)$ by this means.

The above procedure of minimizing (IV.2) is known as the least squares χ^2 method of fitting [Be69,Ge70]. The quantity α in (IV.2) is $1/\nu$ where ν is the number of degrees of freedom in the fit (i.e., ν = N [data points] - number of fitting parameters). The quantity e^2 obtained by minimizing (IV.2) is commonly called the "reduced χ^2" or the "χ^2 per degree of freedom" and denoted by the symbol χ^2_ν. The χ^2 value is related to χ^2_ν by the equation;

$$\chi^2 = \nu \times \chi^2_\nu \qquad \text{(IV.7)}$$

A program called SMASHER was written to calculate the background, "slice" the spectra and fit them with the DWBA angular distributions. A program example to use SMASHER is given in Appendix II.

CHAPTER V

EXPERIMENTAL RESULTS

The experimental results from the stripping reactions (α,t) and (α,^{3}He) on targets of ^{144,148,152,154}Sm and ^{208}Pb are presented in this Chapter, which is separated into six sections. In the first section, the criterion used to accept a particular set of ℓ-transfers for a given angular distribution is discussed. Background subtraction is discussed in the second section. In particular, the α-breakup calculation described in Chapter IV, the method of normalization and the uncertainty in the background calculation are presented. In the third section, our data for the well resolved low-lying states excited in the ^{208}Pb(α,t)^{209}Bi and ^{208}Pb(α,^{3}He)^{209}Pb reactions are discussed. These data are used to test the DWBA calculations performed with the code DWUCK4 [Ku84], both as regards angular distribution shapes and as regards predicted magnitudes (by comparing spectroscopic strengths obtained from the present measurement with those from previous work). In the fourth section, the overall spectral shapes and their variations from isotope to isotope are discussed for the stripping reactions ^{144,148,152,154}Sm[(α,t) and (α,^{3}He)].

The results from the (α,t) and (α,^{3}He) reactions on ^{144,148,152,154}Sm are presented in the fifth and sixth sections, respectively. The spectroscopic strengths for the low-lying states of ^{145}Eu, ^{149}Eu and ^{145}Sm obtained from the present measurement, through the use of the ^{144}Sm(α,t)^{145}Eu, ^{148}Sm(α,t)^{149}Eu and ^{144}Sm(α,^{3}He)^{145}Sm reactions, respectively, are compared with those from previous measurements. The well resolved low-lying states of ^{145}Eu and ^{145}Sm are used to provide a check on how well the predicted DWBA angular distributions agree with the measured angular distributions. Spectroscopic strengths for the low-lying states of ^{153}Eu, ^{155}Eu, ^{149}Sm, ^{153}Sm and ^{155}Sm are reported for the first time. The spectroscopic strength distributions at high excitation energies for the proton and neutron states built on the samarium target ground states are also presented. The summed transition strengths (Σ C^2S) for ^{145}Eu obtained from this study are compared with those from previous work.

V.1 CRITERION FOR ACCEPTING ℓ-TRANSFERS

As described in the previous Chapter, the high-lying regions of the spectra generally involved a mixture of ℓ-transfers which were sought to be identified by fitting the measured angular distributions with a set of DWBA calculations for different ℓ-transfers. The strength parameters a_{ℓ}, which are related to the spectroscopic strengths, were determined by requiring that $\sum_{\ell} a_{\ell} \frac{d\sigma^{\ell}_{DWBA}}{d\Omega}$ (with the set of allowed ℓ's chosen on the basis of shell model considerations) provided the best fit to the shape and magnitude of the experimental angular distributions. The most common criterion used for this was the minimization of the quantity χ^2_{ν} ("reduced χ^2") defined by equations (IV.2 and IV.7). Each of the a_{ℓ} values corresponding to the minimum χ^2_{ν} has an associated error or width [Be69]. The error (da_{ℓ}) in the parameter a_{ℓ} was approximated by the standard deviation of the fit, which is determined by the inverse matrix elements of the fit; it was not weighted by χ_{ν}. This error is included, along with other experimental errors, in the results which are tabulated and plotted in the following sections of this Chapter. Since the calculated angular distributions for the different ℓ-transfers were rather similar, it was difficult to be sure that the correct set of ℓ-transfers was selected by following the best-fit criterion. Acceptance of slightly worse fits (slightly larger χ^2_{ν}) would have led to a different set of ℓ-transfers. In order to assess the difficulty of this procedure, the experimental angular distributions were also fitted with single ℓ-transfers. The a_{ℓ}'s and the χ^2_{ν} from these fits were obtained as a function of excitation energy.

For each combination of ℓ-transfers, the program calculates various local minima. The minimum χ^2_{ν} is the lowest of these local minima. This minimum χ^2_ν will be listed in all the tables in this Chapter except for Tables V.1, V.9 and V.12, while the χ^2_ν values corresponding to the other local minima will be listed in a few selected cases (Tables V.2, V.4, V.6 and V.8).

V.2 BACKGROUND CALCULATIONS

As mentioned in Chapter IV, the backgrounds used in previous experiments were often arbitrarily drawn by hand. In an attempt to be more systematic in handling the background, we peformed an α-breakup calculation, as described in Chapter IV, and the results are presented in this section.

We discuss first the results for the (α,t) reactions. With a single normalization constant for each reaction, the α-breakup calculation predicted the shape and magnitude of the high excitation energy region of the spectra reasonably well for forward angles out to 12°. The calculation predicted only about 50% of the observed cross section at 18° and about 10% at 25°. This suggested that while the breakup calculation may explain the background at forward angles, some other contribution was present at larger angles. As mentioned in Chapter IV, the unexplained part of the background at 18° and 25° was thought to be due to a compound nucleus evaporation process. However, a simple Fermi-gas calculation of this process did not explain the shape of the spectra in the high-lying region [Aa84,Me85]. Therefore the empirical shape and magnitude of the spectrum at large angles and high excitation energies was used for the contribution of this process, and the contribution was taken to be constant at all angles.

The net background was taken to be the sum of the α-breakup part and the angle-independent part. In Figure V.1, this net background is compared with the spectrum shape over a particularly large range of excitation energies measured in the ^{154}Sm(α,t)^{155}Eu reaction at 5°. We note that the background calculation follows the shape of the spectrum from about 28 MeV to about 43 MeV in excitation energy. Thus the excitation energy at which the background calculation is normalized to the spectrum is not important, as long as it is high enough. In fact, the normalization was done at an excitation energy of 30 MeV in ^{155}Eu, corresponding to a Q-value of -43.2 MeV. For the (α,t) reactions on the other three samarium isotopes, normalizations were carried out at the same Q-value of -43.2 MeV. We believe that this procedure led to greater consistency in the analysis, since the phase space of the α-breakup begins at the same Q-value for all of the europium isotopes. In order to keep the number of free parameters in the background calculation to a minimum, for each reaction we used a single normalization which was the average of the values obtained at different angles. (In the case of the ^{144}Sm(α,t)^{145}Eu reaction, the high-lying position of the

Figure V.1

Triton spectrum from the ^{154}Sm(α,t)^{155}Eu reaction at 5° showing the α-breakup plus evaporation calculation (dashed curve) for the background. Besides the Q-value energy scale along the horizontal axis, excitation energy scales (in MeV) are also shown in the figure. The sharp peaks near Q-values of -35 and -48 MeV are spurious and are due to a defect in the focal plane detector.

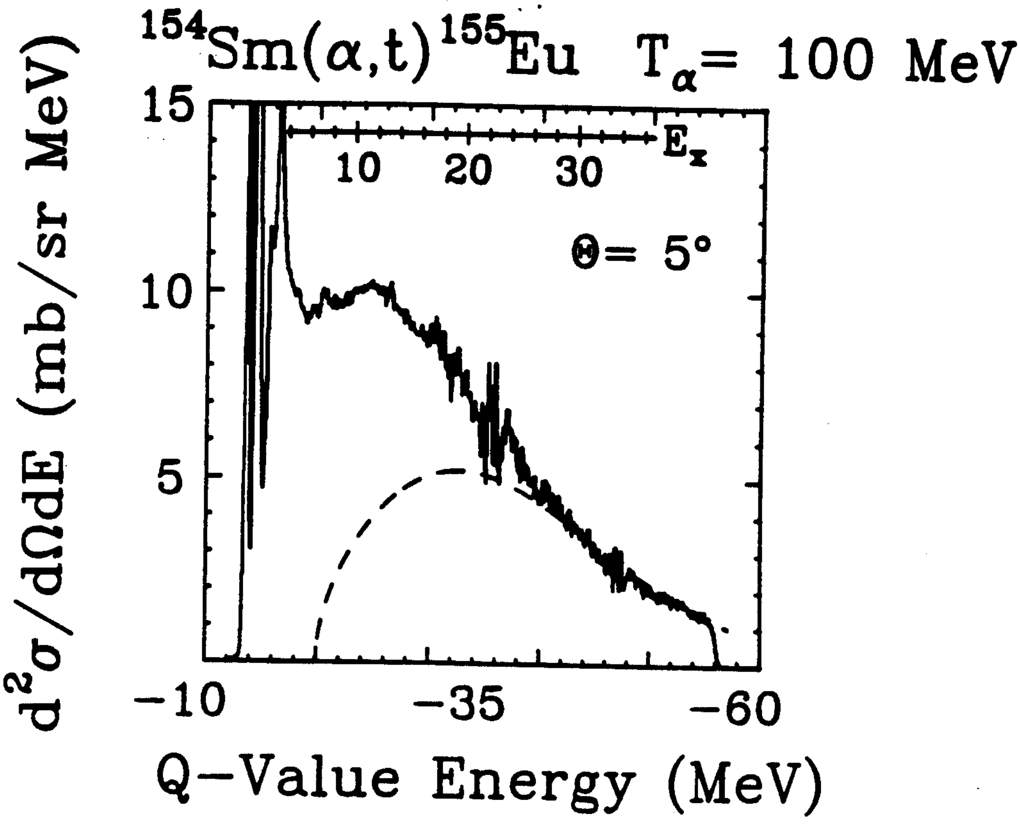
^{154}Sm(α,t)^{155}Eu T$_\alpha$= 100 MeV
d$^2\sigma$/dΩdE (mb/sr MeV)
15
10
5
10
20
30
E$_x$
Θ= 5°
−10
−35
−60
Q−Value Energy (MeV)

Figure V.1

spectrum was measured only at 7° and so no averaging was possible.)

The normalizations used for the α-breakup contributions in the ^{144,148,152,154}Sm(α,t)^{145,149,153,155}Eu reactions were 7.1, 8.7, 6.8 and 8.3, respectively. Note that they are slightly lower for the reactions on ^{144,152}Sm than for the reactions on ^{148,154}Sm. The uncertainties in the absolute cross sections for the reactions may contribute to these differences. We recall from Chapter II that for reactions on ^{152}Sm there is a 20% uncertainty in the absolute cross section values.

The results of the background calculation are compared with the measured spectra from the ^{148}Sm(α,t)^{149}Eu reaction at various angles in Figure V.2. The α-breakup contribution dominates at forward angles but falls at larger angles, as shown by the dot-dashed curves at 18° and 25°. The compound nuclear evaporation process, on the other hand, contributes very little to the background at forward angles ($\lesssim$ 12°) but dominates at 25°. Together, these two processes predict the spectrum shape as well as the magnitude of the cross section at high excitation reasonably well at all the angles studied.

Because the background calculation did not give a perfect fit to the high-lying part of the spectra at all angles and energies, an uncertainly is introduced into the cross section determination. Of course, the high-lying part of the spectra might not result solely from elastic α

Figure V.2

Triton spectra from the ^{148}Sm(α,t)^{149}Eu reaction at eight angles. The estimated total backgrounds are shown by the dashed curves. The α-breakup contributions at angles of 18° and 25° are shown by the dot-dashed curves. At more forward angles the contribution from the compound nucleus evaporation process is small relative to that from α-breakup and therefore the total background is essentially equivalent to the α-breakup contribution. Besides the Q-value energy scale along the horizontal axis, excitation energy scales (in MeV) are also shown in each panel of the figure.

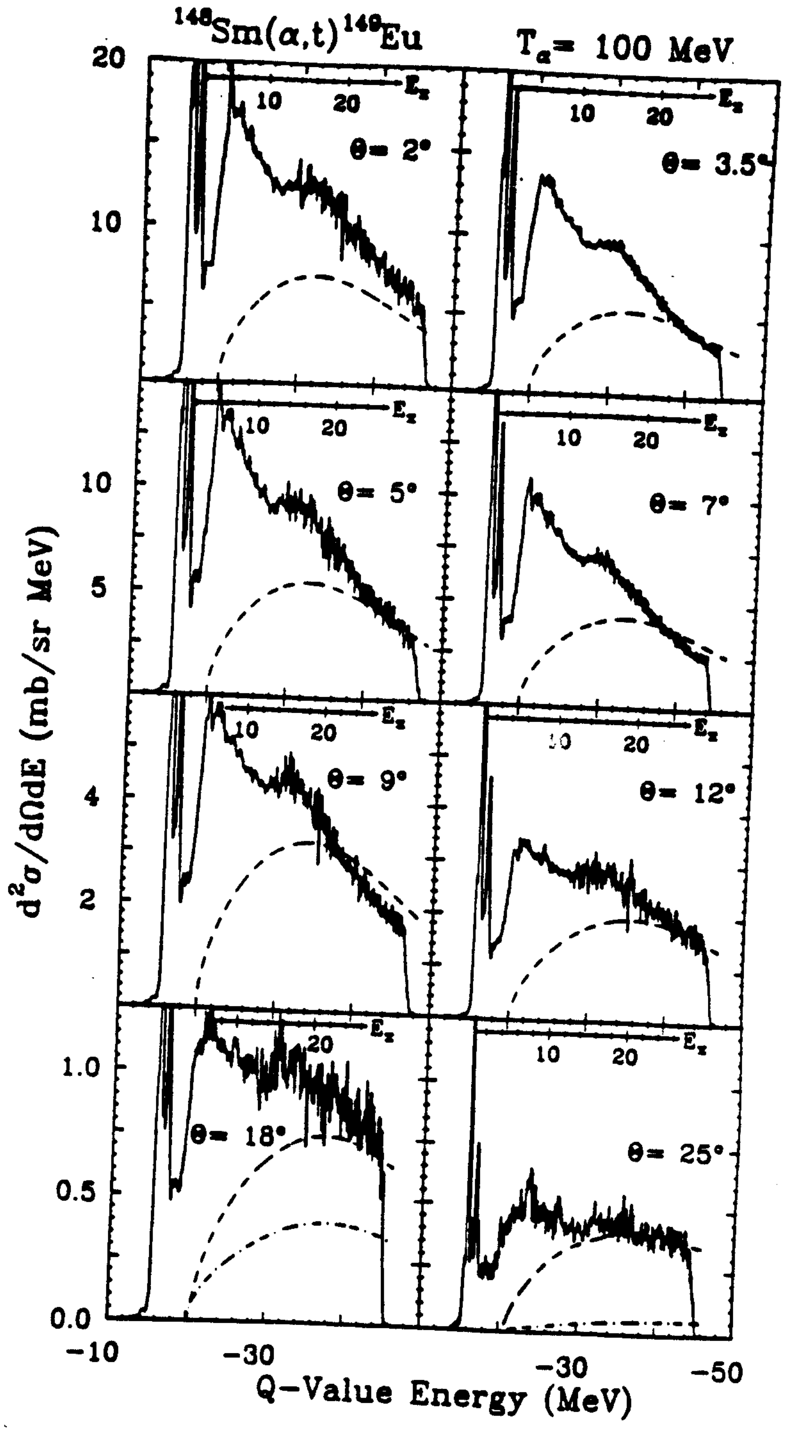
$^{148}Sm(\alpha,t)^{149}Eu$
T_α= 100 MeV
$d^2\sigma/d\Omega dE$ (mb/sr MeV)
Q–Value Energy (MeV)
θ= 2°
θ= 3.5°
θ= 5°
θ= 7°
θ= 9°
θ= 12°
θ= 18°
θ= 25°
E_x
10
20
0.0
0.5
1.0
2
4
5
10
20
−10
−30
−30
−50

Figure V.2

breakup and compound nuclear evaporation. There may be some single particle states or other background process which contribute to the spectrum in this region. However, until more definitive coincidence measurements are made, we assume that our normalization of the background calculation is reasonably correct.

The uncertainty in the background normalization contributes some uncertainty to the relative cross sections. We chose to take half of the percentage difference between the spectra and the predicted background at the position of normalization as the relative error. An interpolation of the error was carried out for all angles for which the measured spectra did not extend to an excitation energy high enough to reach the normalization point. Figure V.2 indicates that for ^{149}Eu, the cross sections at 2° and 9° would have the largest error bars, 13% and 12% respectively, since they are the angles for which the calculated backgrounds are furthest from the spectra at the normalization point (Q-value of -43.2 MeV, E_x= 27.7 MeV).

We now turn to the estimate of the backgrounds for the (α,^{3}He) reactions. The procedure used to calculate the α-breakup contribution was similar to that for the (α,t) reactions, except that the normalization was obtained in a different way. This was because no high-lying spectra (E_x> 15 MeV) were measured in the (α,^{3}He) case, partly due to the lack of time and partly due to experimental problems. The normalization for each target was obtained by assuming that the ratio of total yield to background in the (α, ^{3}He) reaction was the same as that in the (α,t) reaction at a selected angle (7°) and excitation energy (≈14 MeV). The normalizations used for the (α, ^{3}He) reactions on ^{144,148,152,154}Sm were 5.5, 6.3, 4.9 and 3.6, respectively. The evaporation part of the background was adjusted such that the ratio of total yield to background at 25° in the (α, ^{3}He) reaction was the same as in the (α,t) reaction.

As an example of the results obtained, the estimated backgrounds are compared with spectra from the ^{148}Sm(α, ^{3}He)^{149}Eu reaction at various angles in Figure V.3. The backgrounds estimated for the (α, ^{3}He) reactions on the other Sm targets showed the same behavior. The uncertainties of the background subtraction for the (α, ^{3}He) reactions were obtained in the same way as for the (α,t) reactions.

After the calculated backgrounds were subtracted from the measured spectra for both (α,t) and (α, ^{3}He) reactions, the remaining parts of the spectra were assumed to consist only of particle states populated by a direct nucleon transfer mechanism.

V.3 ^{208}PB(α,t)^{209}Bi AND ^{208}Pb(α, ^{3}He)^{209}Pb REACTIONS

Many single particle stripping reactions on ^{208}Pb which populate the low-lying states of ^{209}Bi and ^{209}Pb have been reported [Ma77], [Pe81,Ga85a]. In the present experiment, these states were measured by the (α,t) and (α, ^{3}He)

Figure V.3

Same as Figure V.2, but for the ^{148}Sm(α,^{3}He)^{149}Sm reaction. Besides the Q-value energy scale along the horizontal axis, excitation energy scales (in MeV) are shown in each panel of the figure. The break near the middle of the spectra is due to a defect in the focal plane detector.

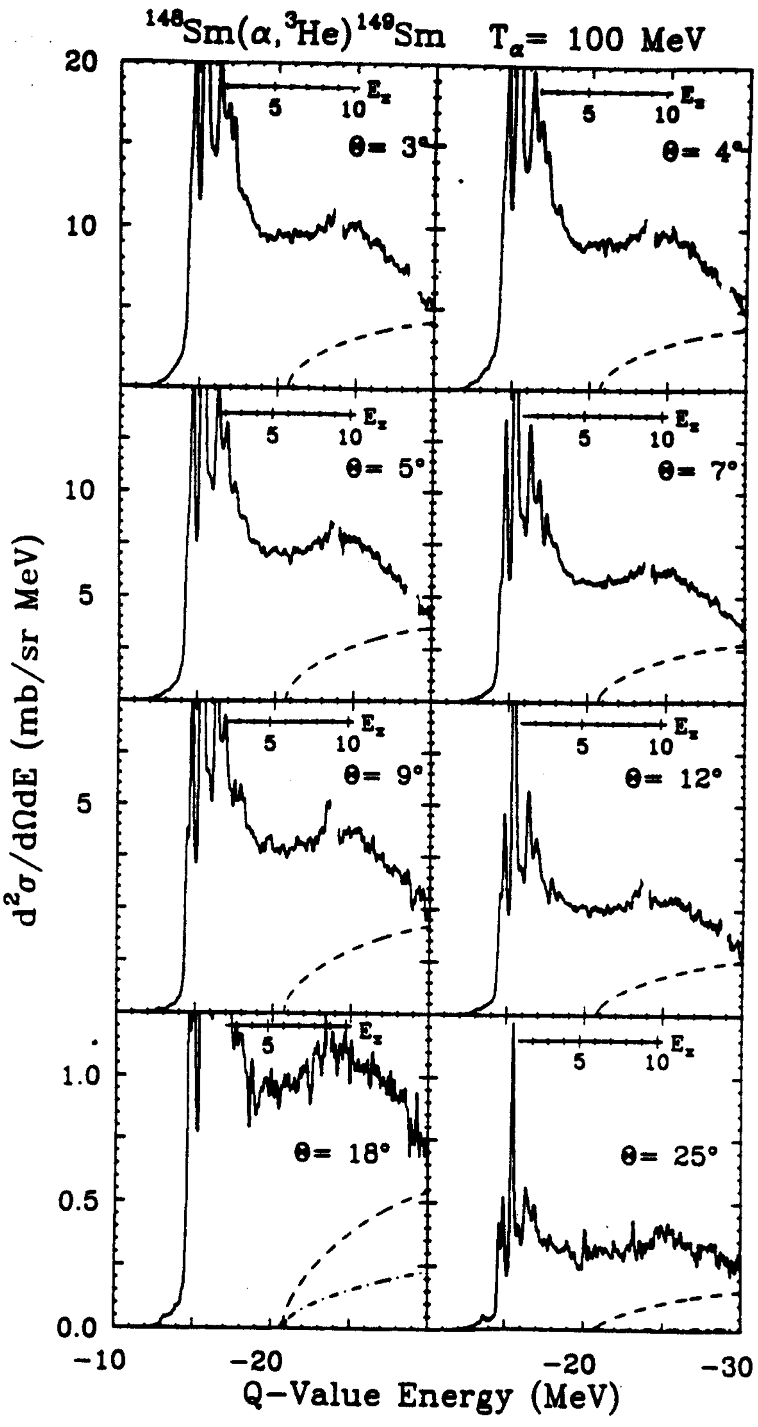
^{148}Sm(α,^{3}He)^{149}Sm T$_\alpha$= 100 MeV
d^{2}σ/dΩdE (mb/sr MeV)
Q-Value Energy (MeV)
20
10
10
5
5
1.0
0.5
0.0
-10
-20
-20
-30
E$_x$
5
10
θ= 3°
θ= 4°
θ= 5°
θ= 7°
θ= 9°
θ= 12°
θ= 18°
θ= 25°

Figure V.3

reactions on ^{208}Pb for three reasons. First, they are well separated even with the modest resolution available in the present experiment. Therefore they provide a check of how accurately the angular distributions predicted by the code DWUCK4 match the experimental angular distributions for states whose J^{π} values are well known. Second, the spectroscopic strengths (C^2S) measured for these states in this investigation can be compared with other work. Such a comparison provides a check on the overall normalization of the DWBA calculations, in particular the value of N (occurring in (III.15)) which in previous work [Ga85a] was determined to be 36. Third, the slicing method used for the higher excitation energy regions of the Sm and Eu isotopes (sections V.5.2 and V.6.2) can be tested by summing the angular distributions of two low-lying states to find whether the χ^2_{ν} fitting program can select the correct ℓ-transfers for this summed distribution.

Three distinct low-lying states are populated in both ^{209}Bi and ^{209}Pb, as shown in Figure V.4. We note that the resolution for the (α,^{3}He) reaction is somewhat better than that for the (α,t) reaction. This may be explained in the following way. The spectrograph was focused using the elastic peak. The spectrograph settings were then scaled according to the ratio of the rigidity of the particle of interest to that of the elastically scattered ^{4}He. The rigidity of ^{3}He is closer than that of the triton to the rigidity of ^{4}He. Thus the extrapolation is greater for

Figure V.4

Spectra from the $^{208}Pb(\alpha,t)^{209}Bi$ and $^{208}Pb(\alpha,{}^{3}He)^{209}Pb$ stripping reactions at a scattering angle of 5°.

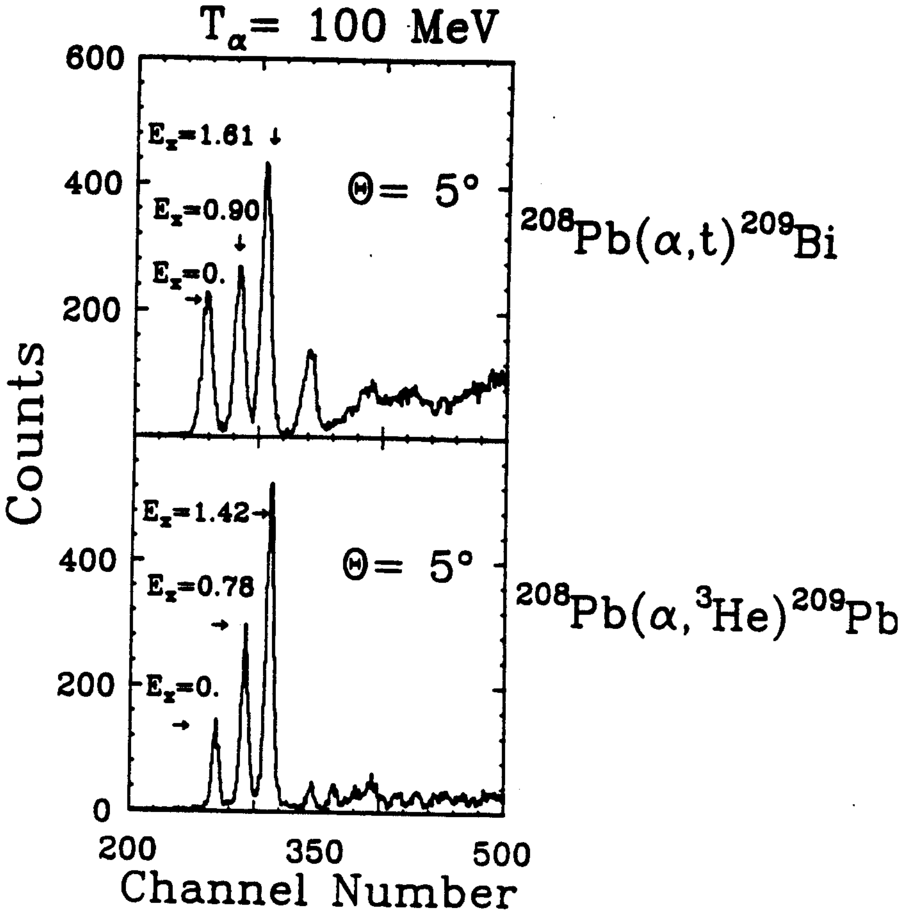

T_α= 100 MeV
Counts
Channel Number
600
400
200
0
200
350
500
E_x=1.61
E_x=0.90
E_x=0.
Θ= 5°
$^{208}Pb(\alpha,t)^{209}Bi$
E_x=1.42
E_x=0.78
E_x=0.
Θ= 5°
$^{208}Pb(\alpha,^3He)^{209}Pb$

Figure V.4

tritons, and this is the probable cause of the worse resolution.

The experimental angular distributions obtained for the low-lying states of ^{209}Bi and ^{209}Pb are shown in Figure V.5. DWBA calculations were made for both the ^{208}Pb(α,t)^{209}Bi and ^{208}Pb(α,^{3}He)^{209}Pb reactions using the optical model parameters listed in Chapter III (Table III.1). A different set of bound state parameters was used for ^{209}Bi (see footnote to Table III.1) [Ga85a]. Use of the first set of bound state parameters gave a low DWBA cross section so that the C^2S value obtained for the ground state of ^{209}Bi was significantly higher than unity (see column A in Table V.1). Recall that unity is the theoretical maximum, as shown by equation (III.16).

Results of the "minimum χ^2_ν" fits for the low-lying states of ^{209}Bi and ^{209}Pb are shown in Figure V.5. The fits have rather large χ^2_ν values ranging from about 2.3 to 8.5. The C^2S values obtained from these fits (using N=36) are listed in Table V.1. For ^{209}Bi, two sets of bound-state parameters, labeled A and B, were used. They are the first and the second set given in Table III.1. C^2S values from other recent measurements and from the Nuclear Data Sheets [Ma77] are also tabulated in Table V.1. We note that the C^2S values from the present experiment (with bound-state parameter set B for ^{209}Bi and A for ^{209}Pb) are slightly lower than the values from other recent work and that they are at the lower end of the range quoted by the Nuclear Data

Figure V.5

Angular distributions from the ^{208}Pb(α,t)^{209}Bi and ^{208}Pb(α,^{3}He)^{209}Pb reactions for low-lying proton and neutron states in the final nuclei. The ℓ-transfer and excitation energy (in MeV) are indicated in each panel. The solid curves are the normalized DWBA predictions for these ℓ-transfers.

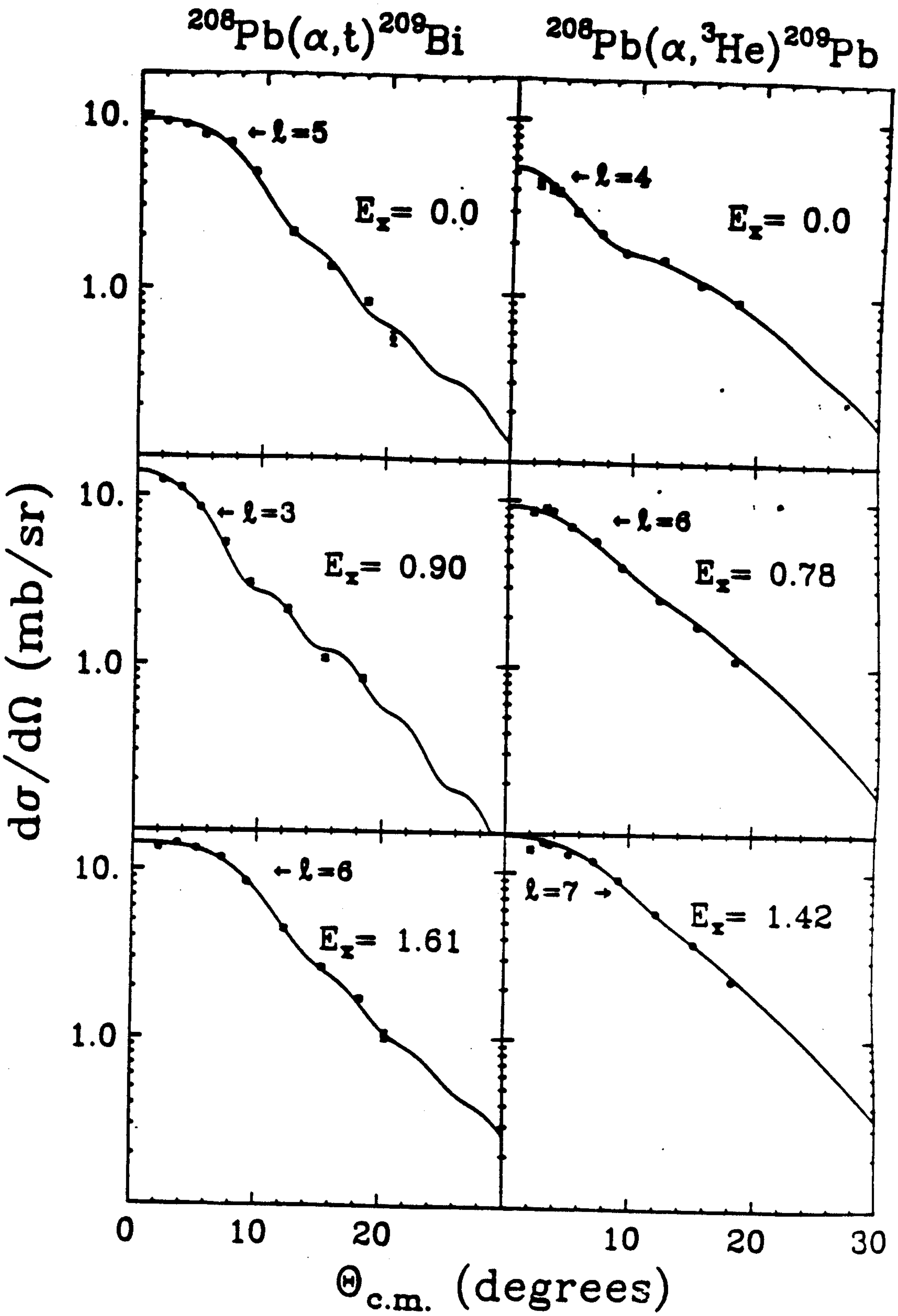

$^{208}Pb(\alpha,t)^{209}Bi$
$^{208}Pb(\alpha,{}^3He)^{209}Pb$
10.
1.0
← ℓ=5
E_x= 0.0
← ℓ=4
E_x= 0.0
← ℓ=3
E_x= 0.90
← ℓ=6
E_x= 0.78
← ℓ=6
E_x= 1.61
ℓ=7 →
E_x= 1.42
$d\sigma/d\Omega$ (mb/sr)
0
10
20
30
$\Theta_{c.m.}$ (degrees)

Figure V.5

Table V.1

List of the C^2S values obtained from the minimum-χ^2_ν fits to the angular distributions for low-lying states in ^{209}Bi and ^{209}Pb. The two columns labeled A and B are the results of using two different sets of bound state parameters given in Table III.1.

^{208}Pb$(\alpha,t)^{209}$Bi								^{208}Pb$(\alpha,{}^3$He$)^{209}$Pb					
This experiment					Other work		Nuclear Data Sheets	This experiment				Other work	Nuclear Data Sheets
		A	B							A			
E_x(MeV)	ℓ	C^2S^*	C^2S^*	nℓj	C^2S^a	C^2S^b	$C^2S^\dagger$	E_x(MeV)	ℓ	C^2S^*	nℓj	C^2S^c	$C^2S^\dagger$
0.00	5	1.44	0.60	$1h_{9/2}$	0.80	0.82	0.54-1.17	0.00	4	0.62	$2g_{9/2}$	0.83	0.66-1.08
0.90	3	0.78	0.53	$2f_{7/2}$	0.76	0.78	0.65-1.18	0.78	6	0.80	$1i_{13/2}$	0.86	0.75-1.52
1.61	6	0.68	0.53	$1i_{13/2}$	0.74	0.78	0.52-0.94	1.42	7	0.45	$1j_{15/2}$	0.58	0.53-1.38

a) [Ga 85a]
b) [Pe81]
c) [Ko74]
*) Present experimental work.
†) [Ma77]

Sheets. However, our C^2S values are consistent with the others within the range of uncertainty (15%) in the value of N at our energy. We conclude that although the absolute cross sections predicted by the DWBA calculations are slightly high, they are resonable. Our C^2S values could have been made higher by decreasing the value of N, but we decided it would be better to use the standard value than to increase the number of variable parameters in the analysis.

These data served to test, for cases where the correct answers were known, the reliability of ℓ-transfer values obtained by fitting measured angular distributions. Table V.2 lists the complete range of χ^2_ν values for different mixtures of ℓ-transfers for the three low-lying states in ^{209}Bi. We note that in all three cases, the correct (single) ℓ-transfer gives the minimum χ^2_ν and that the next nearest χ^2_ν corresponds to a mixture of ℓ-values that includes the correct ℓ-value. Also, the added mixture of other ℓ-transfers reduces the C^2S value for the ℓ-transfer selected by the minimum-χ^2_ν fit.

The need to test the slicing method used in sections V.5.2 and V.6.2 provided a further reason for studying the lead target. The angular distributions for two known low-lying states in ^{209}Bi and in ^{209}Pb were summed and the fitting program was used to analyze them. This procedure of decomposing the summed angular distribution of low-lying states reproduced, to some extent, the situation wherein

Table V.2

List of the possible C^{2}S values, using the ℓ-mixtures indicated, for the low-lying states in ^{209}Bi. The C^{2}S values are determined using the set B of bound state parameters (see Table V.1).

MeV		B			B		MeV		B			B	
E_x = 0.00	ℓ	C^{2}S	χ^2_ν	ℓ	C^{2}S	χ^2_ν	E_x = 0.90	ℓ	C^{2}S	χ^2_ν	ℓ	C^{2}S	χ^2_ν
	5	0.60	3.8	6 3	0.25 0.14	8.5		3	0.53	2.3	7 5 3	0.23 0.05 0.49	3.7
	6 5 4	0.12 0.30 0.03	4.4	7 4	0.12 0.15	16.		4 3	0.06 0.40	2.4	4	0.23	16.
	6 5	0.09 0.44	4.4	6	0.34	26.		6 3	0.02 0.50	3.0	5	0.54	82.
	6 5 3	0.11 0.39 0.02	5.0	7 3	0.18 0.25	31.		5 3	0.05 0.49	3.1	6	0.28	172.
	7 5	0.03 0.54	5.7	4	0.23	50.		7 3	0.01 0.51	3.2	7	0.27	308.
	6 4	0.20 0.09	5.8	7	0.34	134.							
	7 5 4	0.04 0.49 0.01	6.4	3	0.47	135.							

MeV		B			B			B			B	
E_x = 1.61	ℓ	C^{2}S	χ^2_ν	ℓ	C^{2}S	χ^2_ν	ℓ	C^{2}S	χ^2_ν	ℓ	C^{2}S	χ^2_ν
	6	0.53	3.7	7 5	0.27 0.48	8.5	5	0.94	67.	4	0.39	192.
	7 6	0.02 0.51	3.8	7 4	0.35 0.15	14.	7	0.52	67.	3	0.88	359.
	7 6 4	0.04 0.48 0.01	4.9	7 3	0.39 0.26	20.						

angular distributions of high-lying regions with unknown ℓ-transfers were fitted in order to determine the ℓ-transfers and their individual contributions to the cross section. It gave an indication of the accuracy of the fitting procedure in selecting an ℓ-transfer or a mixture of ℓ-transfers. Results obtained by using the minimum-χ_ν^2 method are shown in Table V.3. It is observed that the ℓ-transfers obtained by fitting the summed angular distribution are off by one unit from the correct ℓ values. This suggests that the selection of an ℓ-transfer made by the fitting procedure is probably only accurate to within ±1, consistent with the fact that the angular distribution shapes for neighboring ℓ-transfers are similar (see Figure III.2). Also, the fit to the summed angular distribution with the incorrect ℓ's has a χ_ν^2 value that is much smaller than the χ_ν^2 values for the individual angular distributions with the correct ℓ's. More importantly, the inaccuracy of selecting an ℓ-transfer implies that the C^2S values determined will not be valid, since they may be associated with the wrong ℓ-transfers. Table V.4 lists the range of χ_ν^2 values for the summed angular distribution in the case of ^{209}Bi for all combinations of ℓ-values from the set ℓ=3,4,5,6,7 which gave positive values for C^2S. Hence, the reader can evaluate the reliability of the ℓ-transfer values obtained by the fitting procedure.

Thus we see that C^2S values are hard to deduce in regions where different ℓ-transfers overlap (Tables V.3 and

Table V.3

Results of the analysis of the summed angular distributions of the first two low-lying state in ^{209}Bi and ^{209}Pb, when the ℓ-values were selected by the best-fit requirement. The results are compared with those obtained when each state was individually analyzed using the known ℓ-transfer. The χ^2_ν values of the fits are shown in parenthesis. The labels A and B refer to the two sets of bound state parameters used in the DWBA calculations (see Table V.1).

^{208}Pb(α,t)^{209}Bi						^{208}Pb(α,^{3}He)^{209}Pb					
E_x(MeV)	ℓ	C²S(Σ)† B	E_x(MeV)	ℓ	C²S(exp)†† B	E_x(MeV)	ℓ	C²S(Σ)† A	E_x(MeV)	ℓ	C²S(exp)†† A
			0.00	5	0.60(3.8)				0.00	4	0.62(2.6)
0.45	6	0.10(0.91)				0.39	5	0.40(0.61)			
	4	0.39					7	0.10			
			0.90	3	0.53(2.3)				0.78	6	0.80(8.5)

† Summing the first two low-lying states.

†† C²S values carried over from Table V.1.

Table V.4

List of the extracted C^2S values, for the summed angular distribution of the first two low-lying states in ^{209}Bi, when the ℓ-mixtures were fixed at the values indicated. The correct ℓ-values are 5 and 3.

$E_x = 0.45$ MeV	ℓ	C^2S	χ^2_ν	ℓ	C^2S	χ^2_ν
	6 4	0.10 0.39	0.91	6 3	0.27 0.61	1.5
	5 4	0.33 0.33	0.96	5 3	0.70 0.41	1.6
	6 4 3	0.14 0.30 0.15	0.97	7 5 3	0.03 0.60 0.45	1.7
	6 5 4	0.07 0.13 0.36	0.99	4	0.46	2.0
	6 5 4 3	0.10 0.15 0.26 0.16	1.00	7 3	0.19 0.07	4.3
	7 5 4	0.02 0.25 0.35	1.0	5	1.2	8.5
	5 4 3	0.34 0.31 0.03	1.1	3	1.0	18.
	7 5 4 3	0.03 0.28 0.30 0.07	1.2	6	0.63	34.
	7 4	0.06 0.42	1.2	7	0.61	86.
	6 5 3	0.15 0.33 0.51	1.4			

V.4) but that the correct ℓ-transfer and C^2S value are obtained by the fitting procedure in regions where only a single ℓ-transfer is present (Table V.2). Keeping these conclusions in mind, we shall now proceed in attempts to obtain the spectroscopic strength for single-particle states built on the ground states of the samarium targets.

V.4 SPECTRA FROM NUCLEON-TRANSFER REACTIONS ON SAMARIUM

Spectra at 7° from (α,t) and $(\alpha,{}^3He)$ reactions on $^{144,148,152,154}Sm$ targets are displayed in Figures V.6a and V.6b, respectively. The (α,t) reaction populates proton states in europium and the $(\alpha,{}^3He)$ reaction populates neutron states in samarium. We observe differences among the proton and neutron single particle states as a function of deformation (which increases with mass for the nuclei considered here).

Figure V.6a shows the presence of a gross structure (labeled A) just to the right of a pronounced minimum in all four Eu nuclei. This structure occurs at around a Q-value of -23 MeV for ^{145}Eu, corresponding to E_x= 6.4 MeV. As the deformation increases from ^{145}Eu to ^{155}Eu, the gross structure "A" moves closer to the corresponding ground state. Accordingly, it resides in the unbound region of the spectrum for $^{145,149}Eu$ and in the bound region of the spectrum for $^{153,155}Eu$.

Figure V.6a

Triton spectra at 7° for proton states excited by the ^{144,148,152,154}Sm(α,t)^{145,149,153,155}Eu reactions. The horizontal scale gives the reaction Q-value (in MeV). The corresponding excitation energies in the residual nucleus (in MeV) is also shown in each panel of the figure. The α-breakup plus evaporation calculation is shown as the dashed curve.

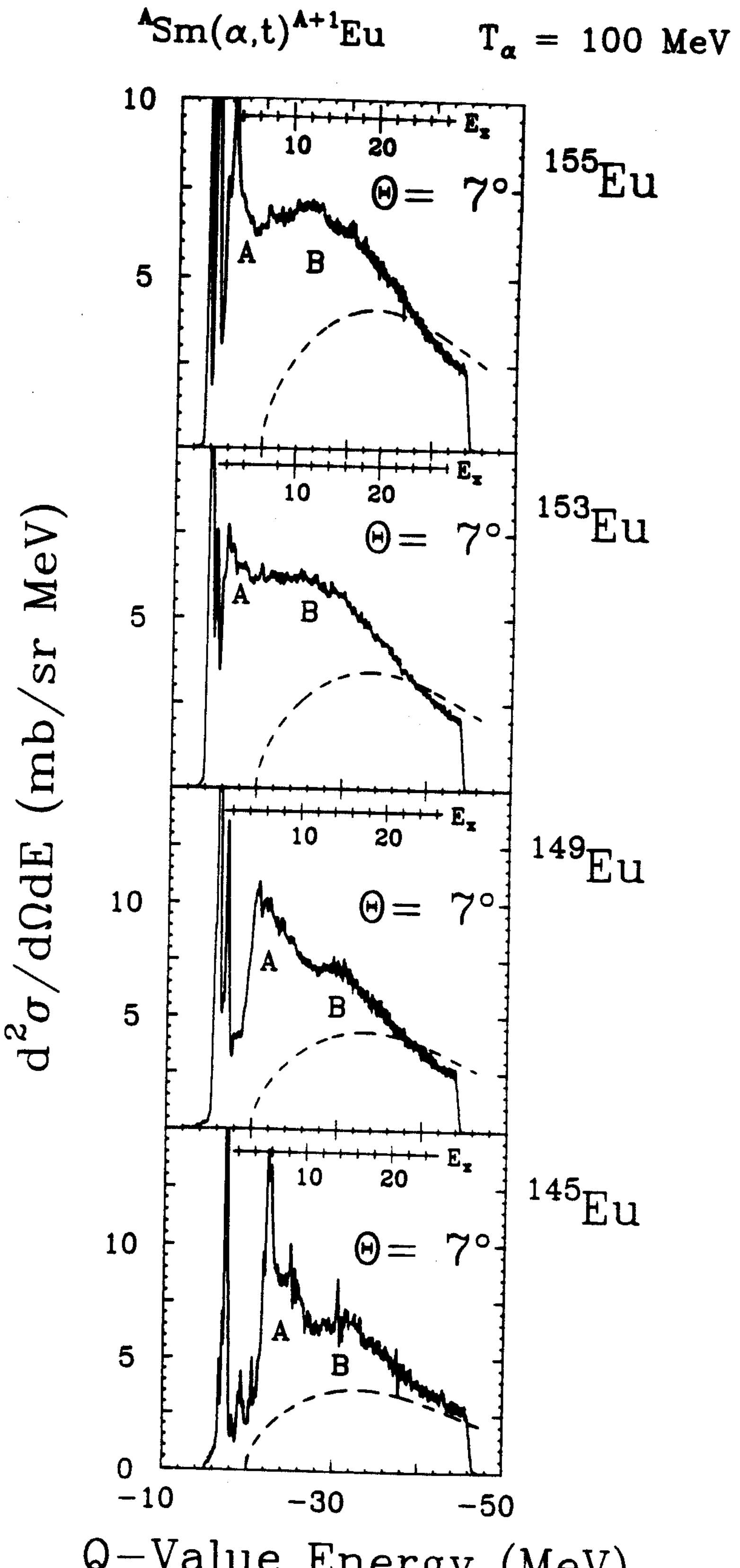

$^{A}Sm(\alpha,t)^{A+1}Eu$
T_α = 100 MeV
^{155}Eu
^{153}Eu
^{149}Eu
^{145}Eu
Θ= 7°
A
B
E_x
10
20
0
5
10
−10
−30
−50
$d^2\sigma/d\Omega dE$ (mb/sr MeV)
Q−Value Energy (MeV)

Figure V.6a

Figure V.6b

Spectra of ^{3}He at 7° for neutron states excited by the ^{144,148,152,154}Sm(α,^{3}He)^{145,149,153,155}Sm reactions. The horizontal scale gives the reaction Q-value (in MeV). Excitation energy (in MeV) is also shown in each panel of the figure. The break near the middle of the spectra is due to a defect in the focal plane detector. The α-breakup plus evaporation calculation is shown as the dashed curve.

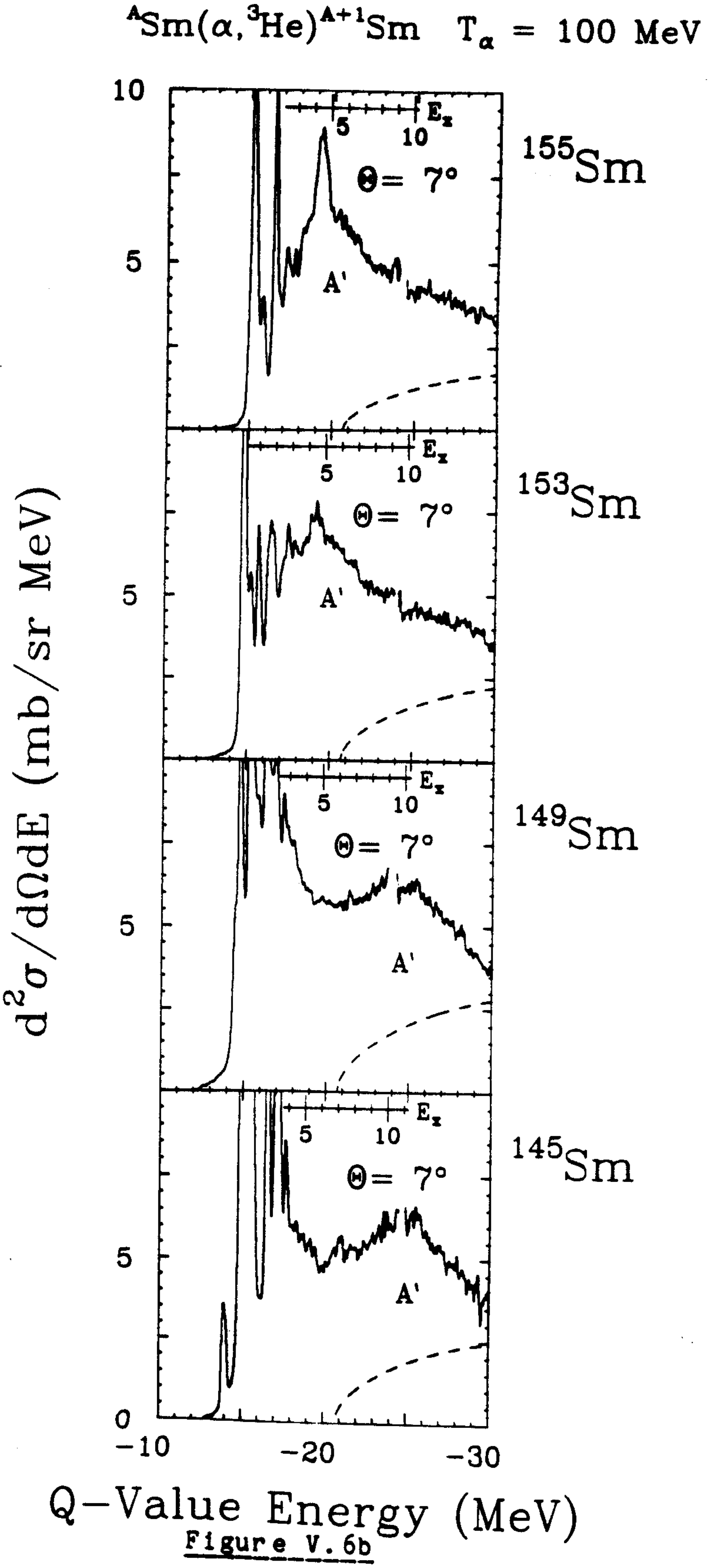

^{A}Sm(α,^{3}He)$^{A+1}$Sm T_α = 100 MeV
$d^2\sigma/d\Omega dE$ (mb/sr MeV)
10
5
0
E_x
5
10
Θ= 7°
A'
^{155}Sm
^{153}Sm
^{149}Sm
^{145}Sm
−10
−20
−30
Q−Value Energy (MeV)

Figure V.6b

There is also a second gross structure "bump", labeled "B" in Figure V.6a, that is centered at a Q-value of about -32 MeV in ^{145}Eu (E_x= 15 MeV). It resides in the unbound region of excitation energy in all four Eu isotopes. This bump also moves closer to the ground state as the deformation increases.

We also observe a gross structure, labeled "A'" in Figure V.6b, around the -25 MeV Q-value region (E_x≈ 11 MeV) in the ^{145}Sm spectrum. This gross structure also moves closer to the ground state as the deformation increases in the odd-mass Sm nuclei. It resides in the unbound region of the spectrum for ^{145,149}Sm and in the bound region of the spectrum for ^{153,155}Sm.

The ℓ-transfers in each region of the spectra will be determined by the fitting procedure (to within an uncertainty of ±1, as discussed before) in the third section for the (α,t) reactions and in the fourth section for the (α,^{3}He) reactions. Thus the ℓ-transfer(s) associated with each of the gross structure "bumps" will be identified.

V.5 ^{144,148,152,154}Sm(α,t)^{145,149,153,155}Eu REACTIONS

This discussion of the results from the (α,t) reactions on the samarium isotopes is divided into two parts:

1) The results for the low-lying states, including the extraction of angular distributions, assignment of ℓ-transfers and determination of C^2S values.

2) The results for the high-lying portion of the spectra, including the extraction of angular distributions using the "slicing" method described in Chapter IV and the determination of the C^2S distribution as a function of excitation energy for different ℓ-transfers.

V.5.1 Low-Lying States in $^{144,148,152,154}Sm(\alpha,t)^{145,149,153,155}Eu$

The low-lying portions of the energy spectra from the (α,t) reactions on ^{144,148,152,154}Sm are displayed in Figure V.7. It is clear from this figure and an examination of other work [Tu80], that in the case of ^{145}Eu the states are well separated up to an excitation energy of 1.2 MeV, whereas the states in the other three nuclei are not well resolved. With increasing mass, and thus increasing deformation of the isotope, the density of low-lying levels also increases. So the levels are not well resolved within our limited experimental resolution. The angular distributions obtained by fitting gaussians to the (mostly) unresolved collection of low-lying states are shown in Figure V.8. In principle, the fitting program should pick out the correct mixture of ℓ-transfers for states within a peak. If the decomposition works well for the low-lying states we may be more confident about applying this method to higher lying regions.

Figure V.7

Triton spectra at 5° showing the low-lying proton states populated by the $^{144,148,152,154}Sm(\alpha,t)^{145,149,153,155}Eu$ stripping reactions.

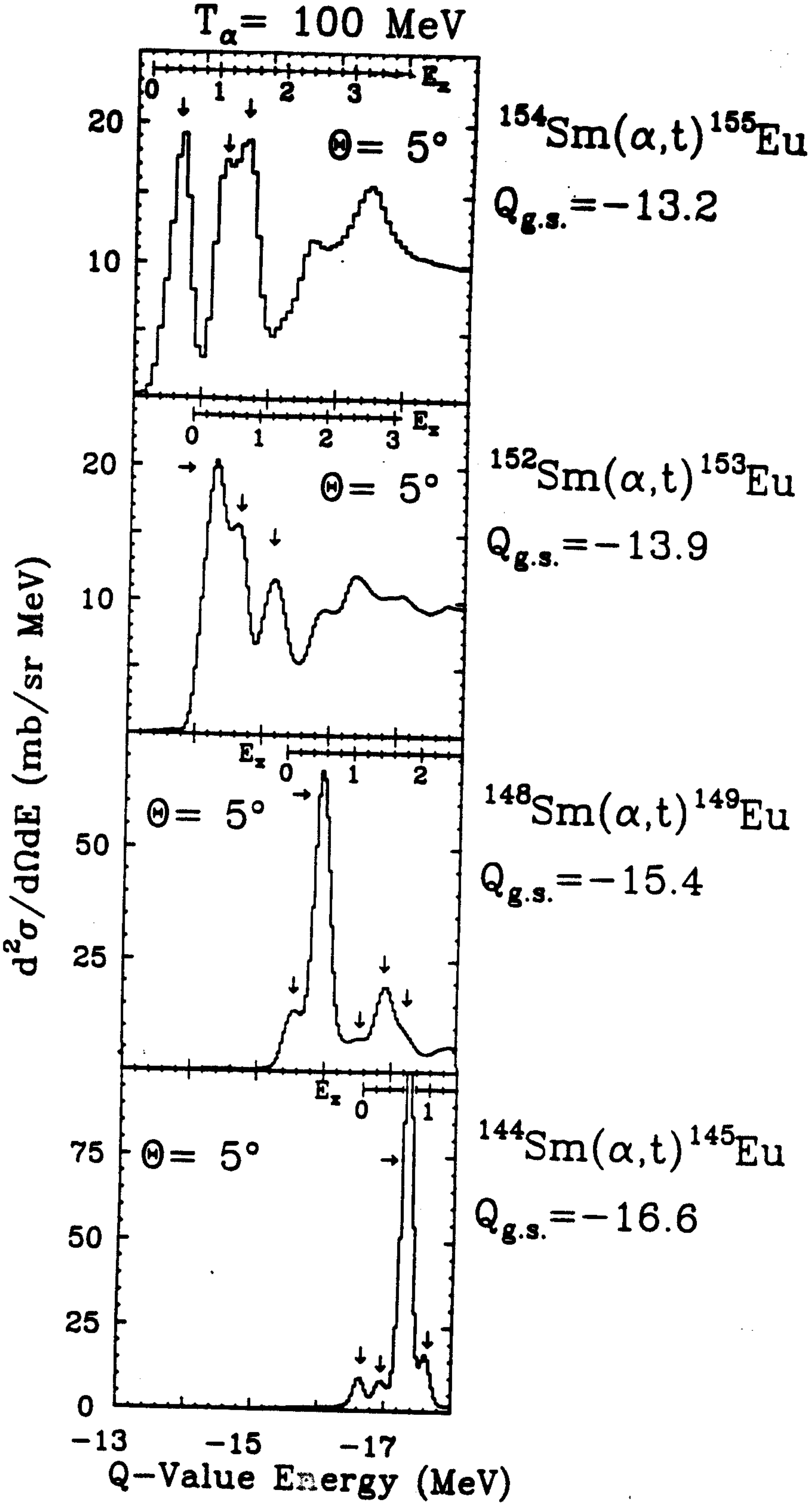
T_α = 100 MeV
E_x
0
1
2
3
Θ= 5°
^{154}Sm(α,t)^{155}Eu
$Q_{g.s.}$=−13.2
^{152}Sm(α,t)^{153}Eu
$Q_{g.s.}$=−13.9
^{148}Sm(α,t)^{149}Eu
$Q_{g.s.}$=−15.4
^{144}Sm(α,t)^{145}Eu
$Q_{g.s.}$=−16.6
20
10
50
25
75
0
$d^2\sigma/d\Omega dE$ (mb/sr MeV)
−13
−15
−17
Q−Value Energy (MeV)

Figure V.7

Figure V.8

Angular distributions of some low-lying peaks (indicated with arrows in Figure V.7) which are excited in ^{145,149,153,155}Eu. The curves are the minimum-χ^2_ν fits with DWBA predictions; the corresponding ℓ values are indicated.

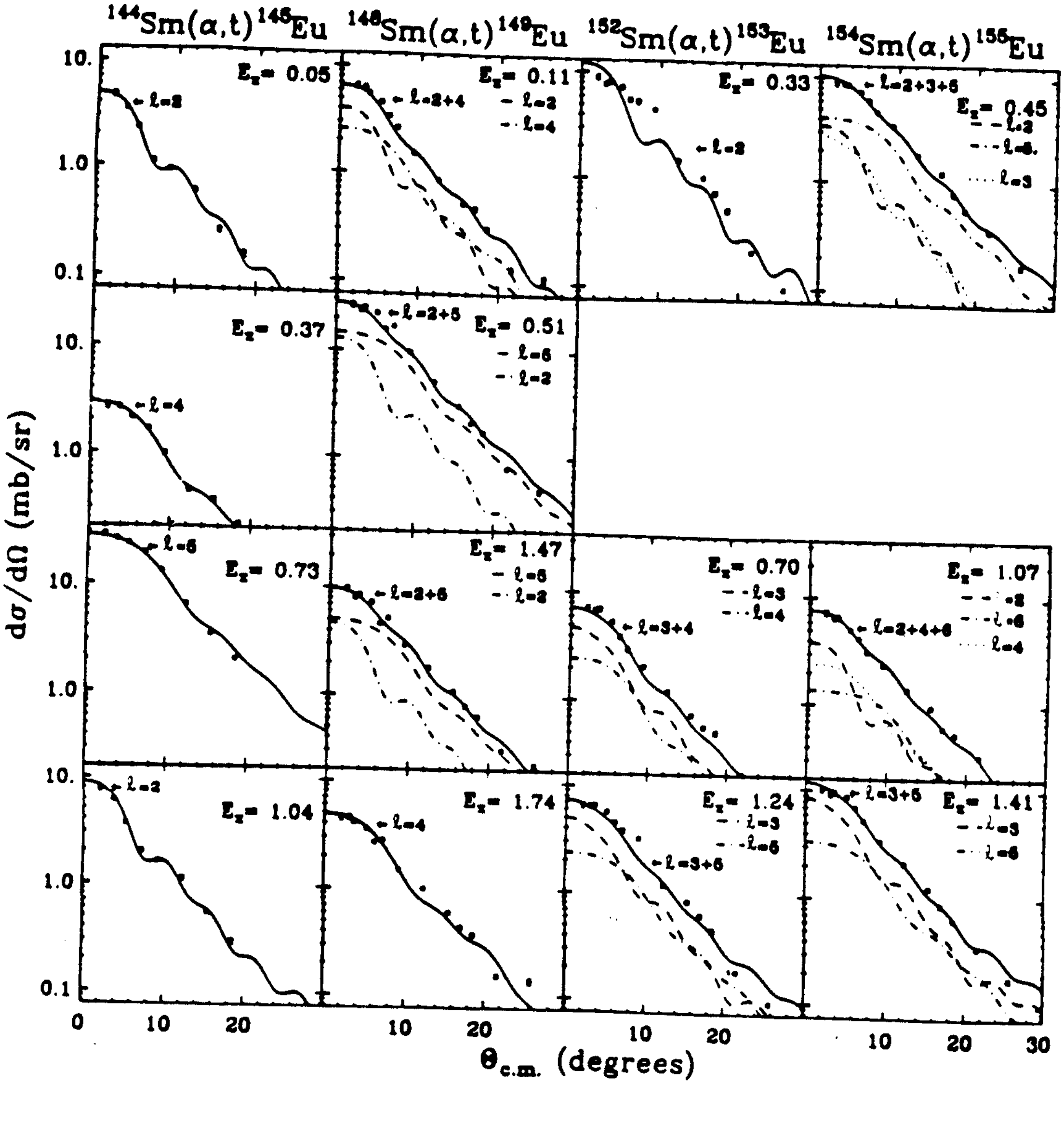

^{144}Sm(α,t)^{145}Eu
^{148}Sm(α,t)^{149}Eu
^{152}Sm(α,t)^{153}Eu
^{154}Sm(α,t)^{155}Eu
E$_x$= 0.05
ℓ=2
E$_x$= 0.11
ℓ=2+4
ℓ=2
ℓ=4
E$_x$= 0.33
ℓ=2
E$_x$= 0.45
ℓ=2+3+5
ℓ=2
ℓ=5
ℓ=3
E$_x$= 0.37
ℓ=4
E$_x$= 0.51
ℓ=2+5
ℓ=5
ℓ=2
E$_x$= 0.73
ℓ=5
E$_x$= 1.47
ℓ=2+5
ℓ=5
ℓ=2
E$_x$= 0.70
ℓ=3+4
ℓ=3
ℓ=4
E$_x$= 1.07
ℓ=2+4+6
ℓ=2
ℓ=6
ℓ=4
E$_x$= 1.04
ℓ=2
E$_x$= 1.74
ℓ=4
E$_x$= 1.24
ℓ=3+5
ℓ=3
ℓ=5
E$_x$= 1.41
ℓ=3+5
ℓ=3
ℓ=5
10.
1.0
0.1
dσ/dΩ (mb/sr)
0
10
20
30
θ$_{c.m.}$ (degrees)

Figure V.8

The Z value (proton number) of europium is 63. In the simple shell model theory, the $1g_{9/2}$ orbit is filled at Z=50. The next subshell (between Z=50 and Z=82) contains the single-particle orbits $1g_{7/2}$, $2d_{5/2}$, $1h_{11/2}$, $2d_{3/2}$ and $3s_{1/2}$ [Bo75a]. It is in these orbits that the 13 valence protons of Eu (outside the Z=50 shell closure) are distributed to form, by coupling with the valence neutrons outside the N=82 shell closure, the low-lying levels of the Eu isotopes. That is the picture according to the spherical shell model which, however, is not valid for the heavier Eu isotopes because of the effects of deformation. The Nilsson model, which incorporates these effects, shows that the single-particle orbits shift in energy depending upon the deformation. The energies of the lower orbits in the next higher subshell (above Z=82), $2f_{7/2}$, $1h_{9/2}$ and $1i_{13/2}$, decrease as the deformation increases, so these orbits can occur at the same energy as the subshell that contains the $1g_{7/2}$, $2d_{5/2}$, $1h_{11/2}$, $2d_{3/2}$ and $3s_{1/2}$ orbits. Therefore the ℓ-transfers expected in proton transfer to the low-lying states in the lighter europium isotopes ^{145,149}Eu are 2, 4 and 5 ($2d_{5/2}$, $2d_{3/2}$, $1g_{7/2}$, $1h_{11/2}$ proton excitations) whereas those expected in ^{153,155}Eu are 2, 3, 4, 5 and 6 ($2d_{5/2}$, $2d_{3/2}$, $2f_{7/2}$, $1g_{7/2}$, $1h_{11/2}$, $1h_{9/2}$ and $1i_{13/2}$ proton excitations) [Bo75a]. The $\ell=0$ transfer corresponding to the $3s_{1/2}$ proton excitation is weak at our high bombarding energy (see Figure III.2), so this ℓ-transfer was not included in the analysis.

We now present the results for the four Eu isotopes individually. In this discussion the reader should remember that the ability to select an ℓ-transfer (and hence to determine the C^2S values) using the minimum-χ^2_ν criterion, when mixing with other ℓ-transfers is involved, is probably accurate only to within ±1. Also, it should be noted that in addition to allowing the above mentioned set of ℓ-transfers to fit each of the low-lying peaks, each peak was also fitted separately by each of the individual ℓ-transfers from that set. This allows the reader to better evaluate the reliability of the ℓ-transfer values obtained from the fit and to have available the C^2S values if a different ℓ-mixture is assumed.

a) Low-lying states in ^{145}Eu

Since the low-lying states of ^{145}Eu were well resolved in the present experiment, the angular distributions measured for them provided a means for checking the angular distributions calculated by the code DWUCK4, just as in the case of the low-lying states of ^{209}Bi and ^{209}Pb discussed before. In addition, the spectroscopic strengths obtained were compared with previous measurements [Tu80,Ga85a].

The four states analyzed are indicated by arrows in Figure V.7. By an examination of the Nilsson model predictions [Bo75a], we see that ℓ-transfers of 2, 4 and 5 are the only possibilities for the low-lying states of ^{145}Eu (see discussion above). These ℓ-transfers were used to fit the angular distributions for the low-lying states using the "minimum χ^2_ν" criterion. The fits are shown in Figure V.8 and the extracted C^2S values in Table V.5, where the χ^2_ν values from the fits are shown in parenthesis.

Table V.6 lists the range of χ^2_ν values for the four low-lying states for all combinations of ℓ values from the set ℓ=2,4,5 which gave positive values for C^2S. (A negative value for C^2S is, of course, unphysical.) We note that, just as was the case for the low-lying states of ^{209}Bi, the χ^2_ν value nearest to the minimum χ^2_ν corresponds to a mixture of ℓ-values which includes the one identified as the correct ℓ-value by the best fit (minimum χ^2_ν). Also, as we would expect, the effect of the additional ℓ-values in the mixture is to reduce the C^2S value for the ℓ-transfer which corresponds to the best fit.

Table V.7 displays the C^2S values obtained when the angular distribution for each state was fitted with a single ℓ-transfer chosen from the allowed set (ℓ=2, 4 or 5 in the case of ^{145}Eu). At least some of these single-ℓ fits are clearly unphysical, since they give C^2S values considerably above the theoretical maximum (unity).

As shown in Table V.5, the results from the present experiment agree quite well with those from previous measurements. The states at E_x= 0.05 and 0.37 MeV have strengths quite close to the values determined in previous measurements, while the states at E_x= 0.73 and 1.04 MeV have

Table V.5

List of the spectroscopic strengths (C^2S) obtained from minimum-χ^2_ν fits for the low-lying states of ^{145,149,153,155}Eu. The χ^2_ν values of the fits are given in parenthesis.

	This experiment				Nuclear Data Sheets		Other work		
Pk #	E_x(MeV)	ℓ	$C^2S(\mathrm{exp})^\dagger$	χ^2_ν	E_x(MeV)	nℓj	C^2S	C^2S	Final Nucleus
1	0.05	2	0.31	(4.2)	0.	$2d_{5/2}$	0.37^a	0.33^b	
2	0.37	4	0.24	(1.8)	0.329	$1g_{7/2}$	0.24	0.17	
3	0.73	5	0.70	(6.9)	0.716	$1h_{11/2}$	0.98	0.82	^{145}Eu
4	1.04	2	0.63	(4.0)	1.042	$2d_{3/2}$	0.74	0.98	
1	0.11	2	0.25	(32.)	0.	$2d_{5/2}$	0.22^c		
		4	0.24		0.15	$1g_{7/2}$	0.12		
2	0.51	5	0.42	(36.)	0.496	$1h_{11/2}$	0.63		
		2	0.82						
3	1.07	2	0.08	(16.)	0.811	$2d_{5/2}$	0.03		^{149}Eu
		5	0.08		0.876	"	0.04		
					1.221	"	0.21		
4	1.47	2	0.33	(22.)	1.31	$2d_{5/2}$	0.01		
		5	0.14		1.399	$2p_{1/2}$	0.08		
					1.440	$2p_{1/2}$	0.07		
					1.503	$1h_{11/2}$	0.11		
5	1.74	4	0.42	(27.)					
1	0.33	2	0.70	(101.)					
2	0.70	4	0.25	(36.)					^{153}Eu
		3	0.11						
3	1.24	5	0.08	(49.)					
		3	0.12						
1	0.45	5	0.15	(7.7)					
		3	0.07						
		2	0.20						
2	1.07	6	0.05	(7.6)					^{155}Eu
		4	0.26						
		2	0.23						
3	1.41	5	0.11	(9.1)					
		3	0.21						

a) [Ga85a]; b) [Tu80]; c) [St79]; † Using the minimum χ^2_ν.

Table V.6

List of the possible C^2S values, with the ℓ-mixtures indicated, for the low-lying states in ^{145}Eu.

MeV							MeV						
E_x = 0.05	ℓ	C^2S	χ^2_ν	ℓ	C^2S	χ^2_ν	E_x = 0.37	ℓ	C^2S	χ^2_ν	ℓ	C^2S	χ^2_ν
	2	0.31	4.2	4	0.23	44.		4	0.24	1.8	5	0.06	8.8
	5 2	0.01 0.28	4.9	5	0.06	59.		5 4	0.01 0.20	3.2	2	0.29	62.
	4 2	0.03 0.27	5.4					5 2	0.05 0.05	7.8			
E_x = 0.73	ℓ	C^2S	χ^2_ν	ℓ	C^2S	χ^2_ν	E_x = 1.04	ℓ	C^2S	χ^2_ν	ℓ	C^2S	χ^2_ν
	5	0.70	6.9	4	2.9	34.		2	0.63	4.0	4	0.40	41.
	5 2	0.68 0.10	7.9	2	3.6	165.		5 2	0.02 0.48	4.4	5	0.10	51.
								4 2	0.10 0.48	5.7			

Table V.7

List of C^2S and χ^2_ν values of single ℓ-transfer fits for each peak listed in Tables V.5 and V.6.

E_x(MeV) ℓ→	2 C^2S	2 χ^2_ν	3 C^2S	3 χ^2_ν	4 C^2S	4 χ^2_ν	5 C^2S	5 χ^2_ν	6 C^2S	6 χ^2_ν	Final Nucleus
0.05	0.31	(4.2)			0.23	(44.)	0.06	(59.)			^{145}Eu
0.37	0.29	(63.)			0.24	(1.8)	0.06	(8.5)			
0.73	3.61	(168.)			2.86	(34.)	0.70	(6.9)			
1.04	0.63	(4.0)			0.40	(40.)	0.10	(51.)			
0.11	0.53	(53.)			0.43	(43.)	0.11	(69.)			^{149}Eu
0.51	2.81	(101.)			2.34	(43.)	0.58	(43.)			
1.07	0.48	(101.)			0.38	(24.)	0.10	(20.)			
1.47	1.07	(75.)			0.79	(27.)	0.19	(31.)			
1.74	0.57	(94.)			0.42	(27.)	0.10	(27.)			
0.33	0.70	(101.)	0.24	(108.)	0.69	(108.)	0.18	(115.)	0.13	(183.)	^{153}Eu
0.70	0.59	(43.)	0.20	(48.)	0.55	(53.)	0.14	(69.)	0.10	(115.)	
1.24	0.67	(75.)	0.23	(63.)	0.60	(63.)	0.15	(69.)	0.11	(115.)	
0.45	0.91	(87.)	0.32	(53.)	0.94	(24.)	0.25	(31.)	0.20	(81.)	^{155}Eu
1.07	0.72	(81.)	0.24	(58.)	0.69	(24.)	0.18	(27.)	0.14	(58.)	
1.41	1.08	(87.)	0.37	(31.)	0.99	(31.)	0.25	(43.)	0.20	(94.)	

strengths only slightly lower than those previously measured. The fact that the 0.73-MeV state has $\ell=5$ and a C^2S value not far from unity means that it exhausts most of the $1h_{11/2}$ strength. It appears as the largest peak in the spectrum (Figure V.7). On the whole, the present work gives C^2S values somewhat lower than previously reported. We have already seen this feature in connection with the low-lying states in ^{209}Pb and ^{209}Bi, where possible reasons for the tendency were given.

b) Low-lying peaks in ^{149}Eu

Five peaks in the ^{149}Eu spectrum at the positions indicated by the arrows in Figure V.7 were analyzed. These peaks correspond to unresolved clusters of low-lying states. Their angular distributions were fitted by a mixture of $\ell=2$, 4 and 5 DWBA angular distributions since, as we have seen, these are the only ℓ-transfers likely to occur for the low-lying states of ^{149}Eu. Angular distributions for four of the peaks are shown in Figure V.8. The C^2S values obtained using the "minimum χ^2_ν" criterion are given in Table V.5. Table V.7 lists the C^2S values obtained when the angular distributions were fitted with single ℓ-transfers from the allowed set.

We note from Table V.5 that the best-fit χ^2_ν values are large compared to unity; they range from about 16 to 36. The probable reason for this is that the peaks are very poorly resolved, making it difficult to extract accurate cross sections. Probably because of this, the $\ell=4$ C^2S value for the ground state is considerably larger than that found in other work. There is a large $\ell=5$ ($1h_{11/2}$) contribution to the peak at $E_x= 0.51$ MeV, which is the largest peak in the spectrum. The table shows that the $\ell=5$ ($1h_{11/2}$) proton excitation in ^{149}Eu is fragmented, its strength being spread over at least three of the low-lying peaks. Once again we note that the present strength values are generally lower than those previously reported.

As another test of our procedure for determining ℓ values, the allowed set of ℓ-transfers ($\ell=2$, 4, 5) was enlarged to include $\ell=3$ and 6 as well, and the angular distribution for the state at $E_x= 1.74$ MeV was fitted using ℓ-transfers from the larger set. The minimum-χ^2_ν procedure then selected ℓ-transfers of 3 and 6 instead of 2 and 5. This test reinforces the conclusion already arrived at in our analysis of the low-lying states of ^{209}Bi, that the fitting procedure is reliable in selecting ℓ values only to within ±1.

c) Low-lying peaks in ^{153}Eu

Three peaks were analyzed, as indicated by the arrows in Figure V.7. No strength values are available from previous studies for any state in ^{153}Eu. As we have seen, the Nilsson model prediction is that only ℓ-transfers of 2, 3, 4, 5 and 6 are allowed for the low-lying states of ^{153}Eu. This set of ℓ-transfers was used to fit the angular distributions for the three peaks. The fits using the "minimum χ^2_ν" criterion are displayed in Figure V.8. The corresponding C^2S values, reported here for the first time, are listed in Table V.5. Table V.7 lists the C^2S values obtained when single ℓ-transfer fits were made.

Note that the χ^2_ν values are very large for the best fits (Table V.5). The peak at E_x= 0.33 is not fitted well by any mixture of ℓ-values. As seen in Figure V.8, the angular distribution in the neighborhood of 9° is especially poorly fitted for this peak and, in fact, it is the deviation between experimental calculation and the theoretical calculation at 9° which makes the most significant contribution to the overall χ^2_ν. The other two peaks are better fitted with a mixture of ℓ values. They show some ℓ=3 strength, which supports the Nilsson model prediction that neighboring subshells of the spherical shell model mix at low excitation energy as the deformation increases. The Nilsson model predicts the ℓ=6 orbit to be lower in energy than the ℓ=3 orbit, but we find no ℓ=6 strength.

d) Low-lying peaks in ^{155}Eu

Three peaks were analyzed and the regions are pointed out in Figure V.7. No strength values have been previously reported for any of the states in ^{155}Eu. The Nilsson model shows that ℓ-transfers of 2, 3, 4, 5 and 6 are possible in the region of the low-lying states of ^{155}Eu. This set of ℓ-transfers was used to fit the low-lying peaks, using the "minimum χ_{ν}^{2}" criterion. The resulting fits to the angular distributions are shown in Figure V.8. The corresponding C^2S values, reported here for the first time, are listed in Table V.5. Table V.7 displays C^2S values obtained by single ℓ-transfer fits.

Note that the χ_{ν}^{2} values are large. Note also that a mixture of three ℓ-transfers was selected for the peaks at E_x= 0.45 and 1.07 MeV. Examination of Table V.7 shows that no single-ℓ fit to any of the low-lying peaks is very good. However, mixtures of ℓ values give much better fits (Table V.5 and Figure V.8). As in the case of ^{153}Eu, we find ℓ=3 strength (in agreement with the Nilsson model prediction) but no ℓ=6 strength (in disagreement with the Nilsson model prediction that the $i_{13/2}$ (ℓ=6) orbit is lower in energy than the $2f_{7/2}$ (ℓ=3) orbit).

V.5.2 High-Lying Proton Strength in ^{145,149,153,155}Eu

High-lying spectra from the (α,t) reactions are displayed in Figure V.6a. Angular distributions, obtained by "slicing" the spectra from about 2 MeV to about 15 MeV excitation energy in 520-keV wide bins, were fitted by mixtures of DWBA angular distributions corresponding to different ℓ-transfers. An examination of the expected single particle levels in the Nilsson model [Bo75a] shows the allowed set of ℓ-transfers to be 3, 5 and 6 for ^{145,149}Eu and 2, 3, 5 and 6 for ^{153,155}Eu. (In our analysis we extracted no $\ell=2$ strength, probably because cross sections for $\ell=2$ are much smaller than for the other ℓ values, as shown by Figure III.2.)

A number of different bin widths for the "slices" were tested to see whether the resulting strength distribution depended on the bin width. Bin widths of 280 keV, 520 keV, 1 MeV and 2 MeV were used. The general characteristics of the resulting strength distributions were similar. The decision to select the 520 keV bin width was arbitrary. A width of 280 keV would have been roughly equal to the experimental resolution and thus seemed too small, whereas a width of 2 MeV might have resulted in averaging of states. A width of 520 keV thus appeared to be a good compromise.

Table V.8 lists the complete range of χ^2_ν values for the high-lying region at E_x= 7.18 MeV in ^{153}Eu. Some of the fits give χ^2_ν values which differ only slightly from the minimum χ^2_ν value. Therefore, combinations of ℓ-values other than the particular mixture selected by the minimum-χ^2_ν fit are quite possible in this region. The minimum-χ^2_ν requirement may not be the best criterion to use for deducing C^2S values in high-lying regions. However, since no other criterion was used in this Thesis, the minimum-χ^2_ν

Table V.8

List of the possible C^2S values, with the ℓ-mixture indicated, for the high-lying region at E_x= 7.18 MeV in ^{153}Eu.

ℓ	C^2S	χ^2_ν	ℓ	C^2S	χ^2_ν	ℓ	C^2S	χ^2_ν
6	0.03	3.6	5	0.25	5.5	3	0.25	7.2
3	0.16		2	0.10		2	0.18	
5	0.16	4.0	6	0.002	5.7	6	0.05	8.5
3	0.04		5	0.26		2	0.31	
6	0.02	4.0	6	0.001	6.1	6	0.07	8.7
5	0.04		5	0.25				
3	0.14		2	0.10				
5	0.27	5.2	3	0.29	6.9	2	1.19	15.

results will be displayed for the sake of completeness, along with the fits obtained using single ℓ-transfers.

Examples of calculations using the "minimum χ^2_ν" criterion in different regions of the background-subtracted spectra are shown in Figure V.9. The excitation energies labeled are those at the center of the energy bin "slice", e.g., the energy bin for the 7.30 MeV region in ^{145}Eu is the interval from 7.04 MeV to 7.56 MeV. Note that in some cases the program picked out only one ℓ-transfer. In the case of ^{153}Eu, the angular distributions for the high-lying regions in the neighborhood of 9° are poorly fitted, just as for the low-lying peaks. Therefore the maximum contribution to χ^2_ν comes from the 9° point.

Figure V.10 displays the angular distribution of the under-lying background for typical high-lying regions in the spectra of the four Eu isotopes. Generally, with a few exceptions, the angular distributions for the background have similar shapes. At the larger angles we observe the effect of including the angle-independent evaporation process. We note that, at E_x= 7.18 MeV in ^{153,155}Eu, the shape of the background is different from that in ^{145,149}Eu at nearly the same E_x. This shape difference is primarily due to the low ground-state Q-value in the ^{152,154}Sm$(\alpha,t)^{153,155}$Eu reactions ($Q_{g.s.}$= -13.9 and -13.2 MeV, respectively) compared to the ^{144,148}Sm$(\alpha,t)^{145,149}$Eu reactions ($Q_{g.s.}$= -16.6 and -15.4 MeV, respectively) where

Figure V.9

Angular distributions of some high-lying regions in ^{145,149,153,155}Eu after background subtraction. Each region is 520-keV wide, centered at the excitation energy E_x(in MeV) indicated. The curves are the minimum-χ^2_ν fits using the DWBA angular distributions. The ℓ values thus determined are indicated.

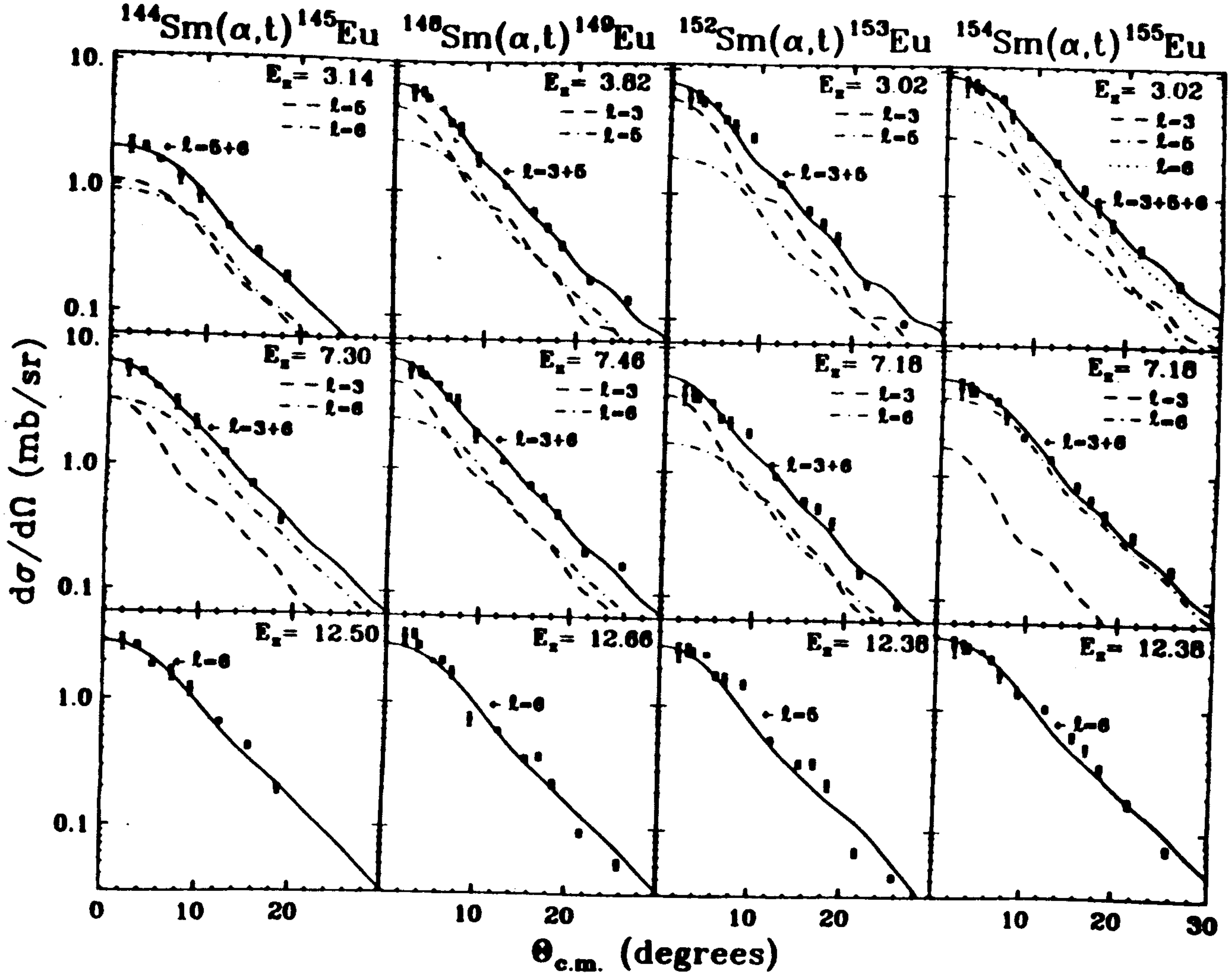

^{144}Sm(α,t)^{145}Eu
^{148}Sm(α,t)^{149}Eu
^{152}Sm(α,t)^{153}Eu
^{154}Sm(α,t)^{155}Eu
E$_x$= 3.14
ℓ=5
ℓ=6
← ℓ=5+6
E$_x$= 3.62
ℓ=3
ℓ=5
← ℓ=3+5
E$_x$= 3.02
ℓ=3
ℓ=5
← ℓ=3+5
E$_x$= 3.02
ℓ=3
ℓ=5
ℓ=6
← ℓ=3+5+6
E$_x$= 7.30
ℓ=3
ℓ=6
← ℓ=3+6
E$_x$= 7.46
ℓ=3
ℓ=6
← ℓ=3+6
E$_x$= 7.18
ℓ=3
ℓ=6
← ℓ=3+6
E$_x$= 7.18
ℓ=3
ℓ=6
← ℓ=3+6
E$_x$= 12.50
← ℓ=6
E$_x$= 12.66
← ℓ=6
E$_x$= 12.38
← ℓ=5
E$_x$= 12.38
← ℓ=6
10.
1.0
0.1
10.
1.0
0.1
1.0
0.1
0
10
20
10
20
10
20
10
20
30
dσ/dΩ (mb/sr)
θ$_{c.m.}$ (degrees)

Figure V.9

Figure V.10

Angular distributions of the under-lying background for typical high-lying regions in the $^{144,148,152,154}\mathrm{Sm}(\alpha,t)^{145,149,153,155}\mathrm{Eu}$ reactions. The term "scale × 0.1" in some of the panels means that the indicated scale must be multiplied by 0.1 to get the actual scale.

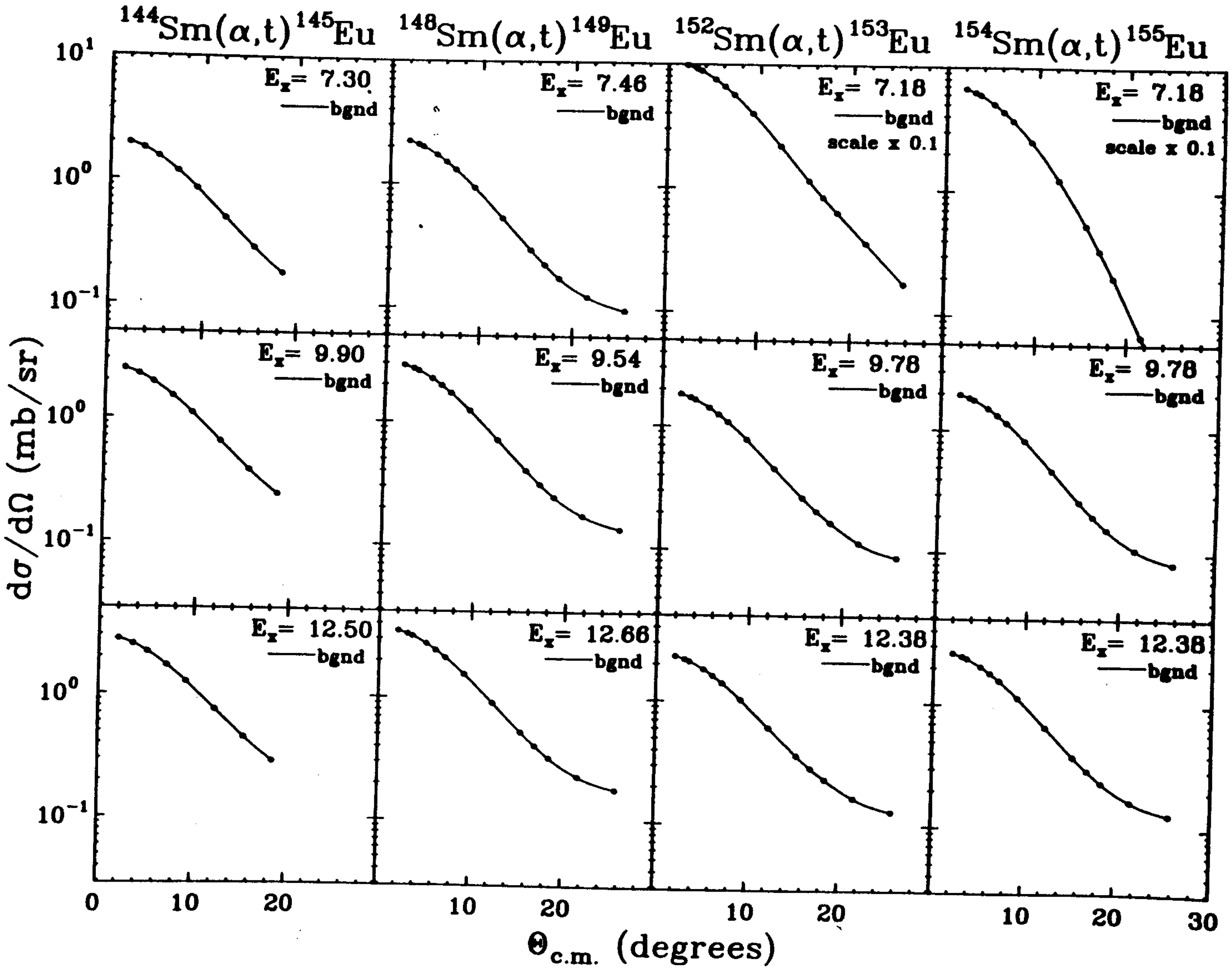^{144}Sm(α,t)^{145}Eu
^{148}Sm(α,t)^{149}Eu
^{152}Sm(α,t)^{153}Eu
^{154}Sm(α,t)^{155}Eu
E$_x$= 7.30
E$_x$= 7.46
E$_x$= 7.18
E$_x$= 7.18
E$_x$= 9.90
E$_x$= 9.54
E$_x$= 9.78
E$_x$= 9.78
E$_x$= 12.50
E$_x$= 12.66
E$_x$= 12.38
E$_x$= 12.38
bgnd
scale x 0.1
10^1
10^0
10^{-1}
dσ/dΩ (mb/sr)
0
10
20
30
Θ$_{c.m.}$ (degrees)

Figure V.10

the background is low and the angle-independent process does not have an effect.

Not all the fits for every region and for every target are displayed, since each reaction has about 25 "sliced" angular distributions. Instead, a 3-dimensional plot of the "sliced" experimental data of $d\sigma/d\Omega$ versus $\Theta_{c.m.}$ versus excitation energy in MeV is shown in Figure V.11. $d\sigma/d\Omega$ is plotted along the z-axis, $\Theta_{c.m.}$ along the y-axis and the excitation energy along the x-axis. The scales for all three axes are linear. The conventional experimental angular distribution at any excitation energy is the projection onto the y-z plane. The range of excitation energies is plotted on the x-axis and listed in Table V.8.

High-lying proton strength distributions in the europium isotopes are displayed as a function of excitation energy in Figures V.12 and V.13. In Figure V.12, the C^2S values are those obtained by performing minimum-χ^2_ν fits to the experimental angular distributions with a mixture of allowed ℓ-transfers (ℓ=3, 5 and 6); Figure V.14 displays the corresponding χ^2_ν as a function of excitation energy. In Figure V.13, the C^2S values are those obtained by fitting the experimental angular distributions with a single ℓ-transfer from the allowed set; Figure V.15 displays the corresponding χ^2_ν as a function of excitation energy. Note in Figure V.15 that the χ^2_ν distributions for the ℓ=5 and ℓ=6 transfers appear very similar. This meant that it was difficult to distinguish between the adjacent ℓ values of 5

Figure V.11

A 3-dimensional plot ($d\sigma/d\Omega$ vs $\Theta_{c.m.}$ vs Excitation energy) of experimental angular distributions for the $^{144,148,152,154}Sm(\alpha,t)^{145,149,153,155}Eu$ reactions. $\Theta_{c.m.}$ varies from 0° to 30° in all four panels of the figure.

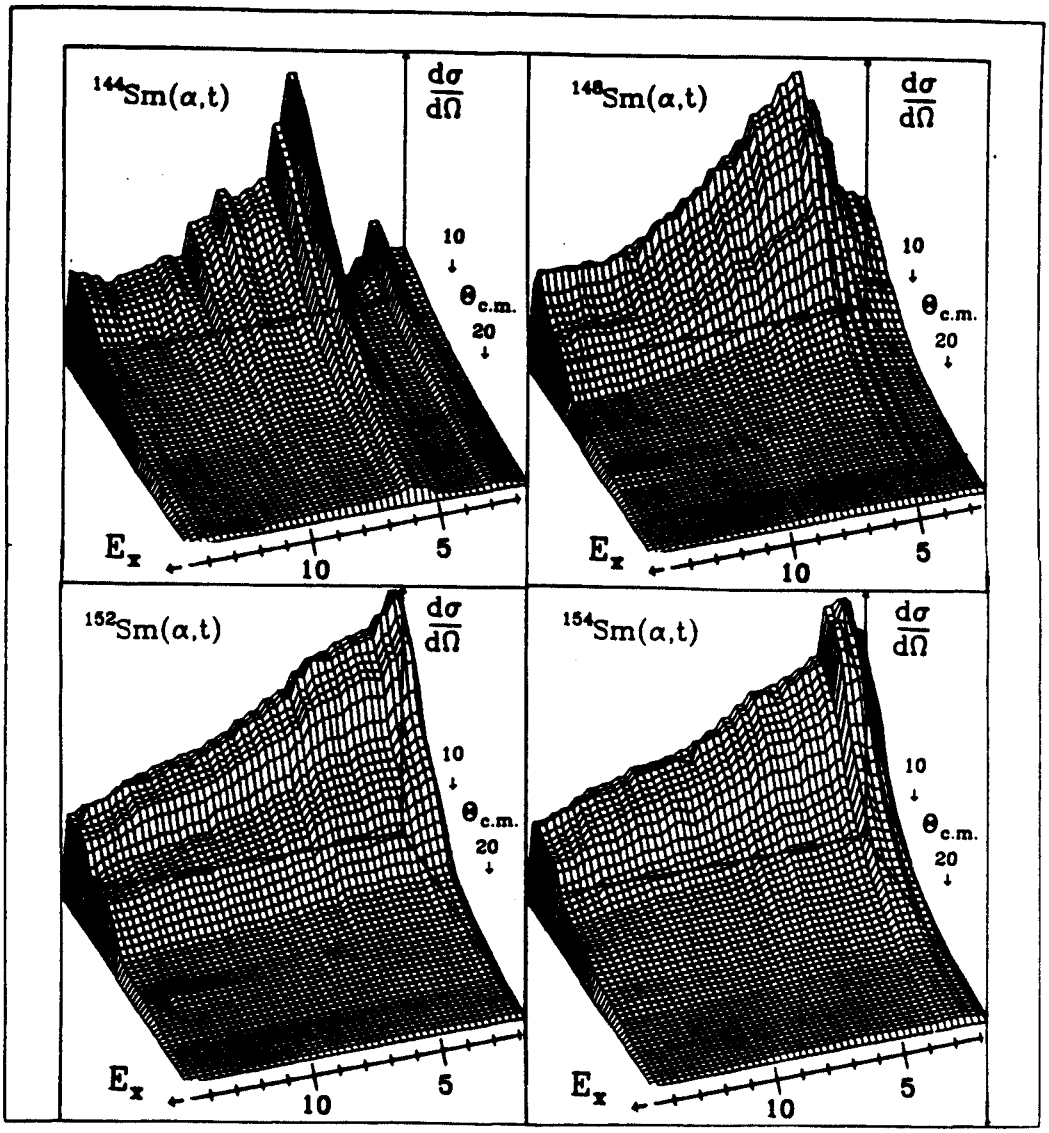

^{144}Sm(α,t)
$\frac{d\sigma}{d\Omega}$
10
$\theta_{c.m.}$
20
E_x
10
5
^{148}Sm(α,t)
$\frac{d\sigma}{d\Omega}$
10
$\theta_{c.m.}$
20
E_x
10
5
^{152}Sm(α,t)
$\frac{d\sigma}{d\Omega}$
10
$\theta_{c.m.}$
20
E_x
10
5
^{154}Sm(α,t)
$\frac{d\sigma}{d\Omega}$
10
$\theta_{c.m.}$
20
E_x
10
5

Figure V.11

Figure V.12

Spectroscopic strength distribution of the fragmented $\ell=3$, 5 and 6 proton single-particle excitations in ^{145,149,153,155}Eu obtained by performing minimum-χ^2_ν fits to angular distributions measured in (α,t) reactions on ^{144,148,152,154}Sm targets. $\ell=3$ corresponds to the $2f_{7/2}$ and $2f_{5/2}$ single-particle states, $\ell=5$ to $1h_{9/2}$ and $\ell=6$ to $1i_{13/2}$. The term "scale × 2" in some of the panels means that the indicated scale must be multiplied by two to get the actual scale.

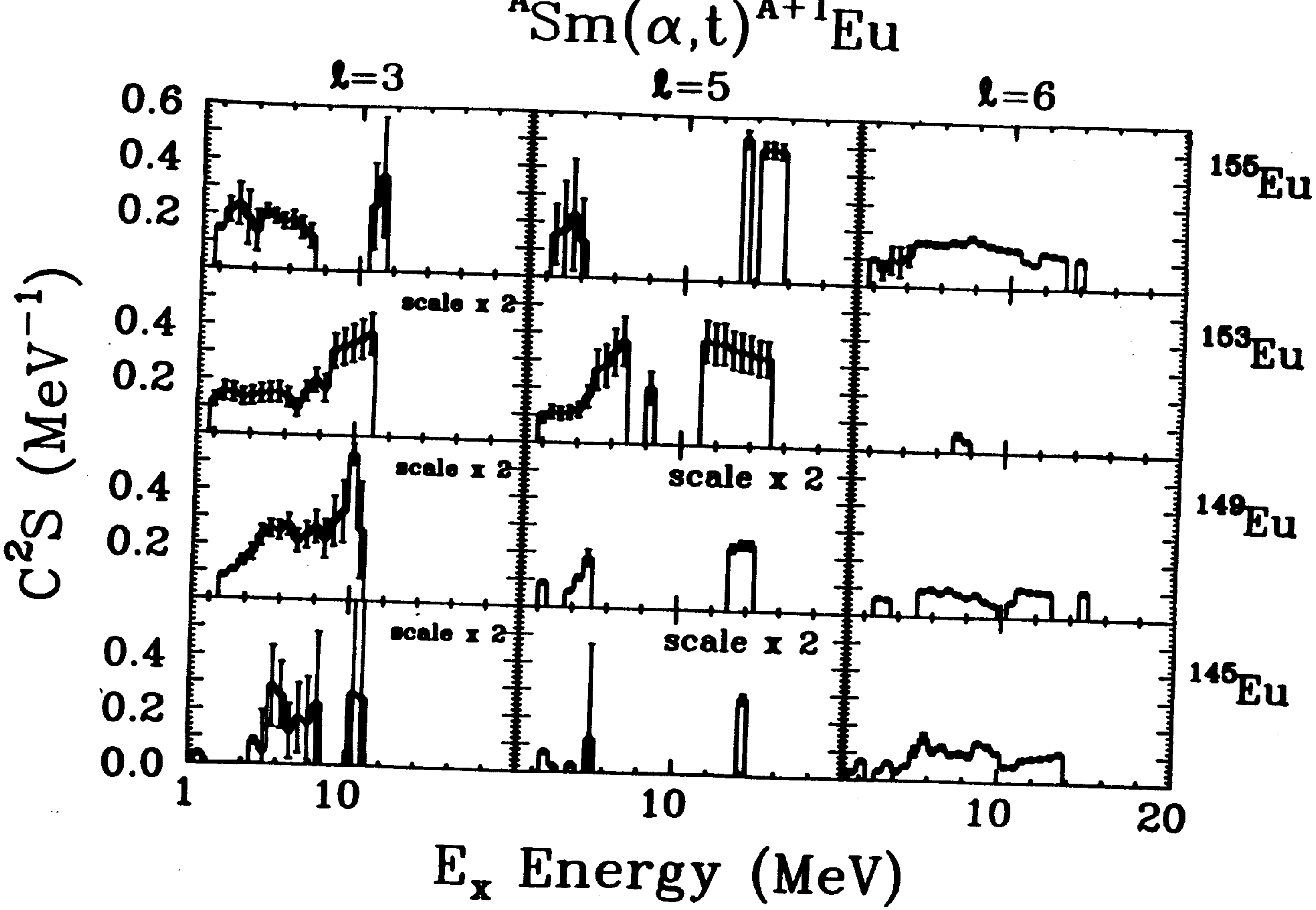
$^{A}Sm(\alpha,t)^{A+1}Eu$
ℓ=3
ℓ=5
ℓ=6
C^2S (MeV^{-1})
0.6
0.4
0.2
0.0
scale x 2
^{155}Eu
^{153}Eu
^{149}Eu
^{145}Eu
1
10
20
E_x Energy (MeV)

Figure V.12

Figure V.13

As for Figure V.12, except that the strength distributions were obtained by fitting the measured angular distributions with single ℓ-transfers (ℓ=3, 5 and 6). The terms "scale × 2", "scale × 3" and "scale × 4" in some of the panels mean that the indicated scales must be multiplied by two, three and four, respectively, to get the actual scales.

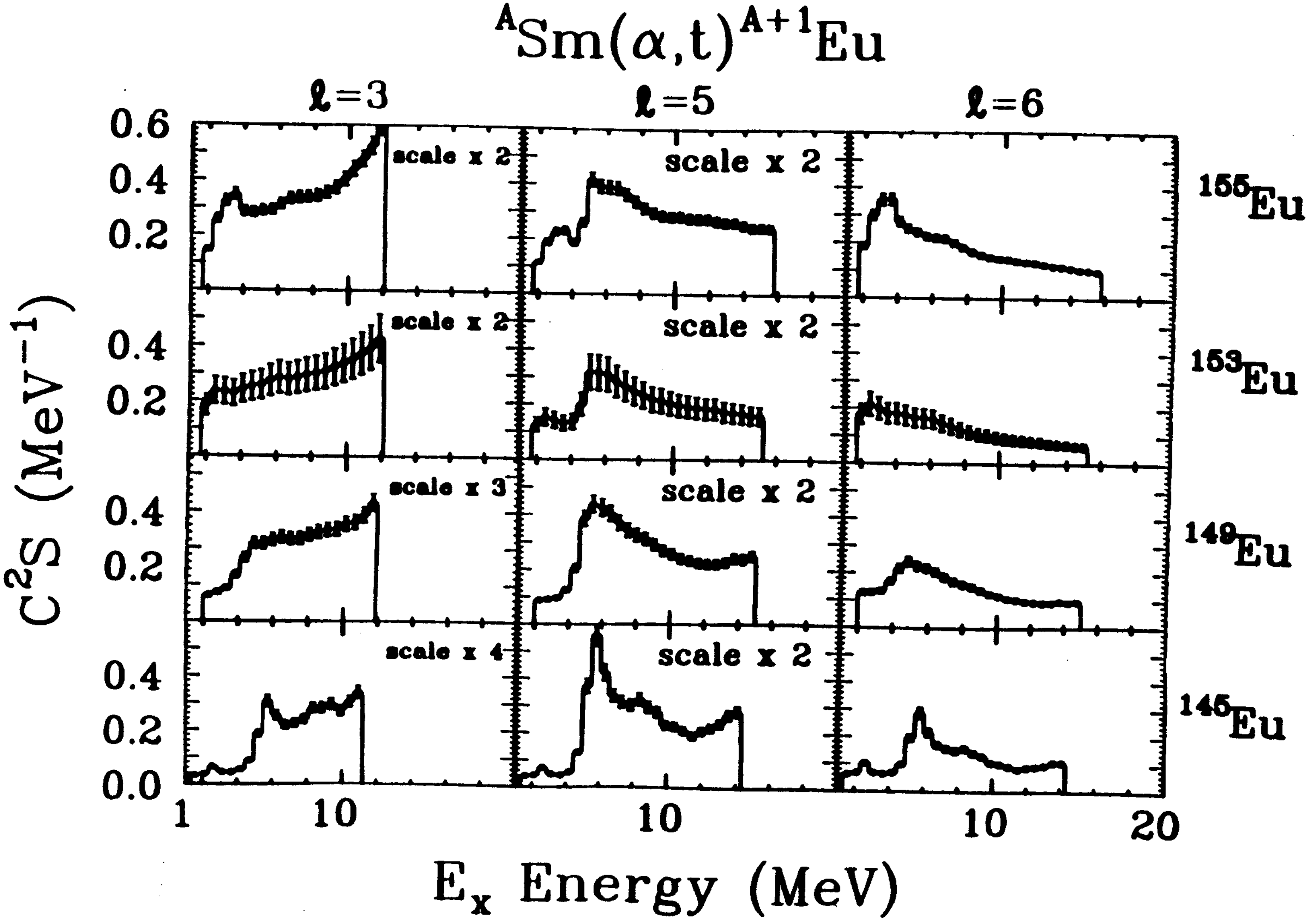
$^{A}Sm(\alpha,t)^{A+1}Eu$
ℓ=3
ℓ=5
ℓ=6
C^2S (MeV^{-1})
0.6
0.4
0.2
0.0
scale x 2
scale x 2
scale x 3
scale x 4
scale x 2
scale x 2
scale x 2
scale x 2
^{155}Eu
^{153}Eu
^{149}Eu
^{145}Eu
1
10
10
10
20
E_x Energy (MeV)

Figure V.13

Figure V.14

The minimum-χ^2_ν distribution corresponding to the fit that produced the C^2S values in Figure V.12.

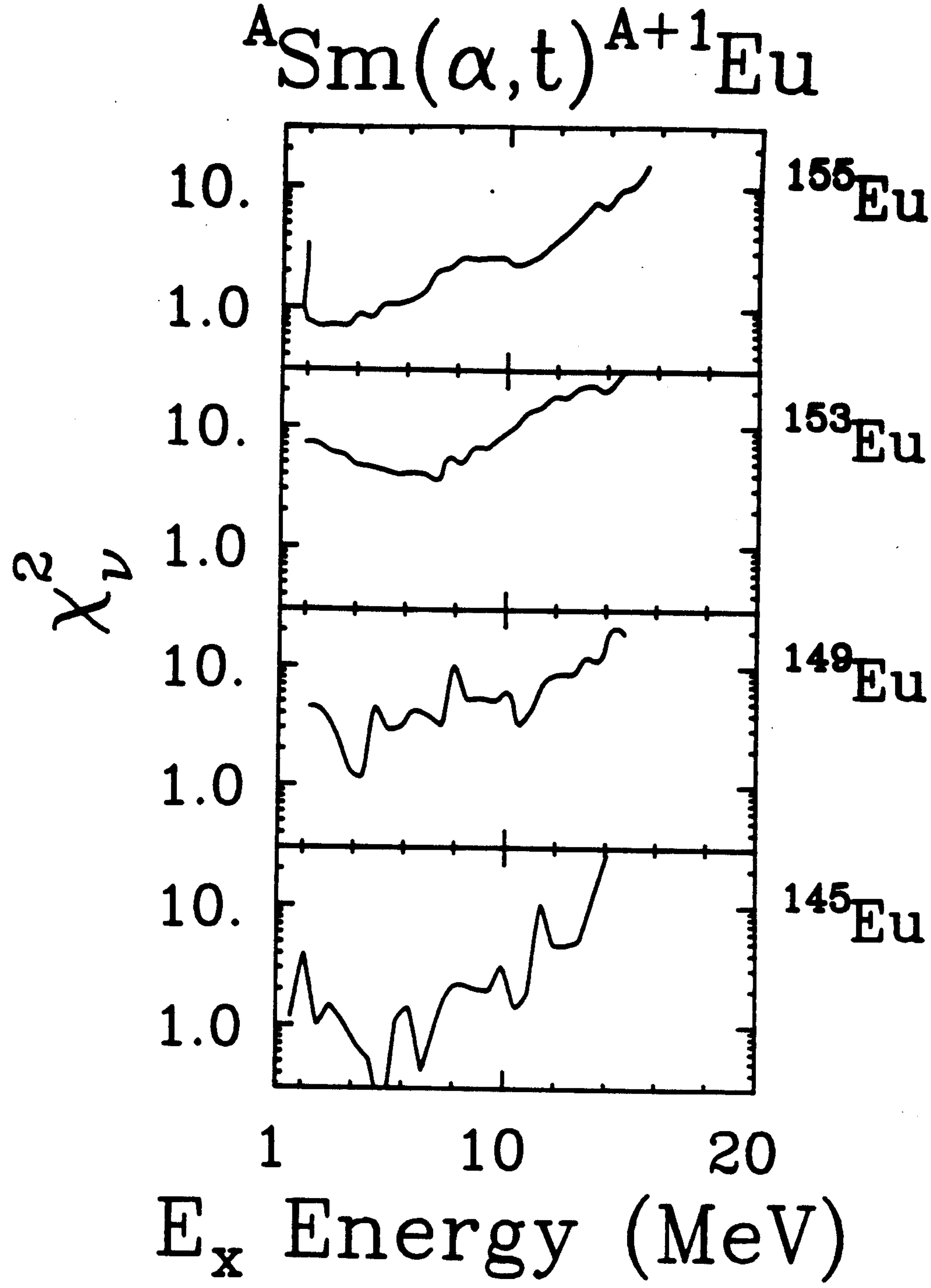

$^{A}Sm(\alpha,t)^{A+1}Eu$
^{155}Eu
^{153}Eu
^{149}Eu
^{145}Eu
10.
1.0
χ^2_ν
1
10
20
E_x Energy (MeV)

Figure V.14

Figure V.15

The χ_ν^2 distribution corresponding to the single-ℓ fits that produced the C²S values in Figure V.13.

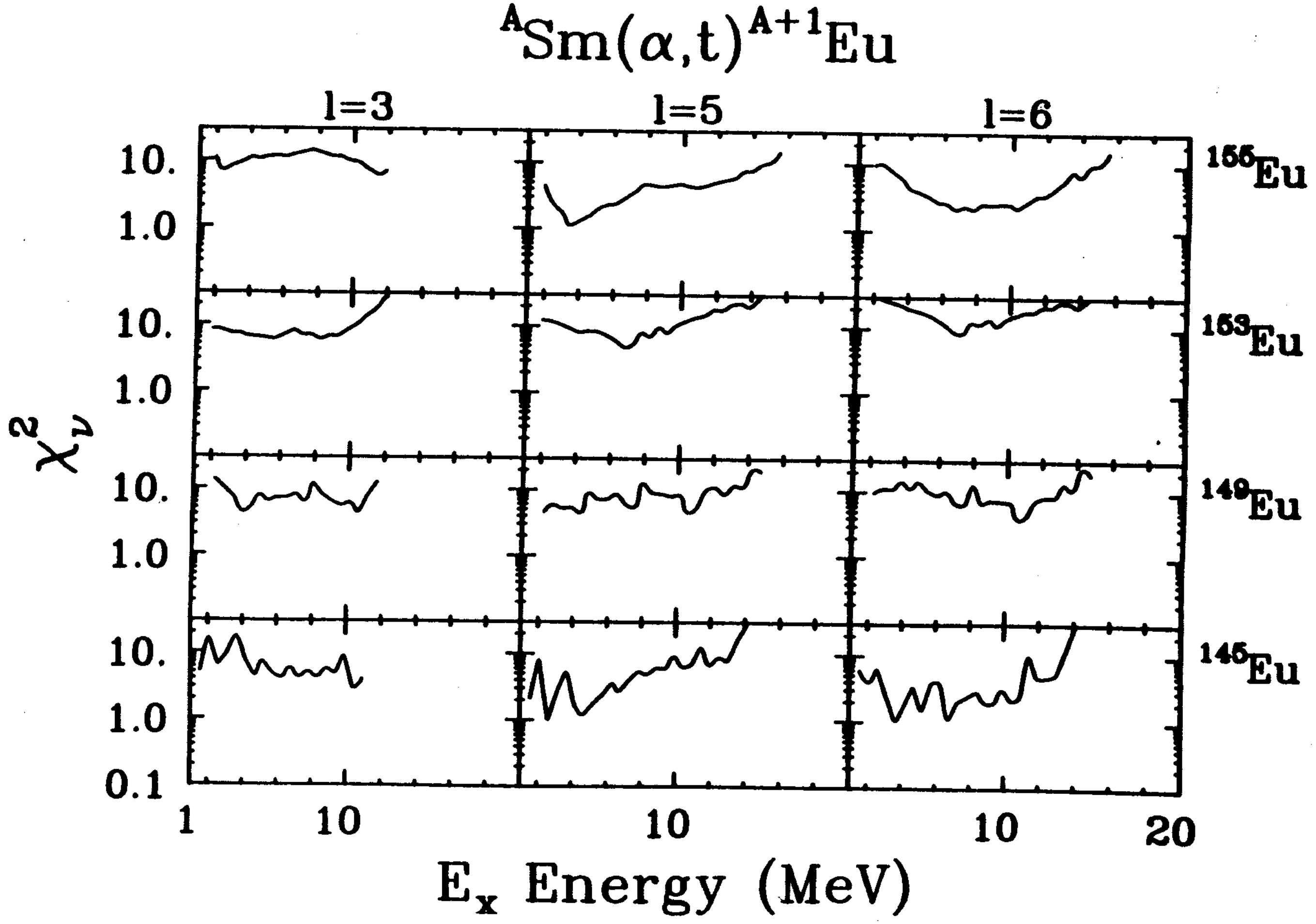
$^{A}Sm(\alpha,t)^{A+1}Eu$
l=3
l=5
l=6
^{155}Eu
^{153}Eu
^{149}Eu
^{145}Eu
χ^2_ν
10.
1.0
10.
1.0
10.
1.0
10.
1.0
0.1
1
10
10
10
20
E_x Energy (MeV)

Figure V.15

and 6. We also notice that it was not very difficult to distinguish between $\ell=3$ and 5 or between $\ell=3$ and 6 using the χ^2_ν distribution. Note also that the $\ell=3$ transfer does not have any C^2S or χ^2_ν values above $E_x = 12$ MeV. As mentioned in Chapter III, DWBA angular distributions for $\ell=3$ could not be calculated above 12 MeV excitation energy and thus a C^2S value for $\ell=3$ could not be determined in that region. Comparison of the plots of C^2S with plots of the respective spectra shows the regions of the spectrum in which the various ℓ-transfers dominate.

The sum rule limit of the spectroscopic strength for a given j-transfer in stripping reactions is unity, as expressed by equation (III.16). The predicted DWBA angular distributions shapes depend only on the ℓ transfer, not on the j-transfer. In particular, the predicted angular distribution shapes for the $2f_{7/2}$ and $2f_{5/2}$ transitions look very similar. (They are not identical because the bound state part of the potential contains an $\ell \cdot s$ term (see Table III.1 and equation III.17c) which has different values for the two transitions.) A given ℓ-value would correspond to either $j=\ell+1/2$ or to $j=\ell-1/2$. We must remember this ambiguity when summing the transition strengths.

A summing of the strength was carried out for each of the four Eu nuclei and is tabulated in Table V.9. Results from previous studies for ^{145}Eu [St83,Ga85a] are also given. The theoretical sum rule limit is 2 for $\ell=3$, since for this ℓ-transfer there are two possible associated j-transfers,

Table V.9

List of the summed transition strengths for the high-lying regions of ^{145,149,153,155}Eu from this experiment and from other work. The uncertainties in the summed strengths are given in parenthesis. They are calculated using the uncertainty in the fitted parameter and in the target thickness.

E_x(MeV) interval	ℓ	This experiment ΣC^2S	$n\ell j$	Other work ΣC^2S	Other work ΣC^2S	Final Nucleus
1.5 - 14.5	3	1.88(1.44)	$2f_{7/2}$	0.43[a]	0.86[b]	^{145}Eu
1.5 - 14.5	5	0.53(0.15)	$1h_{9/2}$	0.75	0.51	
1.5 - 14.5	6	1.03(0.01)	$1i_{13/2}$	0.54	0.88	
2 - 15	3	3.85(0.84)				^{149}Eu
2 - 15	5	1.14(0.10)				
2 - 15	6	0.70(0.01)				
1.5 - 15	2	0.0				^{153}Eu
1.5 - 15	3	3.62(0.80)				
1.5 - 15	5	2.48(0.55)				
1.5 - 15	6	0.05(0.01)				
1.5 - 15	2	0.0				^{155}Eu
1.5 - 15	3	1.27(0.44)				
1.5 - 15	5	1.33(0.37)				
1.5 - 15	6	1.53(0.17)				

a) [Ga85a]
b) [St83]

$2f_{7/2}$ and $2f_{5/2}$ [Bo75a]; for ℓ=2, 5 and 6, the limits are 1. In our analysis, these limits are exceeded to some extent for ℓ-transfers of 3, 5 and 6 in most cases, whereas for ℓ=2 no strength is found. These results show the limitations of the analysis. Some of the possible reasons for the discrepancy are: (i) not enough background may have been subtracted; (ii) the ℓ=5 and ℓ=6 strengths may need a slight redistribution; (iii) we may need to introduce another ℓ-transfer from another subshell; (iv) the reactions are not sensitive to ℓ=2 strength, since ℓ=2 cross sections are much weaker than those for higher ℓ's (about a factor of four weaker than ℓ=3 cross sections, see Figure III.2); (v) in view of the uncertainty of ±1 in ℓ determination, the ℓ=2 strength expected for ^{153,154}Eu in the excitation energy region considered (4 to 15 MeV) may have been misidentified as ℓ=3 by the "minimum χ^2_ν" procedure. This last possibility would account both for the lack of observed ℓ=2 strength for ^{153,155}Eu and, since the misidentification would effectively raise the ℓ=3 sum rule limit to about $2^1/_4$ (The $^1/_4$ is used because the ℓ=2 cross sections is about a factor four less than the ℓ=3 cross sections), for the observed ℓ=3 strength in the two nuclei.

V.6 ^{144,148,152,154}Sm(α,^{3}He)^{145,149,153,155}Sm REACTIONS

We shall discuss the results from the study of the (α,^{3}He) reactions on the samarium isotopes in two parts:

1) The results for the low-lying states, including the extraction of angular distributions, assignments of ℓ-transfer and determination of C^2S values.
2) The results for the high-lying part of the spectra, including angular distributions extracted using the "slicing" method described before and C^2S distributions obtained as a function of excitation energy.

V.6.1 Low-Lying States in ^{145,149,153,155}Sm

The low-lying parts of the energy spectra from the (α,^{3}He) reaction on ^{144,148,152,154}Sm are displayed in Figure V.16. Note that the states in ^{145}Sm are well resolved up to an excitation energy of about 2.5 MeV. As the mass, and thus the deformation, of the isotope increases, the density of the low-lying levels also increases and so the levels are not well separated due to limitations of our experimental resolution. The angular distributions obtained for these unresolved states are shown in Figure V.17. The DWBA program should pick out the correct mixture of ℓ-transfers for the states within a peak. If the decomposition works well for the low-lying states, we can be more confident about applying the method to the higher lying regions of the spectra.

The N (neutron number) values of the samarium isotopes ^{145,149,153,155}Sm are 83, 87,91 and 93, respectively. In simple shell model theory the $1h_{11/2}$ level is filled at

Figure V.16

Spectra of ^{3}He at 5° showing the low-lying neutron states populated by the ^{144,148,152,154}Sm(α,^{3}He)^{145,149,153,155}Sm stripping reactions. Besides the Q-values energy scale along the horizontal axis, excitation energy scales (in MeV) are also shown in each panel of the figure.

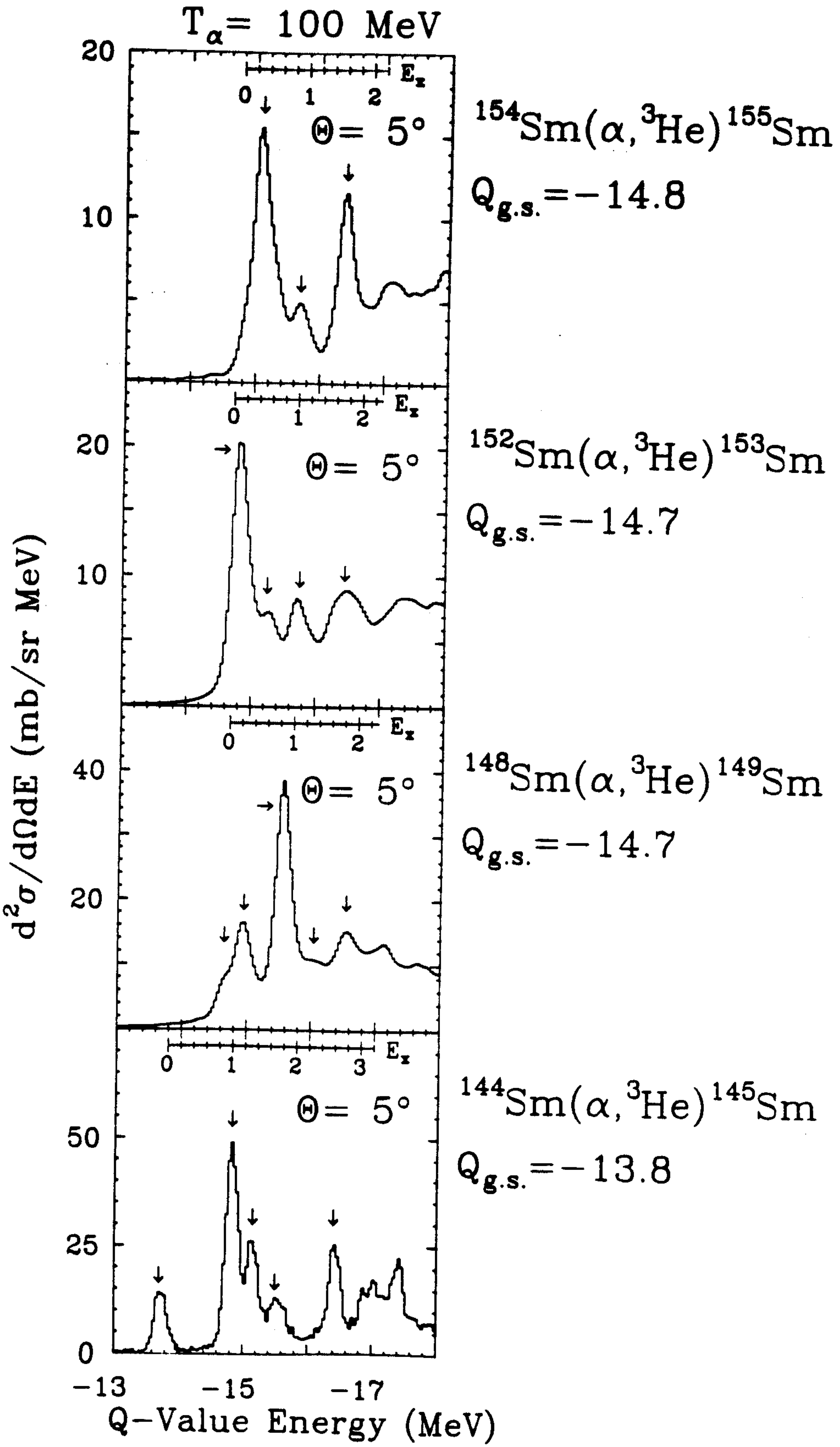
Tα= 100 MeV
d²σ/dΩdE (mb/sr MeV)
Q−Value Energy (MeV)
−13
−15
−17
E_x
Θ= 5°
154Sm(α,3He)155Sm
Qg.s.=−14.8
20
10
0
1
2
152Sm(α,3He)153Sm
Qg.s.=−14.7
20
10
148Sm(α,3He)149Sm
Qg.s.=−14.7
40
20
144Sm(α,3He)145Sm
Qg.s.=−13.8
50
25
0
3

Figure V.16

Figure V.17

Angular distributions of some low-lying peaks (indicated with arrows in Figure V.16) which are excited in ^{145,149,153,155}Sm. The curves are minimum-χ^2_ν fits with the DWBA predictions; the corresponding ℓ values are indicated.

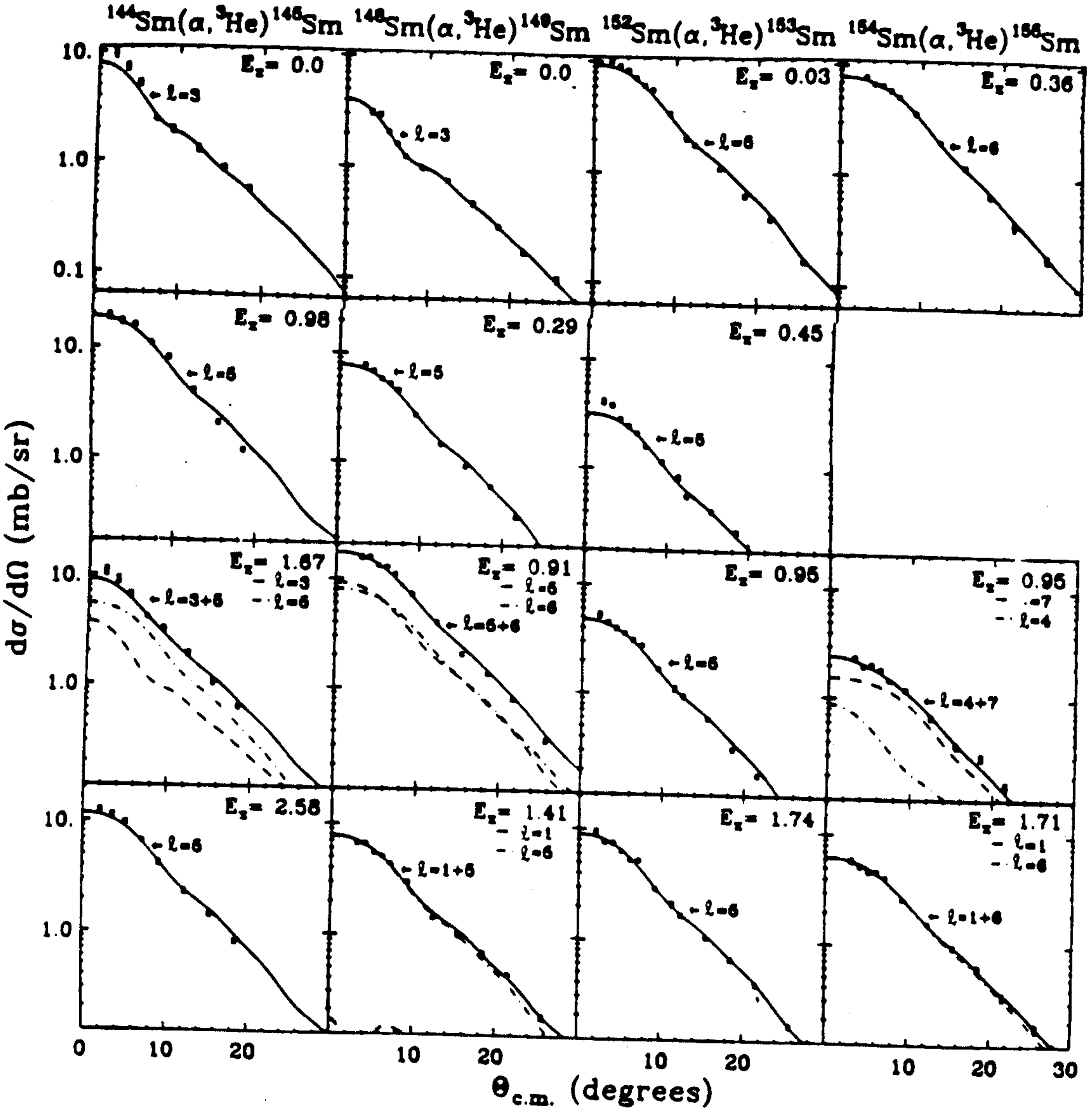

^{144}Sm(α,^{3}He)^{145}Sm
^{148}Sm(α,^{3}He)^{149}Sm
^{152}Sm(α,^{3}He)^{153}Sm
^{154}Sm(α,^{3}He)^{155}Sm
E_x= 0.0
← ℓ=3
E_x= 0.0
← ℓ=3
E_x= 0.03
← ℓ=6
E_x= 0.36
← ℓ=6
E_x= 0.98
← ℓ=6
E_x= 0.29
← ℓ=5
E_x= 0.45
← ℓ=5
E_x= 1.67
ℓ=3
ℓ=6
← ℓ=3+6
E_x= 0.91
ℓ=5
ℓ=6
← ℓ=5+6
E_x= 0.95
← ℓ=6
E_x= 0.95
=7
ℓ=4
← ℓ=4+7
E_x= 2.58
← ℓ=6
E_x= 1.41
ℓ=1
ℓ=6
← ℓ=1+6
E_x= 1.74
← ℓ=6
E_x= 1.71
ℓ=1
ℓ=6
← ℓ=1+6
10.
1.0
0.1
dσ/dΩ (mb/sr)
0
10
20
30
$\theta_{c.m.}$ (degrees)

Figure V.17

N=82, and the valence neutrons in the Sm nuclei (ranging in number from 1 to 11) are distributed in the next subshell (between N=82 and N=126). This subshell contains the orbits $2f_{7/2}$, $1h_{9/2}$, $1i_{13/2}$, $3p_{3/2}$, $2f_{5/2}$ and $3p_{1/2}$ [Bo75a]. As was the case for the proton orbits, the Nilsson model shows that the neutron orbits also shift in energy depending upon the deformation. As the deformation increases, the $2g_{9/2}$ and $1j_{15/2}$ orbits from the next higher subshell (above N=126) occur in the same energy region as the orbits listed above. Therefore, the ℓ-transfers expected for the low-lying states of ^{145,149}Sm are 1, 3, 5 and 6, while for ^{153,155}Sm, the expected ℓ-transfers are 1, 3, 4, 5, 6 and 7.

Results for the low-lying states will be presented individually for the four Sm isotopes. As mentioned earlier, the ability to select an ℓ-transfer (and thus to determine the C^2S value) by the "minimum χ^2_ν" criterion, when other ℓ-transfers are also involved, is probably reliable to within ±1.

In addition to allowing the set of ℓ-transfers mentioned above to fit each of the low-lying peaks, each peak was also fitted separately by each of the single ℓ-transfers from that set. This allows the reader to better evaluate the reliability of the ℓ-transfer values obtained from the fit and to have available the C^2S values if a different ℓ-mixture is assumed.

a) Low-lying states in ^{145}Sm

Since the low-lying states of ^{145}Sm were well resolved in the present experiment, the angular distributions measured for them provided a means for checking the angular distributions predicted by the code DWUCK4 for different ℓ-transfers. In addition, the spectroscopic strengths obtained were compared with previous measurements [Bo75b].

The five states that were analyzed are indicated by arrows in Figure V.15. The allowed set of ℓ-transfers (ℓ=1, 3, 5 and 6) was used to fit the angular distributions for the low-lying states. The fits are shown in Figure V.17. The C^2S values extracted using the minimum χ^2_ν method are shown in Table V.10. Table V.11 lists the C^2S values obtained when single ℓ-transfer fits were made. The χ^2_ν value for each fit is shown in parenthesis.

As shown in Table V.10, the ℓ-value for the ground state is correctly identified but the strength is less than half the value determined in earlier work. The peak at 0.98 MeV is identified as having ℓ=5; it probably corresponds to the known state at 1.099 MeV, which has ℓ=6. (Recall the ±1 uncertainty in ℓ determination.) The 0.98-MeV peak is the largest one in the ^{145}Sm spectrum, consistent with the fact that the (α,^{3}He) reaction at 100 MeV favors high-ℓ transfers; this is due to the angular momentum matching condition (III.5). It is for the same reason that the known $3p_{3/2}$ level at 0.89 MeV does not appear to be excited in the

Table V.10

List of the spectroscopic strengths (C^2S) obtained from minimum-χ^2_ν fits for the low-lying states of ^{145,149,153,155}Sm. The χ^2_ν values of the fits are given in parenthesis.

Pk #	E_x(MeV)	This experiment ℓ	C^2S(exp) (χ^2_ν)	Nuclear Data Sheets E_x(MeV)	$n\ell j$	Other work C^2S	Final Nucleus
1	0.00	3	0.38 (5.4)	0.0	$2f_{7/2}$	0.85[a]	
2	0.98	5	0.88 (12.)	0.894	$3p_{3/2}$	0.53	
				1.099	$1i_{13/2}$	0.46	
3	1.28	5	0.53 (4.3)	1.43	$1h_{9/2}$	0.64	^{145}Sm
4	1.67	5	0.26 (4.5)	1.620	$3p_{1/2}$	0.63	
		3	0.23	1.676	$2f_{5/2}$	0.21	
				2.350	($2f_{5/2,7/2}$)	0.04, 0.03	
				2.499	($2f_{5/2,7/2}$)	0.07, 0.05	
5	2.58	5	0.55 (2.9)	2.674	($3p_{1/2,3/2}$)	0.11, 0.05	
					$1i_{13/2}$	0.25	
1	0.00	3	0.25 (2.0)				
2	0.29	5	0.38 (5.8)				
3	0.91	6	0.13 (11.)				
		5	0.46				
4	1.41	5	0.38 (6.5)				^{149}Sm
		1	0.76				
5	1.89	6	0.11 (13.)				
		3	0.24				
1	0.03	5	0.48 (9.5)				
2	0.45	5	0.17 (9.1)				
3	0.95	5	0.25 (6.0)				^{153}Sm
4	1.74	5	0.48 (6.6)				
1	0.36	6	0.13 (1.1)				
2	0.95	7	0.02 (3.2)				^{155}Sm
		4	0.02				
3	1.71	6	0.10 (2.8)				
		1	0.61				

a) [Bo75b]

Table V.11

List of C^2S and χ^2_ν values of single ℓ-transfer fits for each low-lying peak from the $(\alpha,{}^3He)$ reactions on the samarium isotopes.

$\ell \rightarrow$	1		3		4		5		6		Final
E_x(MeV)	C^2S	χ^2_ν	C^2S	χ^2_ν	C^2S	χ^2_ν	C^2S	χ^2_ν	C^2S	χ^2_ν	Nucleus
											^{145}Sm
0.0	4.6	(72.)	0.38	(5.4)			0.23	(25.)	0.06	(31.)	
0.98	14.7	(343.)	0.15	(67.)			0.88	(12.)	0.23	(16.)	
1.28	10.5	(204.)	0.94	(28.)			0.52	(4.3)	0.14	(12.)	
1.67	8.0	(161.)	0.70	(14.)			0.37	(6.1)	0.10	(10.)	
2.58	11.3	(235.)	1.02	(44.)			0.55	(2.9)	0.14	(8.5)	
											^{149}Sm
0.0	2.9	(204.)	0.25	(2.0)			0.13	(48.)	0.35	(53.)	
0.29	5.8	(656.)	0.66	(109.)			0.38	(5.8)	0.10	(20.)	
0.91	15.2	(810.)	1.73	(168.)			0.94	(12.)	0.24	(12.)	
1.41	9.0	(608.)	0.87	(102.)			0.41	(8.6)	0.10	(10.)	
1.89	13.5	(608.)	1.23	(109.)			0.52	(23.)	0.13	(17.)	

$\ell \rightarrow$	1		3		4		5		6		7		
E_x(MeV)	C^2S	χ^2_ν	C^2S	χ^2_ν	C^2S	χ^2_ν	C^2S	χ^2_ν	C^2S	χ^2_ν	C^2S	χ^2_ν	
													^{153}Sm
0.03	6.1	(588.)	0.78	(115.)	0.23	(27.)	0.48	(9.5)	0.13	(24.)	0.10	(63.)	
0.45	2.4	(461.)	0.30	(69.)	0.08	(15.)	0.17	(9.1)	0.04	(20.)	0.03	(48.)	
0.95	3.7	(571.)	0.46	(123.)	0.13	(24.)	0.25	(6.0)	0.06	(15.)	0.05	(43.)	
1.74	8.8	(622.)	1.03	(147.)	0.28	(27.)	0.48	(6.6)	0.12	(9.9)	0.09	(35.)	
													^{155}Sm
0.36	10.6	(504.)	0.97	(73.)	0.25	(20.)	0.10	(6.1)	0.13	(1.1)	0.10	(12.)	
0.95	4.9	(270.)	0.35	(32.)	0.08	(20.)	0.03	(12.)	0.04	(5.3)	0.03	(4.8)	
1.71	12.5	(490.)	1.05	(84.)	0.25	(23.)	0.89	(10.)	0.10	(3.2)	0.08	(8.1)	

0.98-MeV peak. Indeed, when we tried to fit the angular distribution for this peak with a pure $\ell=1$ transfer, the attempt failed: the shape was wrong (Figure V.18) and the extracted C^2S value (14.7, as shown in Table V.11) was unphysically high. The peak at $E_x = 1.28$ MeV, if identified with the known $1h_{9/2}$ level at 1.43 MeV, agrees best with previous measurements. Note from Table V.10 that the sum of the C^2S values for $\ell=5$ determined in this work exceeds the sum rule limit of unity. This implies that some of the strength identified as $\ell=5$ is probably $\ell=6$ (for which the minimum-χ^2_ν fits did not find any strength).

b) Low-lying states in ^{149}Sm

Five low-lying peaks in the ^{149}Sm spectrum were analyzed as indicated by arrows in Figure V.16. They were taken to correspond to unresolved groups of individual states and their angular distributions were fitted by mixtures of ℓ-transfers from the allowed set ($\ell=1$, 3, 5 and 6). The fits using the minimum-χ^2_ν criterion are also shown for four of these peaks in Figure V.16. The C^2S values obtained are shown in Table V.10. Table V.11 gives the C^2S values from single ℓ-transfer fits.

Note from Table V.10 that for the first two peaks single ℓ-transfers are selected by the minimum-χ^2_ν procedure (with very low χ^2_ν), implying that the peaks corresponding to individual states. The other three peaks appear to

Figure V.18

Angular distribution for the $E_x = 0.98$ MeV state in ^{145}Sm. The solid curve is the minimum-χ^2_ν fit with the DWBA prediction for the $\ell=1$ angular distributions.

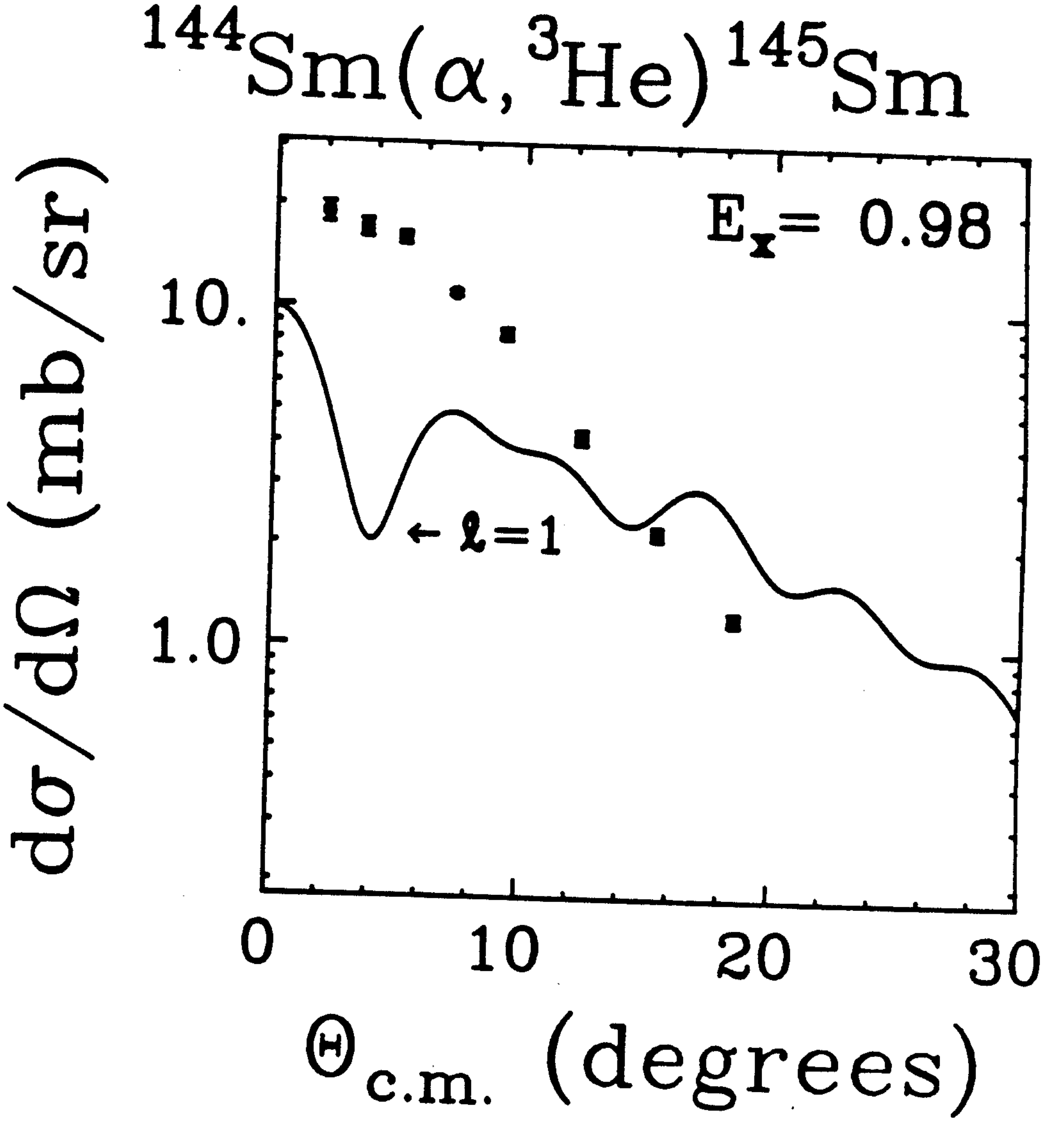

$^{144}Sm(\alpha,{}^3He)^{145}Sm$
$E_x = 0.98$
10.
1.0
$\leftarrow \ell=1$
0
10
20
30
$d\sigma/d\Omega$ (mb/sr)
$\Theta_{c.m.}$ (degrees)

Figure V.18

correspond to groups of states. We have the most confidence in the C^2S values and ℓ-transfers determined for the first two states, since fits with other possible ℓ-transfers are much worse (see Table V.11). The state at 0.29 MeV appears to have $\ell=5$. For the peak at $E_x = 0.91$ MeV, which has the largest cross section in the spectrum, the minimization procedure selected a mixture of $\ell=5$ and 6. But it is very possible that the peak is a single level having either $\ell=5$ or $\ell=6$, since the χ^2_ν values with these single-ℓ fits are only marginally worse than the best fit value.

c) Low-lying states in ^{153}Sm

Four peaks were analyzed as indicated by arrows Figure V.16. No previous strength measurements are available for any state in ^{153}Sm. The set of ℓ values suggested by the Nilsson model ($\ell=1$, 3, 4, 5, 6 and 7) was used to fit the low-lying peaks. The fits to the angular distributions are shown in Figure V.17. The corresponding C^2S values, reported here for the first time, are listed in Table V.10. Table V.11 gives the C^2S values obtained from single ℓ-transfer fits.

The minimum-χ^2_ν procedure selected the ℓ-transfer of 5 for all the peaks, with no admixture of any other ℓ-transfer (Table V.10). But the sum of the C^2S values exceeds the sum rule limit for $\ell=5$. From Table V.11, we see that the χ^2_ν value for the $\ell=6$ fit to the $E_x = 1.74$ MeV peak comes closer to the minimum-χ^2_ν value than in all the other cases. If, on this basis, we assign ℓ=6 to the peak at E_x= 1.74 MeV, then the sum of the C^2S values for the other three peaks does not exceed the sum rule limit for ℓ=5.

d) Low-lying states in ^{155}Sm

Three peaks were analyzed, as indicated by arrows in Figure V.16. No previous strength measurements are available for any state in ^{155}Sm. The set of possible ℓ-transfers (ℓ=1, 3, 4, 5, 6 and 7) was used to fit the low-lying peaks. Fits to the angular distributions are displayed in Figure V.17 and the corresponding C^2S values, reported here for the first time, are listed in Table V.10. Table V.11 lists the C^2S values for single ℓ-transfer fits with the χ^2_ν value from each of the fits given in parenthesis.

The χ^2_ν values listed in Table V.10 range from 1.1 to 13, indicating the quality of the fits varies from good to not so good. No ℓ=5 ($1h_{9/2}$) strength is found. We notice that as the deformation increases with the mass of the Sm isotope, the ℓ-transfers for the analyzed peaks are generally of higher value. The ℓ-transfers of 4 and 7, which correspond to orbits in the next higher subshell above N=126, seem to be present for the E_x= 0.95 MeV peak in ^{155}Sm. However, because the peaks are poorly resolved and because of the uncertainties of the procedure used, it is not possible to make definite ℓ-assignments.

V.6.2 High-lying Neutron Strength in ^{145,149,153,155}Sm

The high-lying portion of the spectra from the (α,^{3}He) reactions are displayed in Figure V.6a. Angular distributions were obtained by "slicing" the spectra from about 2 to 14 MeV excitation energy in 520-keV wide bins. DWBA fits were made to the angular distribution of each slice.

As we have seen in Table V.10, the C^2S values for ℓ=5 ($1h_{9/2}$) exceeds the sum rule limit in the low-lying peaks of ^{145,149,153}Sm. Therefore, the ℓ=5 possibility was excluded from the set of possible ℓ-transfers when fitting the high-lying regions of ^{145,149,153}Sm. Through examination of the expected single particle levels [Bo75a], ℓ-transfers of 1, 3, 4, 6 and 7 were used to fit the high-lying regions in these three nuclei. For ^{155}Sm, ℓ=5 was also included. Typical fits using the minimum-χ^2_ν criterion for different regions of the spectra are shown in Figure V.19. The excitation energies indicated are those at the centers of the energy bin "slices", e.g., the energy bin for the 6.94 MeV region is the interval from 6.68 MeV to 7.20 MeV. As was the case for the (α,t) reactions, in some cases the program did not pick out more than one ℓ-transfer.

Figure V.19

Angular distributions of some high-lying regions in ^{145,149,153,155}Sm after background subtraction. The curves are the minimum-χ^2_ν fits using the DWBA angular distributions. The indicated ℓ values determined by this procedure are indicated.

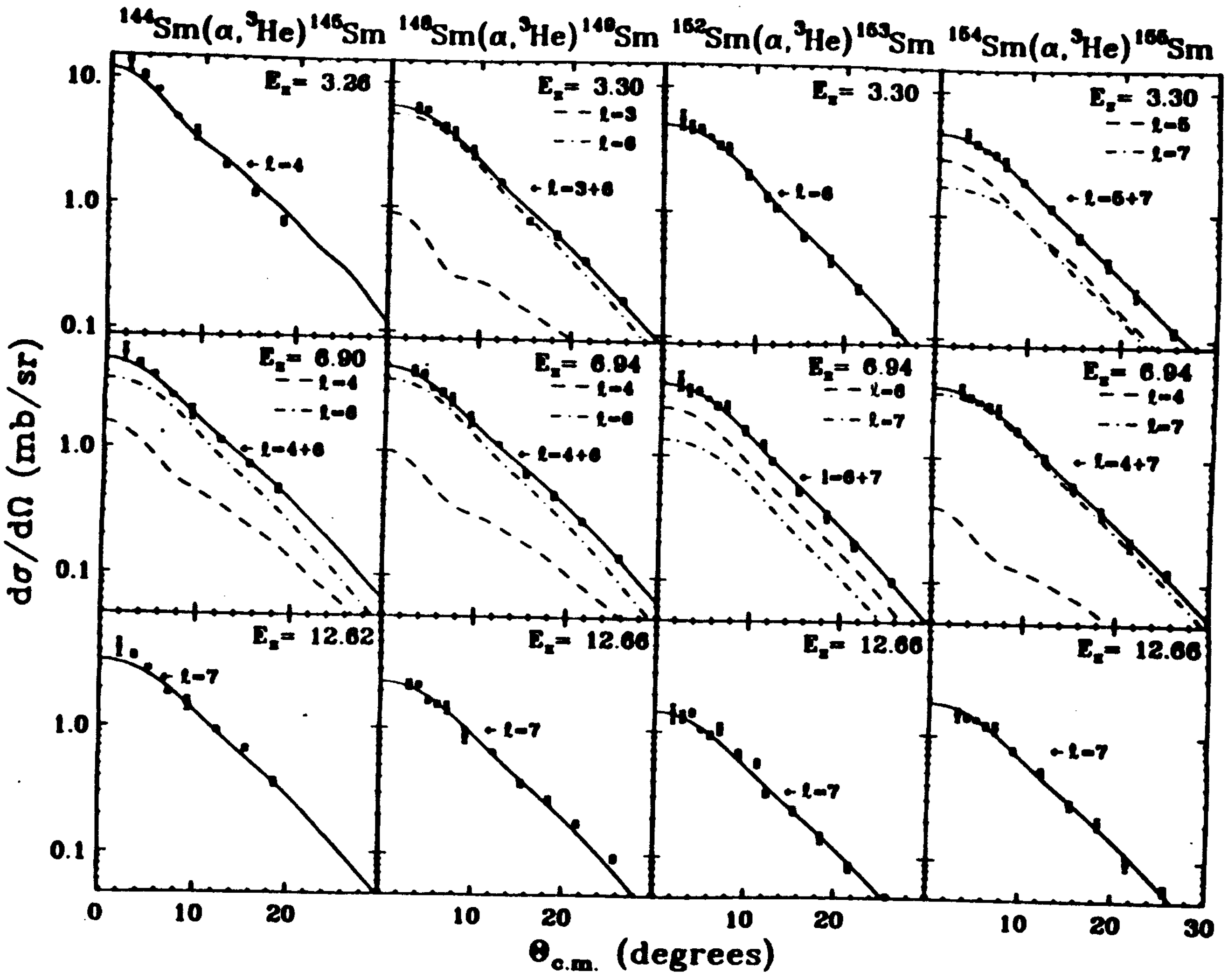

^{144}Sm(α,^{3}He)^{145}Sm
^{148}Sm(α,^{3}He)^{149}Sm
^{152}Sm(α,^{3}He)^{153}Sm
^{154}Sm(α,^{3}He)^{155}Sm
E$_x$= 3.26
← ℓ=4
E$_x$= 3.30
ℓ=3
ℓ=6
← ℓ=3+6
E$_x$= 3.30
← ℓ=6
E$_x$= 3.30
ℓ=5
ℓ=7
← ℓ=5+7
E$_x$= 6.90
ℓ=4
ℓ=6
← ℓ=4+6
E$_x$= 6.94
ℓ=4
ℓ=6
← ℓ=4+6
E$_x$= 6.94
ℓ=6
ℓ=7
← ℓ=6+7
E$_x$= 6.94
ℓ=4
ℓ=7
← ℓ=4+7
E$_x$= 12.62
← ℓ=7
E$_x$= 12.66
← ℓ=7
E$_x$= 12.66
← ℓ=7
E$_x$= 12.66
← ℓ=7
10.
1.0
0.1
dσ/dΩ (mb/sr)
0
10
20
30
Θ$_{c.m.}$ (degrees)

Figure V.19

Not all of the fits for every region for every isotope are displayed, since each reaction has about 25 "sliced" angular distributions. Instead, a 3-dimensional plot of the "sliced" experimental data of $d\sigma/d\Omega$ versus $\Theta_{c.m.}$ versus excitation energy in MeV is shown in Figure V.20. $d\sigma/d\Omega$ is plotted along the z-axis, $\Theta_{c.m.}$ along the y-axis and excitation energy along the x-axis. The scales for all three axes are linear. The conventional experimental angular distribution at any excitation energy is the projection onto the y-z plane. The range of excitation energies is plotted on the x-axis and listed in Table V.12.

High-lying neutron strength distributions in the samarium isotopes are displayed as a function of excitation energy in Figure V.21 and V.22. In Figure V.21, the C^2S values are those obtained by performing minimum-χ^2_ν fits to the experimental angular distributions with a mixture of allowed ℓ-transfers; Figure V.23 displays the corresponding χ^2_ν as a function of excitation energy. In Figure V.22, the C^2S values are those obtained by fitting the experimental angular distributions with a single ℓ-transfer from the allowed set; Figure V.24 displays the corresponding χ^2_ν as a function of excitation energy. Note in Figure V.24 that the χ^2_ν distribution for $\ell=6$ and $\ell=7$ appear very similar up to a certain excitation energy. This is due to the difficulty in distinguishing between the adjacent ℓ-transfers of 6 and 7 in that excitation energy region. We also notice that, except for $\ell=6$ and 7, it is not very difficult to

Figure V.20

A 3-dimensional plot ($d\sigma/d\Omega$ vs $\Theta_{c.m.}$ vs Excitation energy) of experimental angular distributions for the $^{144,148,152,154}Sm(\alpha,{}^3He)^{145,149,153,155}Sm$ reactions. $\Theta_{c.m.}$ varies from 0° to 30° in all four panels of the figure.

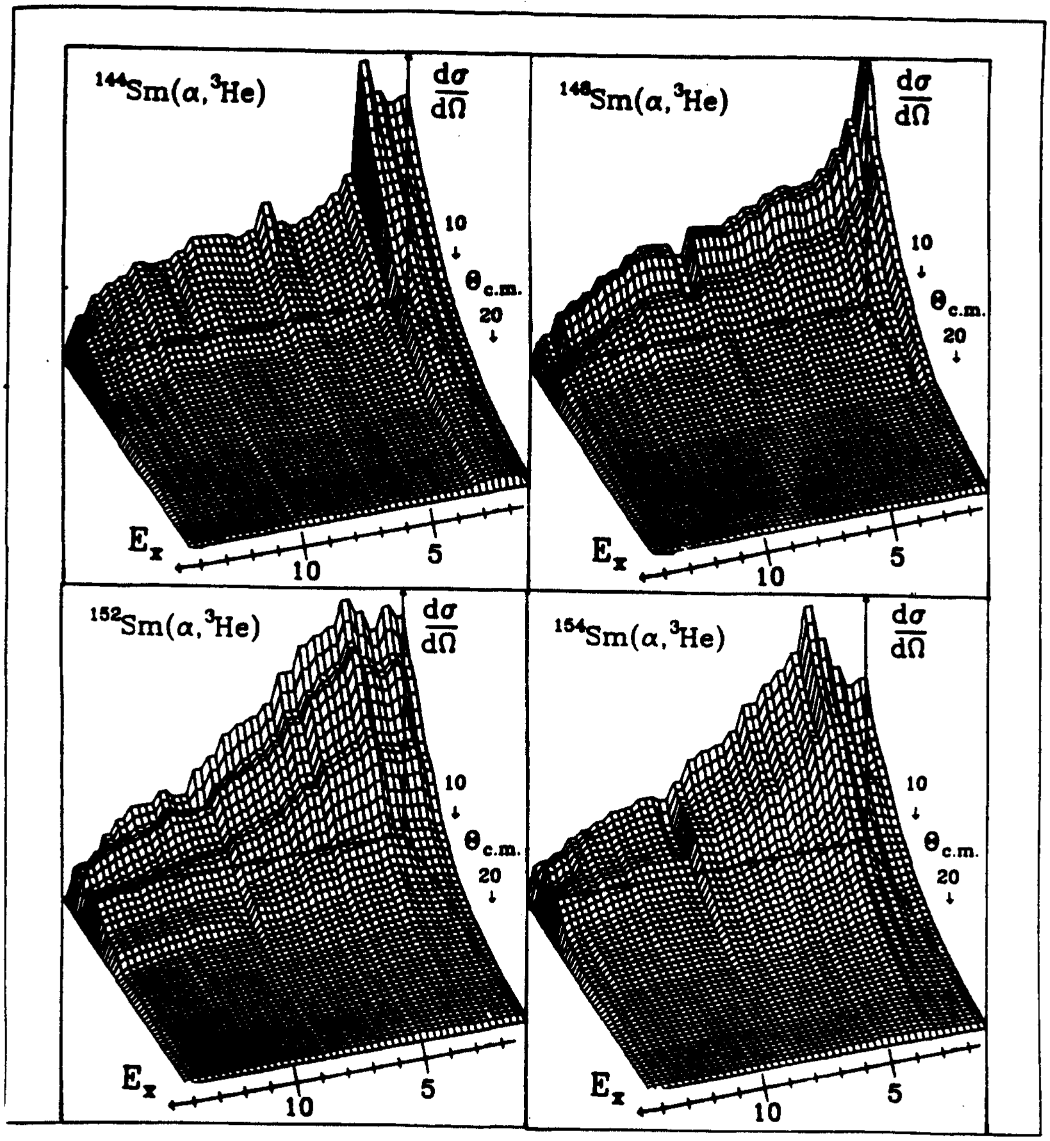

^{144}Sm(α,^{3}He)
$\frac{d\sigma}{d\Omega}$
10
$\theta_{c.m.}$
20
E_x
10
5
^{148}Sm(α,^{3}He)
$\frac{d\sigma}{d\Omega}$
10
$\theta_{c.m.}$
20
E_x
10
5
^{152}Sm(α,^{3}He)
$\frac{d\sigma}{d\Omega}$
10
$\theta_{c.m.}$
20
E_x
10
5
^{154}Sm(α,^{3}He)
$\frac{d\sigma}{d\Omega}$
10
$\theta_{c.m.}$
20
E_x
10
5

Figure V.20

Table V.12

List of the summed transition strengths for the high-lying regions of $^{145,149,153,155}Sm$ from this experiment and from other work. The uncertainties in the summed strengths, which appear in parenthesis, are calculated using the uncertainty in the fitted parameter and in the target thickness.

This experiment			
E_x(MeV) interval	ℓ	ΣC^2S	Final Nucleus
2.7 - 14	3	0.0 (0.0)	^{145}Sm
2.7 - 14	4	1.61 (0.24)	
2.7 - 14	6	1.34 (0.10)	
2.7 - 14	7	0.26 (0.02)	
2 - 14	3	0.58 (0.31)	^{149}Sm
2 - 14	4	1.12 (0.26)	
2 - 14	6	0.88 (0.08)	
2 - 14	7	0.58 (0.05)	
2 - 14	3	0.0 (0.0)	^{153}Sm
2 - 14	4	0.0 (0.0)	
2 - 14	6	1.06 (0.22)	
2 - 14	7	0.34 (0.07)	
2 - 14	3	0.32 (0.30)	^{155}Sm
2 - 14	4	0.31 (0.20)	
2 - 14	5	0.10 (0.04)	
2 - 14	6	0.26 (0.11)	
2 - 14	7	0.83 (0.10)	

Figure V.21

Spectroscopic strength distribution of the fragmented $\ell=3$, 4, 6 and 7 neutron single-particle excitations in ^{145,149,153,155}Sm obtained by performing minimum-χ^2_ν fits to angular distributions measured in the (α,^{3}He) reactions on ^{144,148,152,154}Sm targets. $\ell=3$ corresponds to the $2f_{7/2}$ and $2f_{5/2}$ single-particle states, $\ell=4$ to $2g_{9/2}$, $\ell=6$ to $1i_{13/2}$ and $\ell=7$ to $1j_{15/2}$. The term "scale × 2" in some of the panels means that the indicated scale must be multiplied by two to get the actual scale.

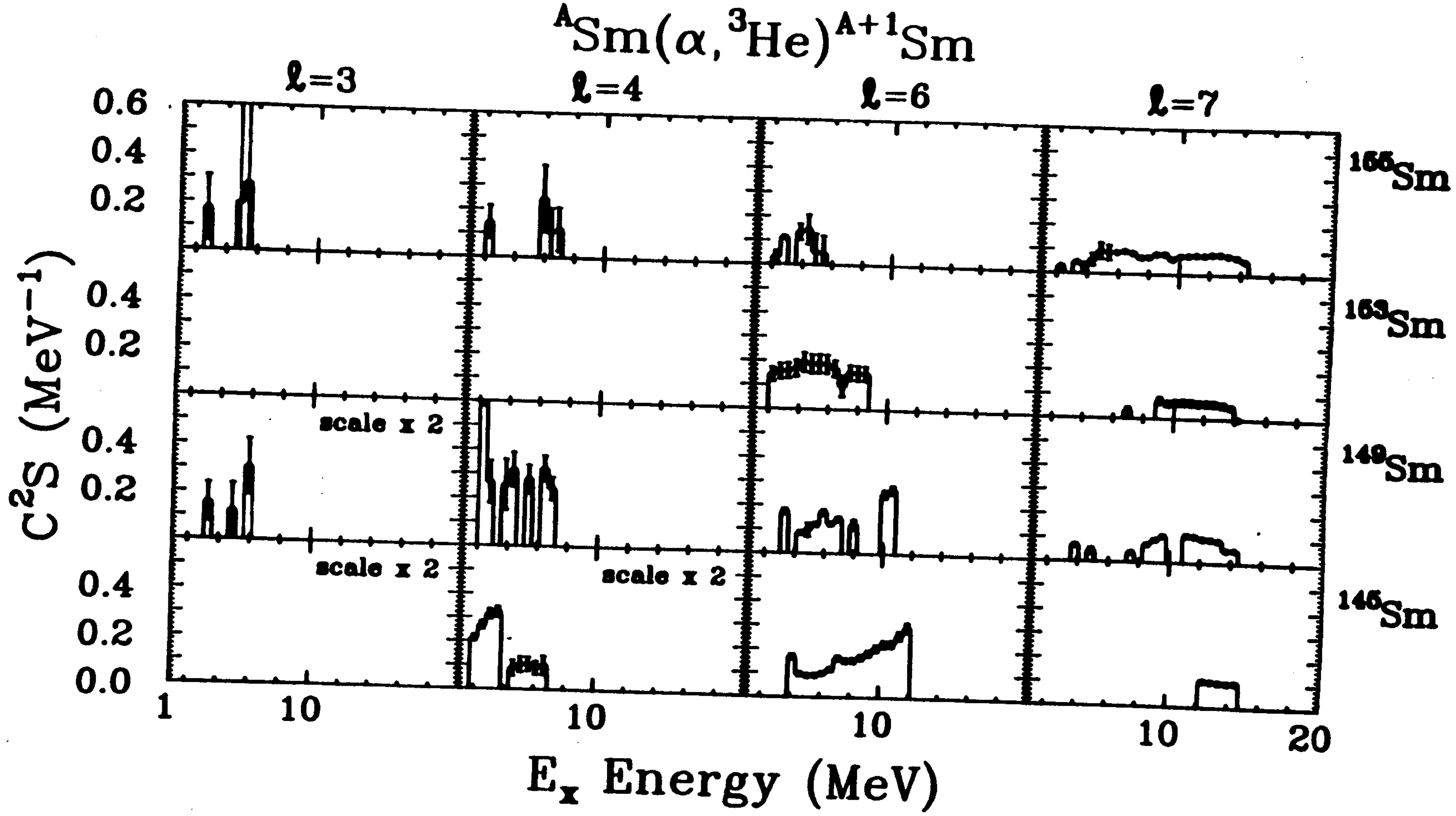
$^{A}Sm(\alpha,{}^{3}He)^{A+1}Sm$
ℓ=3
ℓ=4
ℓ=6
ℓ=7
C^2S (MeV^{-1})
0.6
0.4
0.2
0.4
0.2
0.4
0.2
0.4
0.2
0.0
^{155}Sm
^{153}Sm
^{149}Sm
^{145}Sm
scale x 2
scale x 2
scale x 2
1
10
10
10
10
20
E_x Energy (MeV)

Figure V.21

Figure V.22

As for Figure V.21, except that the strength distributions were obtained by fitting the measured angular distributions with single ℓ-transfers (ℓ=3, 4, 6 and 7). The terms "scale × 2" and "scale × 8" in some of the panels mean that the indicated scales must be multiplied by two and eight, respectively, to get the actual scales.

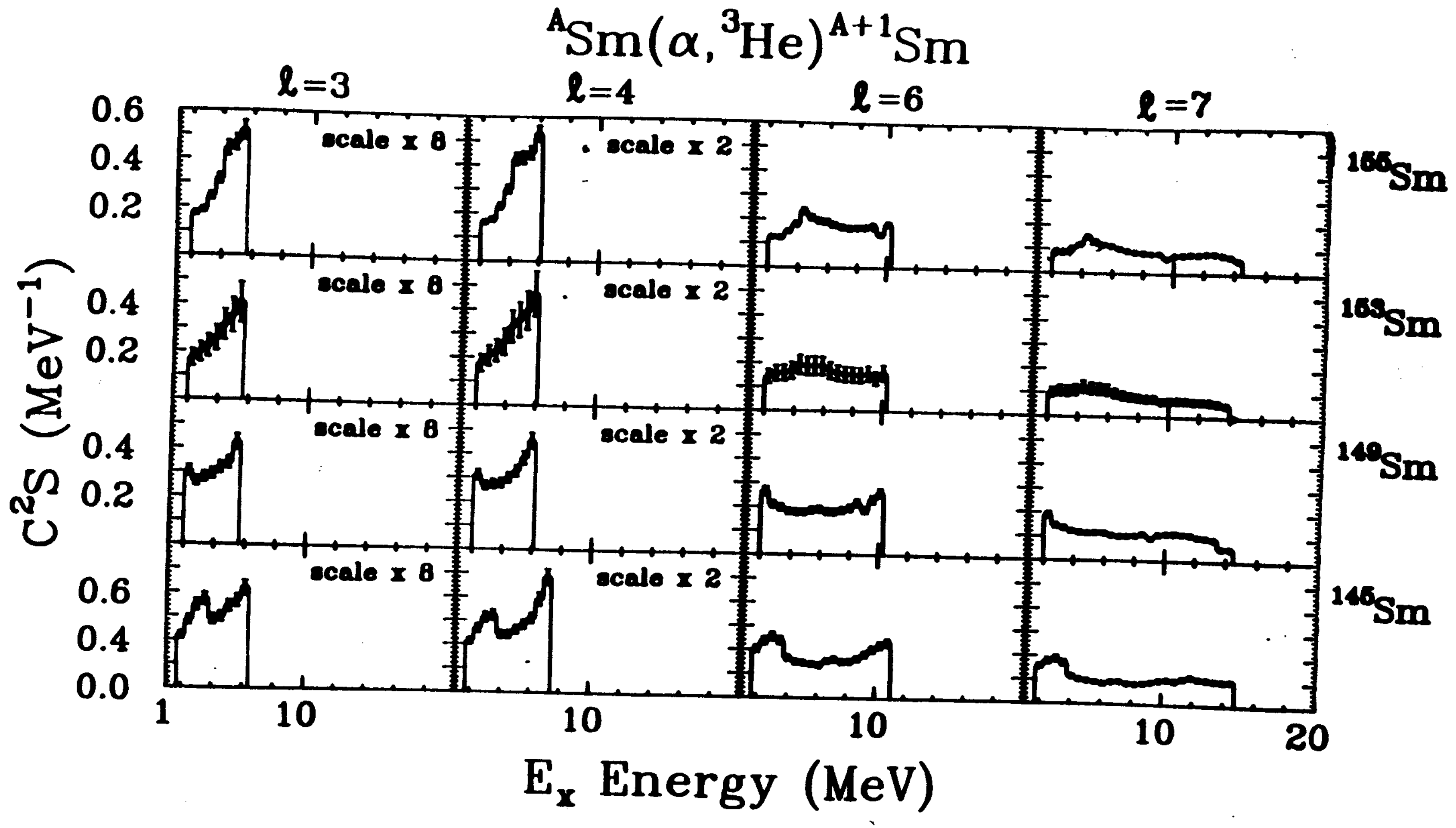
$^{A}Sm(\alpha,{}^{3}He)^{A+1}Sm$
ℓ=3
ℓ=4
ℓ=6
ℓ=7
scale x 8
scale x 2
^{155}Sm
^{153}Sm
^{149}Sm
^{145}Sm
C^2S (MeV^{-1})
0.6
0.4
0.2
0.0
1
10
20
E_x Energy (MeV)

Figure V.22

Figure V.23

The minimum-χ_{ν}^{2} distribution corresponding to the fit that produced the $C^{2}S$ values in Figure V.21.

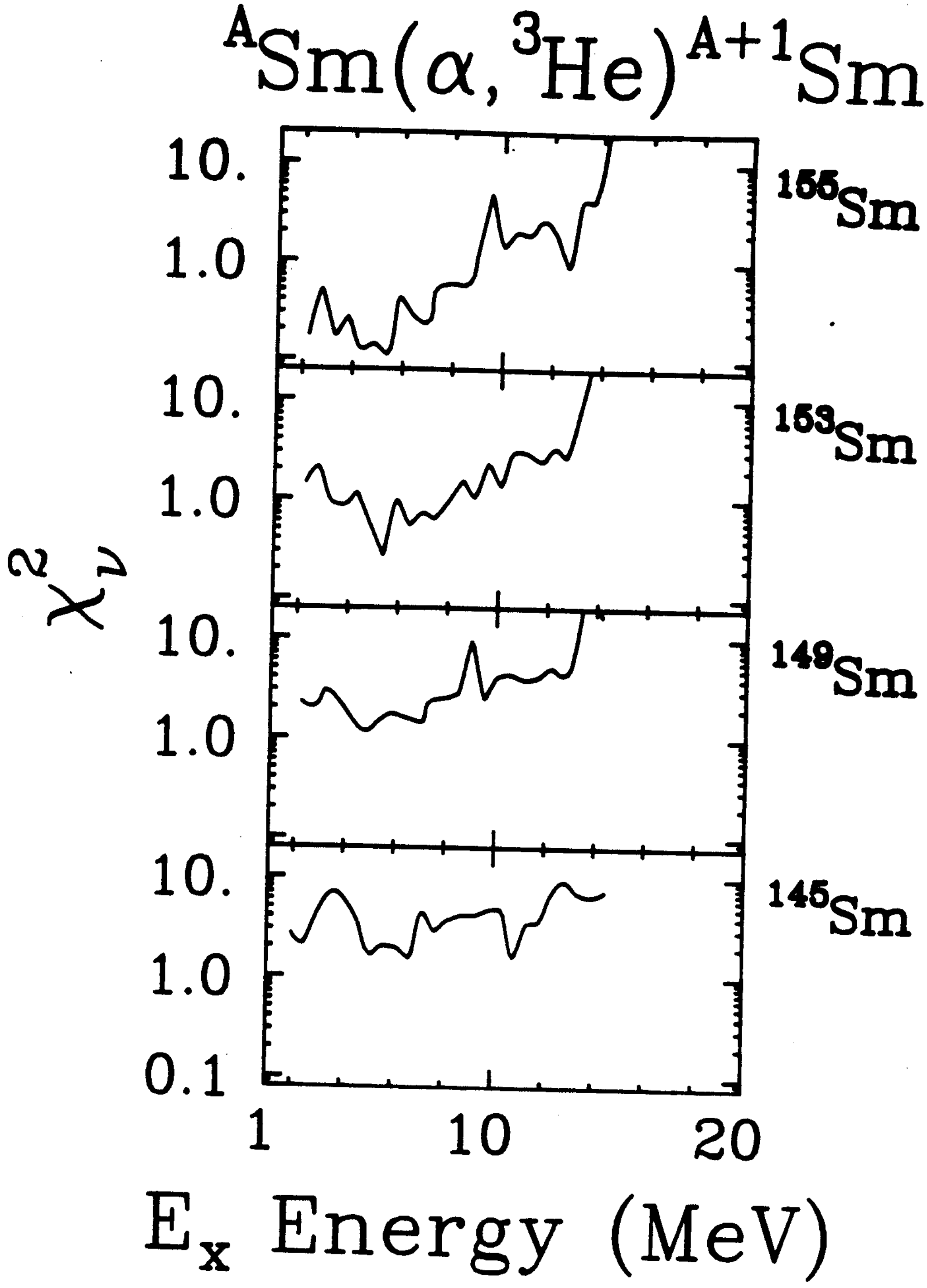

$^{A}Sm(\alpha,{}^{3}He)^{A+1}Sm$
χ^2_ν
10.
1.0
^{155}Sm
10.
1.0
^{153}Sm
10.
1.0
^{149}Sm
10.
1.0
0.1
^{145}Sm
1
10
20
E_x Energy (MeV)

Figure V.23

Figure V.24

The χ^2_ν distribution corresponding to the single-ℓ fits that produced the C^2S values in Figure V.22.

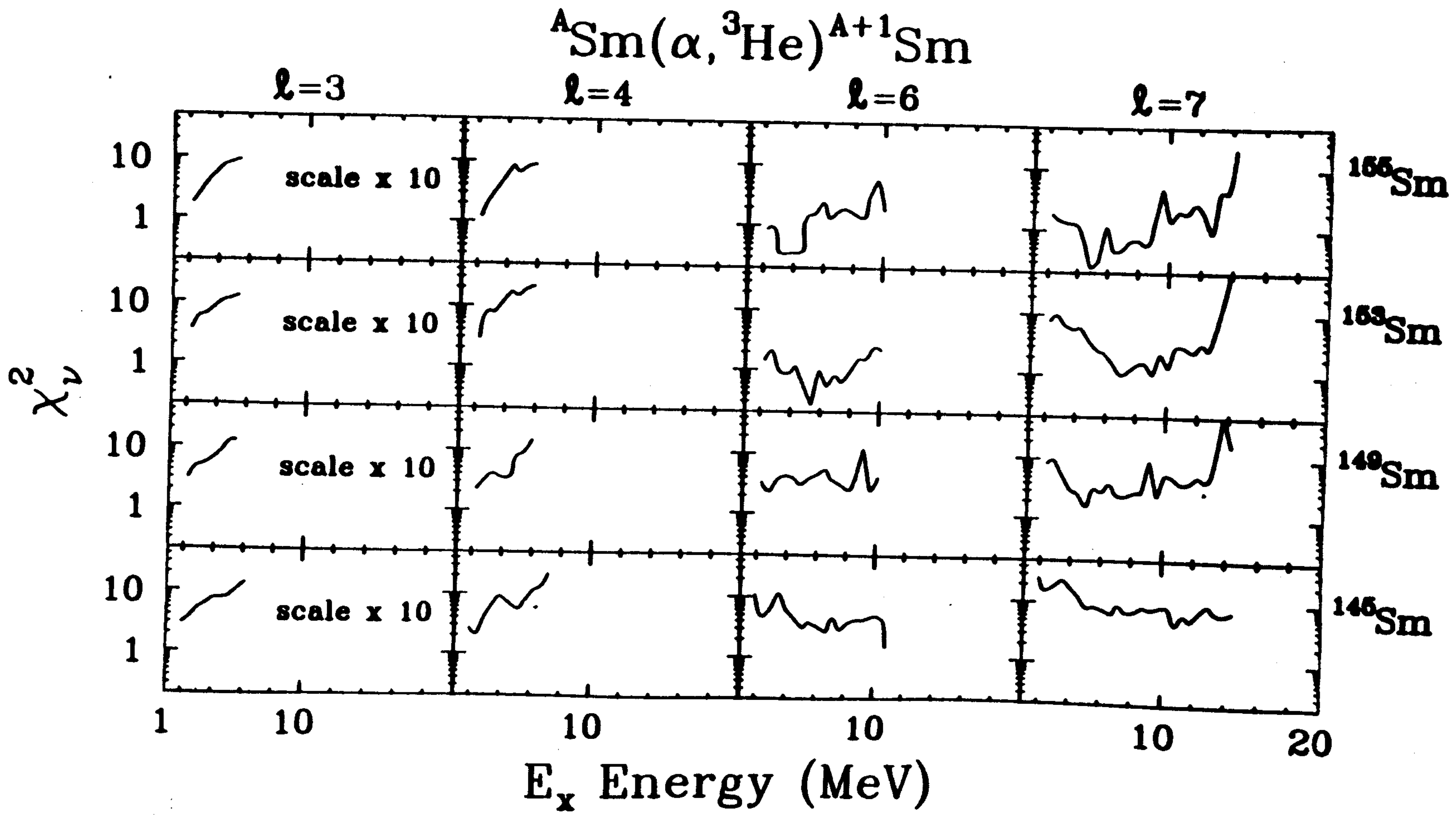
$^{A}Sm(\alpha,{}^{3}He)^{A+1}Sm$
ℓ=3
ℓ=4
ℓ=6
ℓ=7
χ^2_ν
10
1
scale x 10
^{155}Sm
^{153}Sm
^{149}Sm
^{145}Sm
1
10
20
E_x Energy (MeV)

Figure V.24

distinguish between any two ℓ-transfers. Recall, from Chapter III, that above 12 MeV excitation energy, DWBA calculations were feasible only for ℓ=7 and thus C^2S values could be determined only for ℓ=7 above that excitation energy. Comparison of the plots of C^2S with plots of the respective spectra shows the regions of the spectrum in which the various ℓ-transfers dominate.

A summing of the strength was carried out for each of the four odd-mass samarium nuclei and is tabulated in Table V.12. There is very little ℓ=5 strength observed in ^{155}Sm. In the three lighter Sm nuclei, as mentioned earlier, most of the ℓ=5 strength is observed in the low-lying region of the spectra. The lack of ℓ=5 neutron strength in ^{155}Sm suggests that the $1h_{9/2}$ orbit becomes occupied as the neutron number increases. The summed ℓ=3 strength has large uncertainties; in ^{155}Sm, the uncertainty has about the same magnitude as the strength. The sum rule limit is exceeded for ℓ-transfers of 4 and 6 in ^{145}Sm. This may be explained in two ways. First, perhaps not enough background is subtracted in the excitation energy region (2 to 14 MeV) under consideration, or second, the ℓ=3 and 4 strengths may need to be slightly redistributed.

Very recently, theoretical predictions [Ma86] were made for the strength distributions of neutron single-particle excitations in deformed samarium (^{153,155}Sm) and proton single-particle excitations in deformed europium (^{153,155}Eu) isotopes. The C^2S values presented in this Chapter will be compared with these and other nuclear structure calculations in the next Chapter.

CHAPTER VI

COMPARISON WITH NUCLEAR STRUCTURE MODELS

This work, which represents the first attempt to find high-lying particle state strength in deformed nuclei, is also unique in that it presents a systematic study of both proton and neutron particle states using the same set of isotopes (samarium) as targets. In this Chapter, the strength distributions already obtained in Chapter V are compared with two nuclear structure model calculations. This discussion contains four sections. In the first section, a comparison of the results obtained from the ^{144}Sm(α,t)^{145}Eu reaction at 80 MeV [Ga85a] and our work at 100 MeV (discussed in Chapter V) is presented. The second section gives a brief summary of two theoretical models that predict strength distributions for particle states in the samarium isotopes. These are the quasi-particle phonon model (QPPM) and the Interacting Boson-Fermion Approximation model (IBFA). Comparison of the theoretical (QPPM) and experimental strength distributions for protons in ^{145,153,155}Eu and neutrons in ^{153,155}Sm are presented. Also, the IBFA model predictions are compared with the proton strength distributions in ^{149,153,155}Eu. The third section presents the conclusions. Finally, in the fourth section, suggestions are made for improvement in the analysis of single-nucleon transfer data to extract spectroscopic information at high excitation energies.

VI.1 THE ^{144}Sm(α,t)^{145}Eu REACTION AT 80 MEV AND 100 MEV

In this section, we compare the results of the ^{144}Sm(α,t)^{145}Eu reaction at 80 MeV and 100 MeV. The histograms in Figure VI.1 display the C^2S values determined at the two energies as a function of excitation energy; the top part of the figure gives the results obtained at 80 MeV [Ga85a] and the bottom part the results obtained from the present experiment at 100 MeV.

For the C^2S values from the present work, error bars are shown which reflect uncertainties due to both the fitting procedure and the absolute normalizations. For the ℓ=3 and 5 transfers, there are differences between the 80 and 100 MeV data sets. Compared with the 80 MeV data, there appears to be more ℓ=3 strength and less ℓ=5 strength above E_x= 6 MeV in the 100 MeV data. The distribution of ℓ=6 strength in the two data sets is somewhat similar, except that the data taken at 100 MeV show more strength above 11 MeV of excitation energy. Besides the difference in the bombarding energy, the analyses of the two data sets were also somewhat different. For example, the background

Figure VI.1

Comparison between theoretical and experimental proton strength distributions for the high-lying subshells in ^{145}Eu. The theoretical distributions [St83] are the thick smooth curves and the experimental distributions are in histogram form. The term "scale × 2" in some of the panels means that the indicated scale must be multiplied by two to get the actual scale.

Figure VI.1a. (Top figure) Experimental distributions obtained from the ^{144}Sm(α,t)^{145}Eu reaction at 80 MeV incident energy [Ga85a].

Figure VI.1b. (Bottom figure) Experimental distributions obtained from the same reaction at 100 MeV incident energy (present work).

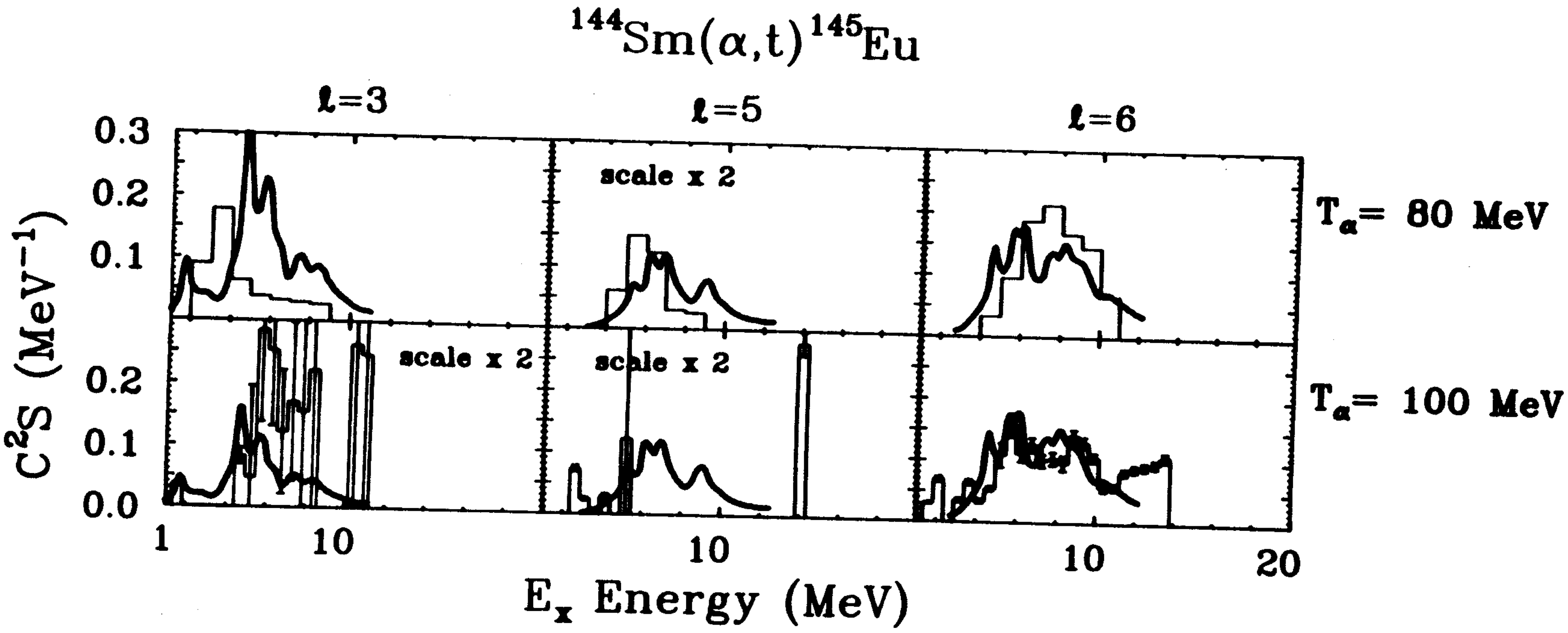
^{144}Sm(α,t)^{145}Eu
ℓ=3
ℓ=5
ℓ=6
scale x 2
scale x 2
scale x 2
T$_\alpha$= 80 MeV
T$_\alpha$= 100 MeV
C^{2}S (MeV^{-1})
0.3
0.2
0.1
0.2
0.1
0.0
1
10
10
10
20
E$_x$ Energy (MeV)

Figure VI.1

subtractions were carried out differently. As mentioned before, the results at 80 MeV were obtained using an empirical background subtraction. Another difference is the uncertainty in the ℓ-values obtained from the 100 MeV data. This uncertainty is ±1 and it critically affects our entire determination of C^2S values.

VI.2 MODELS FOR POSITION AND WIDTH OF SINGLE-PARTICLE EXCITATIONS

The two models discussed here are the quasi-particle phonon model (QPPM) [Ma76,So80] and the Interacting Boson-Fermion Approximation model (IBFA) [Sc82]. Both models are derived from a particle-core coupling scheme and predict single-particle strength functions. The spectroscopic strength (defined in Chapter III) as a function of excitation energy is called the strength function. In the models the strength function takes on the Breit-Wigner form [Bo69]

$$C^2(\omega) = \frac{\Gamma_2(\omega)}{[\varepsilon - \omega]^2 + \Gamma_2(\omega)^2} \qquad (\text{VI.1})$$

Here we shall only discuss the assumptions and the input each model uses to calculate the strength distribution. The derivations of the two models are discussed in the references given above.

VI.2.1 The Quasi-Particle Phonon Model (QPPM)

The quasi-particle phonon model describes the fragmentation of the quasi-particle strength due to the interaction of the quasi-particle with the phonon excitation modes of the core. The term "phonon" used here describes excitations of the core. Among the phonons included in the model are the low-lying quadrupole (J=2) and octupole (J=3) phonons, multipole phonons with J > 3, and spin-multipole phonons. Both isoscalar and isovector modes are considered for the phonons. The effect of the odd quasi-particle on the phonon structure is discounted, since the effect is minimal. The Pauli principle is only taken into account to a limited extent. These features of the model influence the results in the low (~1 - 2 MeV) excitation energy region. The interaction of the quasi-particle with the phonon does not use any free parameters. The model predicts the position ω, width $\Gamma_2(\omega)$ and magnitude $C^2(\omega)$ of the strength function. The relation between these quantities is given in equation (VI.1).

The comparison of the QPPM predictions with the experimental proton and neutron strength distributions for the high-lying excitations in ^{145,153,155}Eu and ^{153,155}Sm is presented in three parts. Parts one and two discuss the results for the proton strength distributions in ^{145}Eu and in ^{153,155}Eu, respectively. The third part discusses the results for the neutron strength distributions in ^{153,155}Sm.

Comparison between theoretical (QPPM) and experimental proton strength distributions in ^{145}Eu:

In Figure VI.1, the predictions of the quasi-particle phonon model for the $2f_{7/2}$ ($\ell=3$), $1h_{9/2}$ ($\ell=5$) and $1i_{13/2}$ ($\ell=6$) proton strength distributions in ^{145}Eu are shown by the solid curves. They are superimposed on the data plotted as histograms. The experimental $\ell=3$ C^2S distribution extracted at 100 MeV agrees, within the uncertainties of the measurement, with the prediction. For $\ell=5$, there seems to be a large strength missing in the experimental distribution at 100 MeV in the excitation energy region from 6 to 10 MeV. This may be due to the uncertainty in determining ℓ-transfers to within ±1 in regions where different ℓ-transfers overlap, which would affect the magnitude of the C^2S values extracted. For $\ell=6$, the experimental distribution from the present work agrees with the prediction up to about E_x= 11 MeV but is larger than the prediction at higher excitation energies. This may be because the estimated background was not high enough at the larger excitation energies or because the determination of C^2S values is difficult in excitation energy regions where different ℓ-transfers overlap.

Thus the comparison between the strength distributions for individual ℓ-values predicted by the QPPM and those determined experimentally at 100 MeV in the present work is not satisfactory. As we have pointed out, the experimental distributions are suspect because of the uncertainty in identifying ℓ-transfers. But it is possible that the QPPM predictions are also not very reliable. In order to assess this, the model was tested in a manner that bypassed the difficulty with the experimental distributions for the individual ℓ-transfers. It was concluded that the model predictions for ^{145}Eu are quite satisfactory. The test also shed greater light on the limitations of our technique for determining ℓ-values and C^2S strengths.

The test was performed in the following way. A theoretical spectrum was obtained by starting with the predicted $2f_{7/2}$, $1h_{9/2}$ and $1i_{13/2}$ strength distributions, which overlap in excitation energy, and converting them using the DWBA calculations (with N=36) into a double differential cross-section (mb/sr MeV). This was done for angles of 2°, 7° and 12°; the excitation energy range covered was from 0 to 13 MeV. The comparison between the background-subtracted experimental spectrum and the theoretical spectrum at 2°, 7° and 12° for ^{145}Eu is shown in the left panels of Figure VI.2. (The excitation energy range from 0 to 1.5 MeV is not plotted, as it is dominated by orbitals not included in the theoretical spectrum.) There is good agreement at all three angles. This demonstrates the validity of the QPPM model and confirms the strong overlap between the $2f_{7/2}$, $1h_{9/2}$ and $1i_{13/2}$ proton strength functions in the energy range from 3 MeV to about 11 MeV. The width of the overall distribution is about the same in

Figure VI.2

Comparison between the experimental spectrum (solid histogram) for proton states in ^{145,153,155}Eu and the predicted spectrum (thick dashed histogram) obtained by the conversion of theoretical strength functions at three angles. The theoretical strength functions for ^{145}Eu are those shown in Figure VI.1 [St83] and for ^{153,155}Eu are those shown later in Figure VI.3 [Ma86].

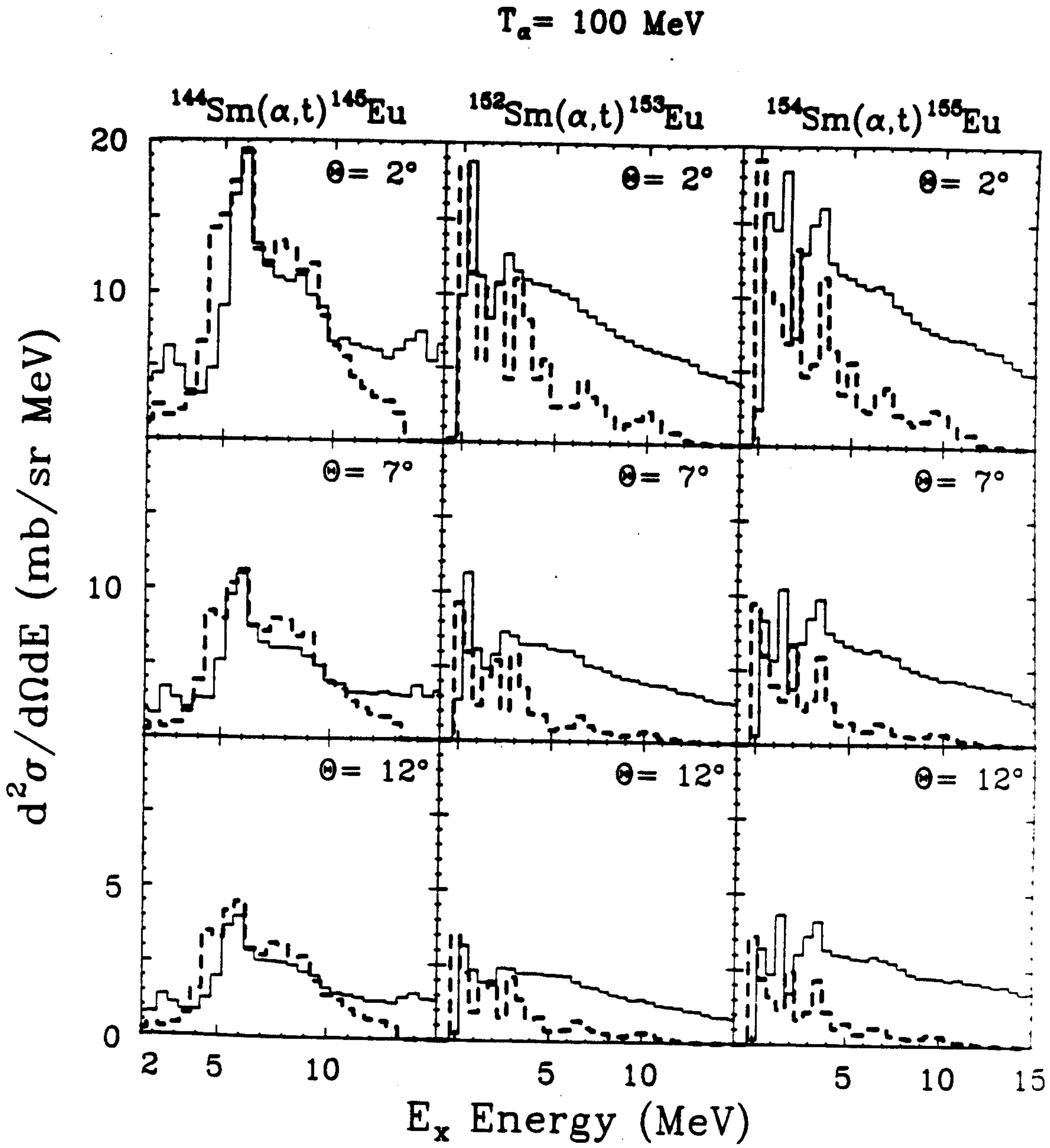

T_α= 100 MeV
^{144}Sm(α,t)^{145}Eu
^{152}Sm(α,t)^{153}Eu
^{154}Sm(α,t)^{155}Eu
Θ= 2°
Θ= 7°
Θ= 12°
20
10
5
0
2
5
10
15
$d^2\sigma/d\Omega dE$ (mb/sr MeV)
E_x Energy (MeV)

Figure VI.2

the theoretical and experimental spectra, though slightly smaller in the latter. This may indicate that the damping of the high-lying orbitals considered is slightly smaller experimentally than is predicted theoretically. The excess experimental cross section seen at all three angles for $E_x >$ 10 MeV may be due to some orbital(s) not included in the theoretical spectrum.

Comparison between theoretical (QPPM) and experimental proton strength distributions for the high- lying region in ^{153,155}Eu:

Figure VI.3 displays both the predicted (QPPM) [Ma86] and experimental strength distributions for the high-lying proton orbits in ^{153,155}Eu. The predictions are for the $2f_{7/2}$ ($\ell=3$) and $1h_{11/2}$ ($\ell=5$) orbits. As before, the experimental C^2S values are greater than the predicted values. At least part of the disagreement in the case of $\ell=3$ is due to the fact that the experimental strength distribution has contributions from both $2f_{7/2}$ and $2f_{5/2}$, whereas the theoretical distribution has only the former. Similarly, in the case of $\ell=5$, some of the strength in ^{153}Eu below 10 MeV of excitation energy may be due to the $1h_{9/2}$ orbital while the strength in ^{153,155}Eu above 10 MeV of excitation energy may actually be due to the $1i_{13/2}$ orbital (in view of the uncertainty in the determination of ℓ-transfer values). The Nilsson model shows that the $1h_{9/2}$

Figure VI.3

Comparison between theoretical [Ma86] and experimental proton strength distributions for the high-lying subshells in ^{153,155}Eu.

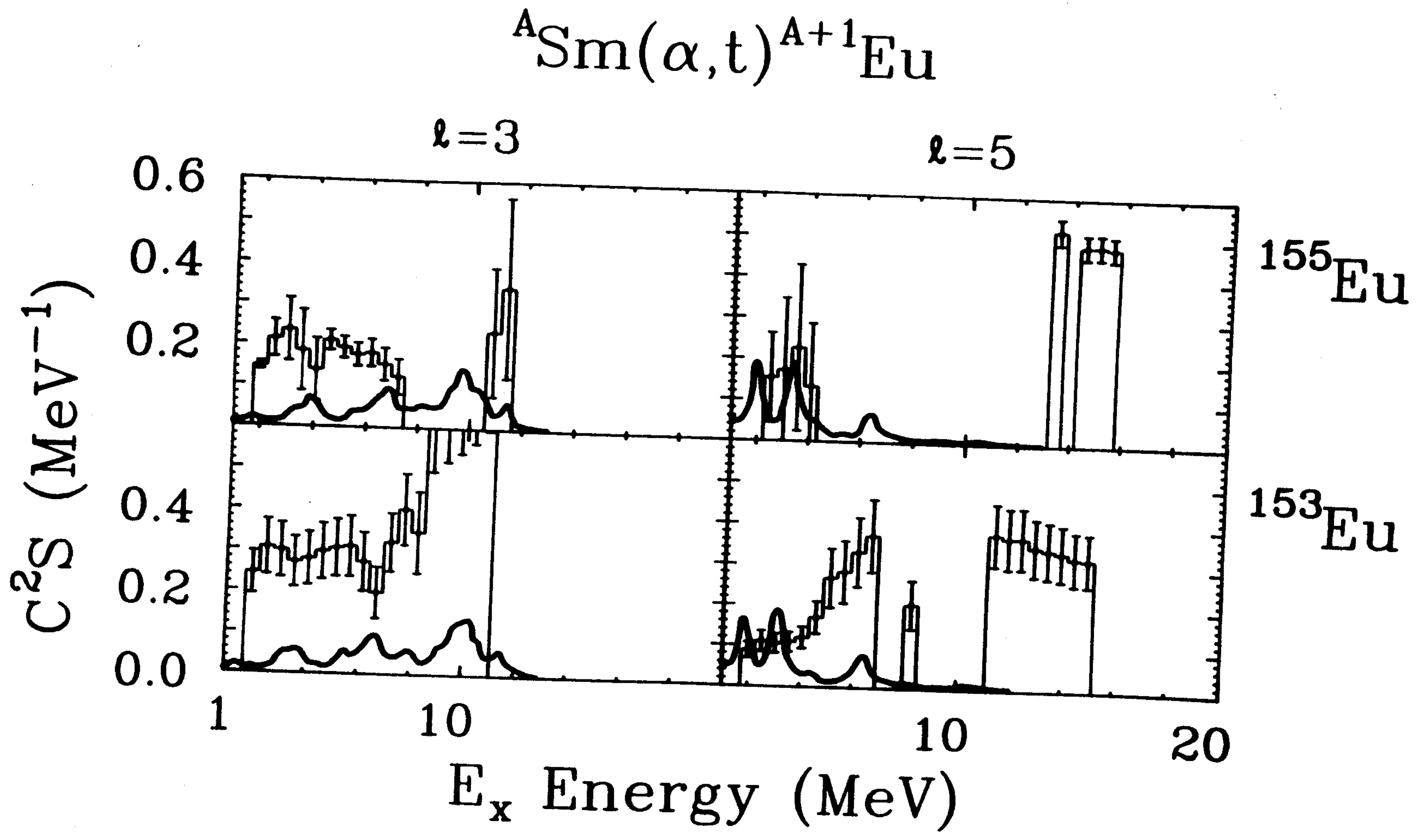
^{A}Sm(α,t)$^{A+1}$Eu
ℓ=3
ℓ=5
^{155}Eu
^{153}Eu
C^{2}S (MeV^{-1})
0.6
0.4
0.2
0.4
0.2
0.0
1
10
10
20
E$_x$ Energy (MeV)

Figure VI.3

and $1i_{13/2}$ excitations are possible in the high-lying excitation energy region of ^{153,155}Eu. But the theoretical strength distributions for the $1h_{9/2}$ and $1i_{13/2}$ orbitals were not calculated in [Ma86] and so are not shown in Figure VI.3.

It is interesting to note that the theoretical proton strength distributions are similar in ^{153}Eu and ^{155}Eu for both the $2f_{7/2}$ and $1h_{11/2}$ orbitals, whereas the experimental strength distributions are different. The similarity seen in the theoretical calculations is probably a consequence of the fact that the deformation parameters for the two nuclei are very similar, while the difference in the experimental strengths may be due to the uncertainty of ±1 in determining ℓ-transfers.

As in the case of ^{145}Eu, a comparison was made (Figure VI.2) between the experimental spectra (background-subtracted) taken at 2°, 7° and 12° for ^{153,155}Eu and the corresponding theoretical spectra obtained by adding up the contributions of the predicted $3s_{1/2}$, $2d_{5/2}$, $2d_{3/2}$, $2f_{7/2}$, $1g_{7/2}$ and $1h_{11/2}$ strength distributions [Ma86]. The low ℓ-transfers (ℓ=0 and ℓ=2) contributed only about 10% to the total cross section of the theoretical spectrum. Unlike the ^{145}Eu case, the plots for ^{153,155}Eu in Figure VI.2 extend down to E_x= 0 MeV. As in the ^{145}Eu case, the theoretical cross sections have generally the same magnitude as the experimental cross sections at all angles for low excitation energies, but there is a marked (and systematic) disagreement for excitation energies above 3 MeV. This is at least partly due to the neglect (because of nonavailablity) of the $1h_{9/2}$ and $1i_{13/2}$ strength distributions in the theoretical spectra; both of them would have made substantial contributions to the spectra.

Comparison between theoretical (QPPM) and experimental neutron strength distributions for the high-lying region in ^{153,155}Sm:

Figure VI.4 displays both the predicted (QPPM) [Ma86] and experimental strength distributions for the high-lying neutron orbits in ^{153,155}Sm. The prediction are for the $2f_{7/2}$ (ℓ=3), $2f_{5/2}$ (ℓ=3), $2g_{9/2}$ (ℓ=4), $1h_{9/2}$ (ℓ=5) and $1i_{13/2}$ (ℓ=6) orbits. In ^{155}Sm, experiment agrees quite well with theory for the $1i_{13/2}$ and $2f_{5/2}$ orbits, but disagrees in the shape and magnitude for $2g_{9/2}$. In ^{153}Sm, there is disagreement between experiment and theory for all the orbits. No strength at all is found for the $2f_{7/2}$, $2f_{5/2}$ and $2g_{9/2}$ orbits in ^{153}Sm. This discrepancy may be partly due to incorrect ℓ assignments and the consequent inaccuracy of experimental strengths determined in the overlapping regions. This statement is supported by the fact that all the experimental strength distributions shown in Figure VI.4 have large error bars, indicating the great uncertainty in determining the strengths. Part of the strength ascribed to the $1i_{13/2}$ (ℓ=6) orbit in ^{153}Sm may possibly be ℓ=7

Figure VI.4

Comparison between theoretical [Ma86] and experimental neutron strength distributions for the high-lying subshells in ^{153,155}Sm. The term "scale × 2" in some of the panels means that the indicated scale must be multiplied by two to get the actual scale.

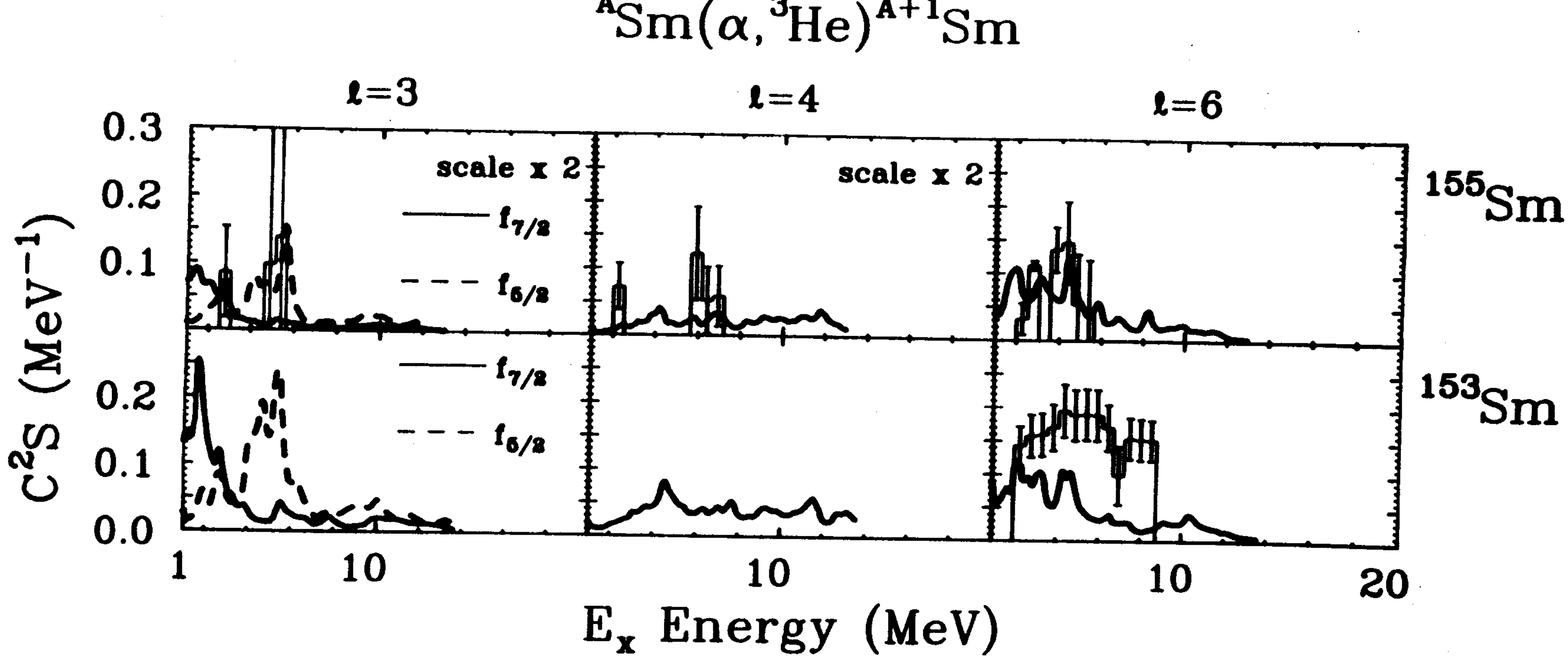
$^{A}Sm(\alpha,{}^{3}He)^{A+1}Sm$
ℓ=3
ℓ=4
ℓ=6
scale x 2
scale x 2
$f_{7/2}$
$f_{5/2}$
$f_{7/2}$
$f_{5/2}$
^{155}Sm
^{153}Sm
C^2S (MeV^{-1})
0.3
0.2
0.1
0.2
0.1
0.0
1
10
10
10
20
E_x Energy (MeV)

Figure VI.4

strength. The Nilsson model shows that the $1j_{15/2}$ excitation should be present in the high-lying region of ^{153,155}Sm. However, the strength distribution for this excitation was not calculated in the recent work by Malov et al. [Ma86].

As was the case for the theoretical proton strength distributions, theoretical neutron strength distributions are similar in ^{153}Sm and ^{155}Sm. For example, the $2f_{7/2}$ and $2f_{5/2}$ strengths in ^{153}Sm and ^{155}Sm have the respective centroids separated by the same amount, about 3 MeV. These similarities in the neutron strength distributions suggest that there is little difference in the structure of these two deformed nuclei (^{153}Sm and ^{155}Sm).

As before, theoretical spectra were obtained at angles of 3°, 7° and 12° by adding up the contributions of the $3p_{1/2}$, $3p_{3/2}$, $2f_{5/2}$, $2f_{7/2}$, $2g_{9/2}$, $1h_{9/2}$ and $1i_{13/2}$ strength distributions.. The $\ell=1$ cross section from the $3p_{1/2}$ and $3p_{3/2}$ strengths is only about 2% of the total theoretical cross section. In Figure VI.5, the theoretical spectra at the three angles are compared with the corresponding background-subtracted experimental spectra. The theoretical spectra have somewhat higher cross sections than the experimental spectra at very low excitation energies ($E_x < 1$ MeV), about the same cross sections for $E_x = 2\text{-}5$ MeV and considerably less cross sections for $E_x > 5$ MeV. As in the ^{153,155}Eu cases, there is not much difference between the theoretical spectra of ^{153,155}Sm; the experimental spectra

Figure VI.5

Same as Figure VI.2 applied to the high-lying neutron states in ^{153,155}Sm.

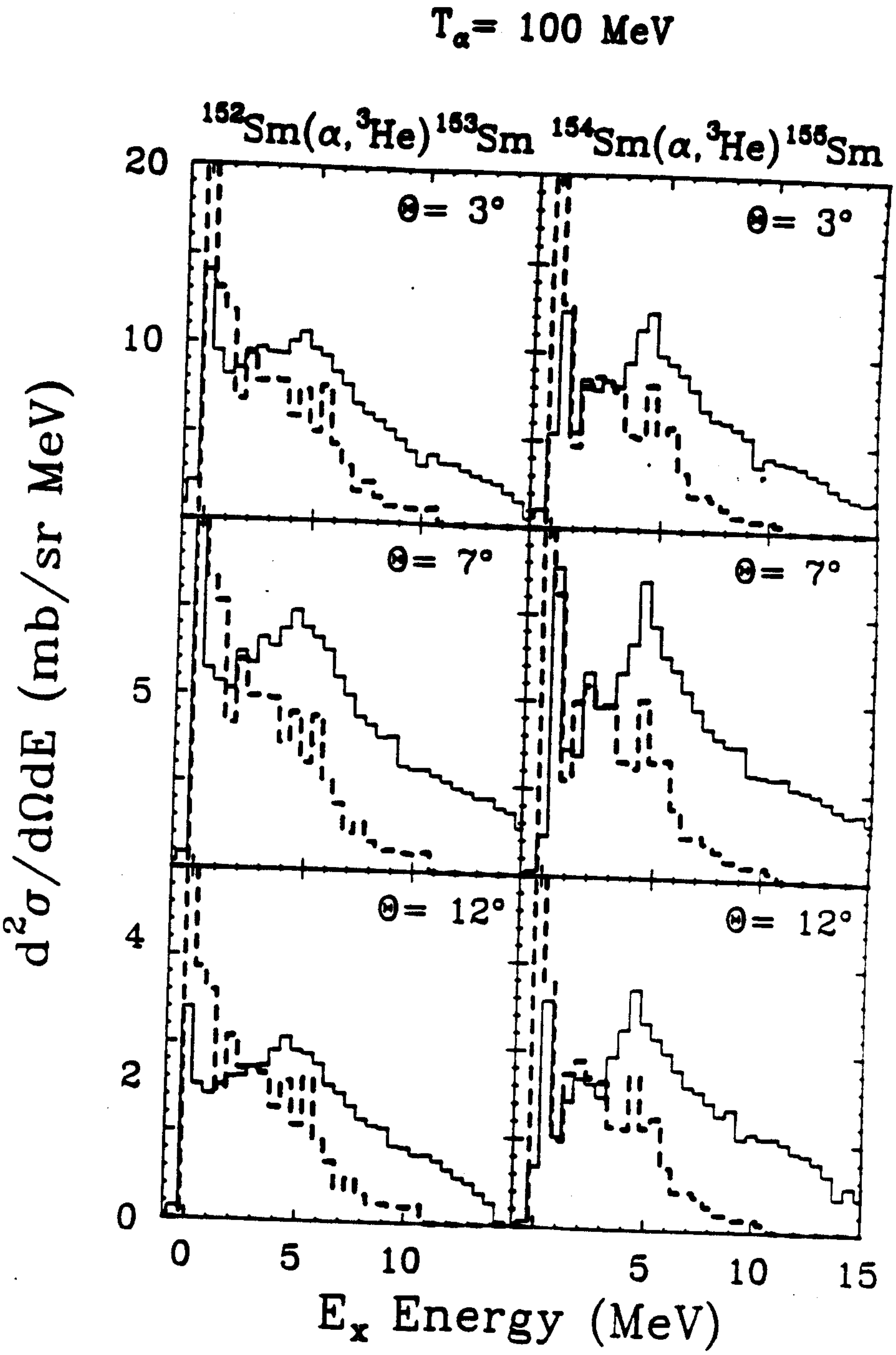

T_α= 100 MeV
^{152}Sm(α,^{3}He)^{153}Sm
^{154}Sm(α,^{3}He)^{155}Sm
Θ= 3°
Θ= 3°
Θ= 7°
Θ= 7°
Θ= 12°
Θ= 12°
20
10
5
4
2
0
0
5
10
5
10
15
d$^2\sigma$/dΩdE (mb/sr MeV)
E$_x$ Energy (MeV)

Figure VI.5

are also rather similar to each other but not, as just mentioned, to the theoretical spectra. The excess experimental cross section occurring for $E_x > 3$ MeV may represent the contribution of the $1j_{15/2}$ neutron excitation. Until the $1j_{15/2}$ strength calculation is made, it would be premature to draw a conclusion about the spreading widths of individual single-particle excitations.

VI.2.2 The Interacting Boson-Fermion Approximation Model (IBFA)

The IBFA model is a particle-core coupling scheme. Its predictive power depends upon parameters in the Hamiltonian some of which are constants while others are allowed to vary slowly with the mass number of the nucleus [Sc82]. The Hamiltonian contains a boson core, a single-particle fermion component and a component describing the coupling of the fermions with the bosons. The monopole-monopole interaction term in the fermion-boson coupling component is weak enough to be ignored. The Pauli principle is automatically incorporated in the coupling component. The model predicts the excitation energy ω and strength $C^2(\omega)$ of various single-particle excitations but does not treat their widths properly. To begin with, the entire predicted strength is concentrated at certain discrete energies ω. For comparison with experimental data, each of these "spikes" is then spread out over a range of excitation energies using the

Breit-Wigner form (VI.1) with an arbitrary, energy independent spreading width $\Gamma_2(\omega)$.

This model was used to predict the $1h_{9/2}$ proton strength distribution in ^{149,153,155}Eu [Sc85]. (Because of certain computational difficulties, the model was not applied to the nearly spherical ^{145}Eu nucleus or to neutron strength distributions in the odd-mass Sm nuclei of interest to us.) The predicted $1h_{9/2}$ proton strengths were spread out using a width $\Gamma_2(\omega)$= 0.5 MeV. The results are shown in the right half of Figure VI.6. They are to be compared with the experimental ℓ=5 strength distributions we have obtained for ^{149,153,155}Eu, which are shown in the left half of the figure. These data were already presented in Figure V.12. Even though a few centroid positions seem to match well, the overall comparison between the experimental strength distributions and the IBFA predictions is poor. We have not pursued this matter further.

VI.3 CONCLUSIONS

As mentioned in the Introduction, our goal was to obtain systematic information on high-lying proton and neutron particle states over a range of spherical to deformed nuclei. Single-nucleon stripping reactions provide the only convenient and generally applicable means presently available for this purpose. The reactions we chose were (α,t) and $(\alpha,{}^3He)$ on targets of ^{144,148,152,154}Sm at a

Figure VI.6

Comparison of the experimental $\ell=5$ proton strength distributions in $^{149,153,155}Eu$ (shown in histogram form on the left hand side) with the corresponding IBFA-model prediction for the $1h_{9/2}$ strength distributions (shown on the right hand side).

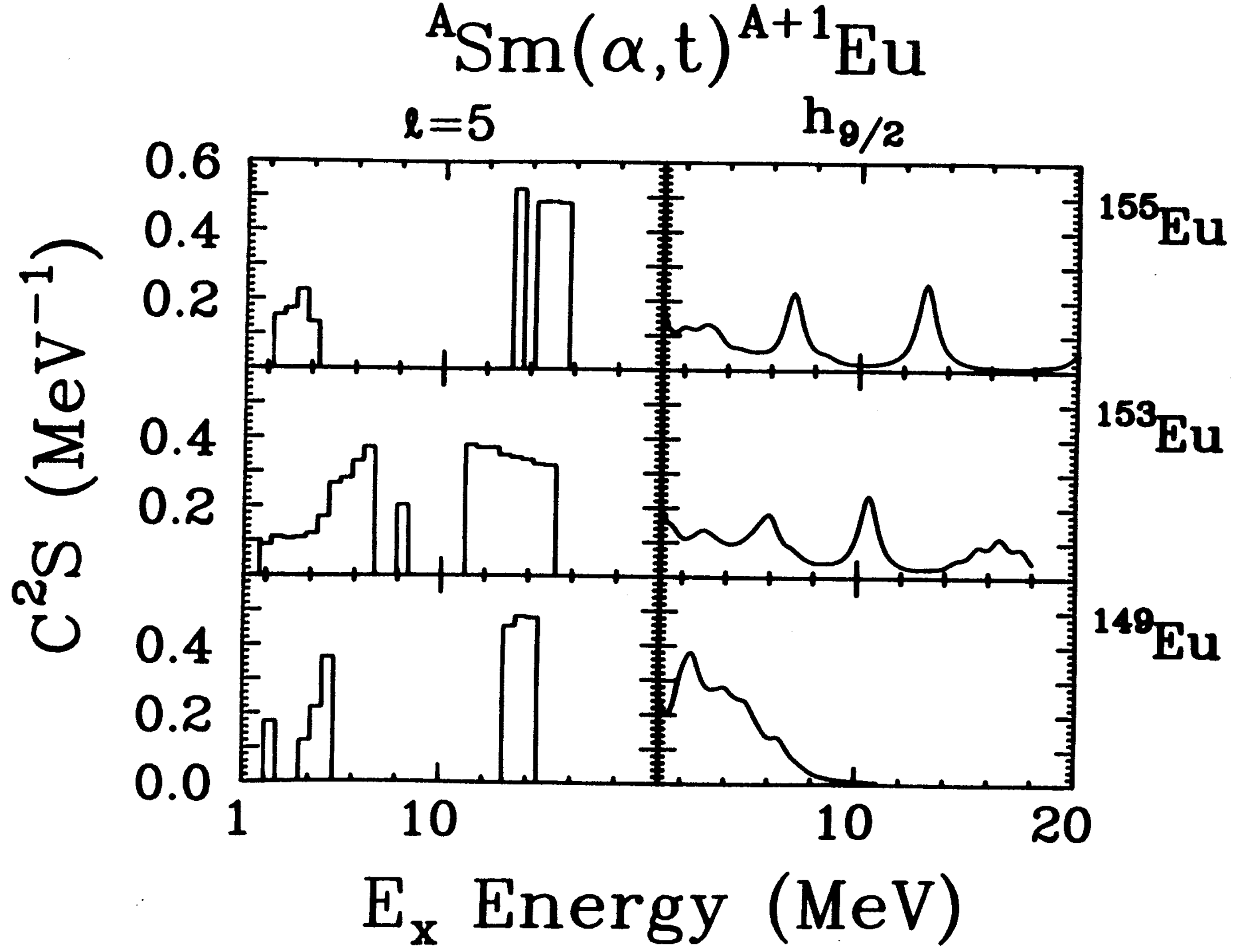
$^{A}Sm(\alpha,t)^{A+1}Eu$
$\ell=5$
$h_{9/2}$
C^2S (MeV^{-1})
0.6
0.4
0.2
0.4
0.2
0.4
0.2
0.0
1
10
10
20
E_x Energy (MeV)
^{155}Eu
^{153}Eu
^{149}Eu

Figure VI.6

constant bombarding energy (100 MeV). We also wanted to reduce the ambiguities of previous analyses. This was accomplished in two ways. First, an attempt was made to calculate the background using the α breakup model instead of by drawing a background by hand, and second, a slicing method was used to obtain the strength distribution without making any assumptions about specific peak shapes.

This concluding discussion is separated into three parts. The first part describes the calculation of the background. The second part discusses the strength found for low-lying peaks using the (α,t) and (α,^{3}He) reactions on ^{144,148,152,154}Sm. The third part presents the results for the systematics of the strength distributions of high-lying single-particle excitations obtained using these reactions.

VI.3.1 The Background

The background calculation was developed to explain the shape and magnitude of the measured spectra at high excitation energies. The calculation included contributions from an elastic α-breakup process and an angle-independent evaporation process. The evaporation process is not totally understood, at least in terms of the Fermi-gas model. The background fitted the shape of the spectra at high excitation energies well (see Figure V.1). With a single normalization for each reaction, the background also reproduced the variations in the magnitude of the high-lying spectra from angle to angle fairly well (within 20%, see Figure V.2). The normalizations used for the background varied from target to target by less than about 20% in the (α,t) reactions and by less than a factor of 2 in the (α,^{3}He) reactions.

VI.3.2 Low-lying Peaks Observed in the (α,t) and (α,^{3}He) Reactions

The (α,t) and (α,^{3}He) reactions were performed on targets of ^{144,148,152,154}Sm and ^{208}Pb. The reactions on ^{208}Pb populated the well-known single-particle levels of ^{209}Bi and ^{209}Pb. Among the Sm targets, the only complete study so far has been for the ^{144}Sm(α,t)^{145}Eu reaction; data for the low-lying levels of ^{149}Eu and ^{145}Sm have also been obtained previously. For all the other cases, strengths are reported here for the first time.

The results obtained with the ^{208}Pb target were used for checking the predictive power of the distorted-wave code DWUCK4 as regards angular distribution shapes and cross section magnitudes. Additionally, since previous work had determined the angular momenta and single-particle strengths (C^2S) for the low-lying levels of ^{145}Eu and since those levels were well resolved in our experiment, our data for these levels were also used for checking the DWUCK4 predictions. In all these cases, which involved individual levels and therefore single ℓ-transfers, the best fit to the angular distribution shape (as determined by the minimum-χ^2_ν procedure) was provided by the correct (single) ℓ-transfer even when the possibility of a mixture of ℓ-values was allowed; see Tables V.1 and V.5. The C^2S values corresponding to the best fits, though somewhat on the low side, agreed with previous determinations within the range of uncertainty of our measured and calculated cross sections.

Generally, however, the reactions on the Sm targets populated (mostly) unresolved collections of low-lying states; this was also invariably the case for the high-lying ($E_x > 2$ MeV) regions. In principle, the fitting program should pick out the correct mixtures of ℓ-transfers for states within a peak. This was tested in two ways.

The first way was to carry out a complete search of χ^2_ν values for each of the low-lying states in ^{209}Bi and ^{145}Eu using a variety of ℓ mixtures. The purpose was to investigate whether other combinations of ℓ-transfers gave acceptable χ^2_ν values relative to the best-fit value. The results, listed in Tables V.2 and V.6, showed that the χ^2_ν value nearest to the minimum χ^2_ν corresponded to a mixture of ℓ-values which included the one identified as the correct ℓ-value by the best fit.

The second way was to sum the measured angular distributions for two states in ^{209}Bi and in ^{209}Pb and then to decompose them using the fitting program. The results (Table V.3) suggested that the selection of an ℓ-transfer made by the fitting procedure was probably only accurate to within ±1. This fact severely limited our ability to determine ℓ-values and, consequently, strength distributions, in regions where different ℓ-transfers overlapped, i.e. over most of the excitation energy range studied. The basic reason for the limitation lay in the similarity of the angular distribution shapes for neighboring ℓ-transfers for $\ell \geq 3$; see Figure III.2. The shapes for $\ell < 3$ were distinctive but, as also shown in Figure III.2, the single-nucleon transfer reactions induced by 100-MeV α particles are not sensitive to low ℓ in the presence of high ℓ. In other words, the kinematic conditions of the experiment restricted us in effect to a study of high-spin single-particle states.

The Nilsson model was used as a guide to select the range of allowed ℓ-transfers for both the low-lying and high-lying states. Due attention was paid to the effect of deformation in bringing down single-particle orbits from the next higher subshell above the proton shell closure at $Z=82$ and the neutron shell closure at $N=126$ into the low-lying regions of the heavier Eu and Sm isotopes, respectively.

In order that the reader can better evaluate the reliability of the ℓ-transfer values obtained by the fitting procedure, the results of single-ℓ transfer fits -- C^2S and χ^2_ν values -- were tabulated for all the low-lying peaks in the Eu and Sm isotopes (Tables V.7 and V.11). These tables are of some use, in that large values of χ^2_ν (say ≥ 20)

associated with a particular ℓ rules out that ℓ-value. But the use is limited, since (as mentioned before) most of the low-lying peaks consist of mixtures of ℓ-values.

There are dramatic differences in the width and position of the low-lying particle states in ^{145,149,153,155}Eu and ^{145,149,153,155}Sm as a function of nuclear deformation; see Figures V.7 and V.16. It is known from earlier investigations that similar effects are seen for hole states.

Mixtures of ℓ-transfers were selected for most of the low-lying peaks in ^{149,153,155}Eu. Notice in Table V.7 that single-ℓ fits to the data with the adjacent ℓ-transfers $\ell=4$ and $\ell=5$ resulted in similar χ^2_ν values. This shows that it was difficult to distinguish between these two ℓ-transfers. The χ^2_ν values listed in Tables V.5 and V.7 for ^{149,153}Eu are all very high (16 to 183), which indicates that ℓ-value selection was difficult for the low-lying peaks in these two nuclei.

We turn now to the low-lying peaks in ^{144,149,153,155}Sm. The Nilsson model allows the $3p_{3/2}$ neutron orbit in all four nuclei. But Table V.11 shows that the largest χ^2_ν values resulted from $\ell=1$ fits. This was because the $\ell=1$ cross section was weak and did not give a good fit to the angular distribution. Of course a weak $\ell=1$ cross section could be mixed in with other ℓ-transfers, but it would be difficult to see because the other ℓ-transfers would have much larger cross sections. Except for the ^{145}Sm low-lying states, Table V.11 shows that the selection of a single ℓ-transfer used to fit the angular distribution of each peak had a χ^2_ν value close that for the neighboring ℓ-transfer. This meant that it was difficult to distinguish between neighboring ℓ-transfers for the low-lying peaks in ^{149,153,155}Sm.

For the low-lying peaks in ^{153}Sm, the best fit (minimum χ^2_ν) was always with $\ell=5$ transfer (Table V.10). The summed $\ell=5$ transition strength was, however, slightly greater than the sum rule limit of unity.

VI.3.3 High-Lying Strength Observed in the (α,t) and $(\alpha,{}^3He)$ Reactions

The high-lying regions in the spectra of the Eu isotopes showed two gross structures, labeled "A" and "B" in Figure V.6a, both of which moved closer to the respective ground states as the deformation increased from ^{145}Eu to ^{155}Eu. A similar behavior was found for the gross structure "A'" present in the spectra of the Sm isotopes (see Figure V.6b). These features, observed for particle states for the first time in the present work, were reminiscent of the behavior previously found for hole states.

While the gross structures "A" and "A'" in the Eu and Sm spectra, respectively, could have been fitted with a gaussian having a centroid that decreased in excitation energy as the deformation increased, it would have been difficult to fit the rest of the spectra accurately with gaussian peaks. For example, the gross structure "B" in the (α,t) data would have been a difficult structure to fit with one gaussian because the structure was flat in ^{145,149,153}Eu. Also, a number of gaussians would have been necessary to fit the region between the gross structures "A" and "B" in the spectra.

Both the number of gaussian peaks used to fit the spectra and the parameters used in the gaussian fitting procedure would have varied among experimenters, making it difficult to draw general conclusions from such fits. Therefore, we used the simple alternative technique of slicing the spectra into intervals of the same width. The technique could easily be used consistently by experimenters. Although the slicing width and starting position in the spectrum are open parameters in this technique, such parameters can be monitored. In our case, the bin width made little difference to the final results. The slicing method may be applied to any stripping reaction for finding single particle strength distributions.

There were certain common features among the extracted strength distributions in the high-lying regions of ^{145,149,153,155}Eu. Such also was the case for the high-lying regions in ^{145,149,153,155}Sm. This is shown in Figure V.12 for the Eu isotopes and in Figure V.21 for the Sm isotopes. These figures display the mixture of ℓ-transfers obtained by the minimum-χ^2_ν procedure. For the Eu isotopes, the χ^2_ν value obtained for each of the sliced regions was less than ten (0.2 to 10) in the region from about 1 to 10 MeV and higher than ten (10 to 30) in the region from 10 to 14 MeV (see Figure V.14). Similarly, for the Sm isotopes, the χ^2_ν values obtained for each of the sliced regions was less than ten (0.1 to 10) in the region from about 2 to 13 MeV, as shown in Figure V.23. We hasten, as before, to point out that it is difficult to separate the ℓ-transfer strengths in overlapping regions and that other combinations of ℓ-transfers gave acceptable fits. Figures V.13 and V.22 may be used to read C^2S value for a single-ℓ fit in any excitation energy region of the spectrum. But these two figures are of limited use, for comparison of the experimental and the built-up theoretical (QPPM) cross-sectional spectra confirmed that a strong overlap exists between the $\ell=3$, 5 and 6 proton strengths in ^{145}Eu (see Figure VI.2) and between the $\ell=3$, 4, 5 and 6 neutron strengths in ^{153,155}Sm (Figure VI.5).

The good agreement shown in Figure VI.2 between the measured and predicted spectra for ^{145}Eu demonstrated the success of the quasi-particle phonon model (QPPM) in predicting strength distributions. The lack of agreement found at high excitation energies for ^{153,155}Eu (Figure VI.2) was ascribed to the neglect of the $1h_{9/2}$ and $1i_{13/2}$ proton strength distributions in the theoretical spectra. Similarly, the excess experimental cross section at $E_x > 3$ MeV in ^{153,155}Sm (Figure VI.5) probably represents the contribution of the $1j_{15/2}$ neutron strength distribution, which was not considered in the theoretical spectra. In view of the neglect of these proton and neutron strength distributions in the theoretical spectra, it was thought that quantitative conclusions about the damping of the strength of individual single-particle excitations would be premature. However, the following qualitative conclusion were drawn.

The high-lying neutron strength in the Sm isotopes comes predominantly from the $2f_{7/2}$ and $1i_{13/2}$ states above the N=82 shell closure and from the $2g_{9/2}$ and $1j_{15/2}$ states above the N=126 shell closure. As seen in Figure V.21, the $2f_{7/2}$ and $2g_{9/2}$ strengths were not observed in all the Sm nuclei. The $1i_{13/2}$ ($\ell=6$) and $1j_{15/2}$ ($\ell=7$) strengths were observed in all four nuclei and appeared to shift lower in excitation energy and to spread out more as the deformation increased.

VI.4 FUTURE DIRECTIONS

More extensive singles measurements of the $(\alpha,{}^3\mathrm{He})$ reaction at high excitation energies are needed to test the α breakup models relevant to neutron-stripping studies. High-lying singles spectra at the larger angles ($\gtrsim 25°$) are also needed to study the angle independent (compound nuclear emission) component of the background mentioned earlier. The breakup models recently developed [Aa84,Me85] may provide insights into additional processes contributing to the background.

Coincidence experiments for obtaining an empirical normalization of the two-body α-breakup spectrum would be of use because such a normalization would reduce the number of parameters put in the background calculation. However, experiments would be difficult using the S320 spectrograph since the solid angle is too small. Instead, a magnet with a large solid angle should be used.

The problem of distinguishing adjacent ℓ-transfers needs to be solved for stripping reactions. One solution perhaps might be to obtain higher quality data than was achieved in the present work over a wide range of angles (2° to 30°). An α-particle beam would be best, since it is the lightest projectile with which both proton and neutron stripping can be studied using the techniques of charged-particle spectroscopy. Work that has been carried out with 183-MeV α-particles [Ga84,Ga85b] does not show any distinguishing difference among adjacent ℓ-transfers. Perhaps some beam energy range can be found which makes it possible to distinguish adjacent ℓ-transfers. Optical model parameters must be determined to test this hypothesis at various beam energies.

A different stripping reaction may be useful for distinguishing adjacent ℓ-transfers. The (d,p) reaction is a possibility for neutron particle states. An advantage of using the (d,p) reaction is that the well-developed deuteron breakup model may be used to calculate the underlying background. In addition, (d,pn) coincidence experiments have been performed on ^{2}H and ^{197}Au at various bombarding energies [Ko85,Se85]. These data would provide an absolute normalization for the background calculation, thereby eliminating the free parameter used in this Thesis.

The experimentally more complicated particle-gamma coincidence technique is an alternative way of obtaining a better determination of ℓ-transfers (as well as j-transfers). Recently such a measurement was made for single-hole states, viz. the ($^{3}He,\alpha\gamma$) reaction was used to measure the $1g_{9/2}^{-1}$ hole state in ^{101}Pd [Sa85]. Again, this requires a large solid angle magnet to detect the charged particles in coincidence with the γ-rays; with the S320 spectrograph, such a measurement would take a prohibitively large amount of time.

APPENDIX I

TABLES OF ANGULAR DISTRIBUTIONS.

This appendix tabulates the extracted cross sections (only three digit accuracy) as a function of angle for the low lying states populated by the reactions $^{144}Sm(\alpha,t)^{145}Eu$ and $^{144}Sm(\alpha,^{3}He)^{145}Sm$ and by the $^{208}Pb(\alpha,t)^{209}Bi$ and $^{208}Pb(\alpha,^{3}He)^{209}Pb$ reactions, for the low lying peaks populated by $^{148,152,154}Sm(\alpha,t)^{149,153,155}Eu$ and $^{148,152,154}Sm(\alpha,^{3}He)^{149,153,155}Sm$ reactions and for the elastic peak populated by the $^{144,148,152,154}Sm(\alpha,\alpha)$ reactions.

Table A.I.1

List of the cross sections for the low-lying states in ^{145}Eu populated by the reaction ^{144}Sm(α,t)^{145}Eu.

E_x - 0.05 MeV

$\theta_{c.m.}$	$\frac{d\sigma}{d\Omega}$ (mb/sr)	uncertainty
2.05432	0.470148E+01	0.258602E+00
3.59502	0.352594E+01	0.131869E+00
5.13566	0.230405E+01	0.831924E-01
7.18969	0.110348E+01	0.386217E-01
9.24349	0.935550E+00	0.347684E-01
12.32361	0.600084E+00	0.248172E-01
15.40284	0.262461E-00	0.140948E-01
18.48097	0.158181E-00	0.102742E-01

E_x - 0.37 MeV

2.05443	0.264404E+01	0.153547E+00
3.59521	0.259201E+01	0.103326E+00
5.13593	0.209470E+01	0.771402E-01
7.19006	0.164280E+01	0.518856E-01
9.24397	0.964934E+00	0.353771E-01
12.32425	0.439845E+00	0.197827E-01
15.40364	0.356590E+00	0.173938E-01
18.48192	0.211891E-00	0.123770E-01

E_x - 0.73 MeV

$\theta_{c.m.}$	$\frac{d\sigma}{d\Omega}$ (mb/sr)	uncertainty
2.05455	0.280936E+02	0.144737E+01
3.59542	0.256860E+02	0.788692E+00
5.13622	0.233134E+02	0.671956E+00
7.19048	0.193962E+02	0.463474E+00
9.24450	0.130336E+02	0.208735E+00
12.32495	0.651299E+01	0.198747E+00
15.40452	0.348939E+01	0.116695E+00
18.48297	0.205492E+01	0.737069E-01

E_x - 1.04 MeV

2.05465	0.754048E+01	0.403082E+00
3.59560	0.596908E+01	0.205248E+00
5.13648	0.362052E+01	0.120773E+00
7.19084	0.201577E+01	0.608402E-01
9.24497	0.165511E+01	0.483837E-01
12.32558	0.113491E+01	0.410143E-01
15.40530	0.563815E+00	0.243352E-01
18.48390	0.296686E+00	0.155120E-01

Table A.I.2

List of the cross sections for the low-lying peaks in ^{149}Eu populated by the reaction ^{148}Sm(α,t)^{149}Eu.

E_x - 0.11 MeV

$\theta_{c.m.}$	$\frac{d\sigma}{d\Omega}$ (mb/sr)	uncertainty
2.05252	0.651218E+01	0.338017E+00
3.07875	0.628119E+01	0.243594E+00
3.59186	0.553659E+01	0.186088E+00
5.13115	0.464783E+01	0.139144E+00
6.15729	0.345409E+01	0.935696E-01
7.18338	0.268948E+01	0.642568E-01
9.23540	0.153806E+01	0.312410E-01
12.31286	0.864493E+00	0.248328E-01
15.38946	0.522259E+00	0.150775E-01
16.92737	0.469517E+00	0.178696E-01
18.46499	0.307155E+00	0.958571E-02
21.53924	0.130530E+00	0.554696E-02
25.63591	0.106578E+00	0.739869E-02

E_x - 0.51 MeV

2.05264	0.262943E+02	0.135801E+01
3.07894	0.235249E+02	0.873718E+00
3.59209	0.252722E+02	0.833368E+00
5.13147	0.224890E+02	0.639111E+00
6.15767	0.159061E+02	0.398493E+00
7.18383	0.171705E+02	0.377226E+00
9.23597	0.976440E+01	0.170972E+00
12.31361	0.509952E+01	0.128647E+00
15.39040	0.300274E+01	0.766622E-01
16.92841	0.209280E+01	0.587565E-01
18.46612	0.168411E+01	0.446377E-01
21.54054	0.776265E+00	0.257981E-01
25.63745	0.479162E+00	0.214445E-01

E_x - 1.07 MeV

2.05282	0.395845E+01	0.206339E+00
3.07921	0.460597E+01	0.182254E+00
3.59240	0.347328E+01	0.118389E+00
5.13191	0.283042E+01	0.880569E-01
6.15821	0.258722E+01	0.722238E-01
7.18445	0.236293E+01	0.571633E-01
9.23677	0.146740E+01	0.300210E-01
12.31468	0.770375E+00	0.224966E-01
15.39172	0.519124E+00	0.149986E-01
16.92986	0.542886E+00	0.198219E-01
18.46770	0.321539E+00	0.995702E-02
21.54238	0.159211E+00	0.647406E-02
25.63961	0.157508E+00	0.951224E-02

E_x - 1.47 MeV

$\theta_{c.m.}$	$\frac{d\sigma}{d\Omega}$ (mb/sr)	uncertainty
2.05295	0.973433E+01	0.504157E+00
3.07941	0.806584E+01	0.308858E+00
3.59263	0.863820E+01	0.287824E+00
5.13224	0.735920E+01	0.215194E-00
6.15860	0.462990E+01	0.122440E-00
7.18491	0.524545E+01	0.119599E+00
9.23735	0.290658E+01	0.546352E-01
12.31545	0.179287E+01	0.476855E-01
15.39269	0.108748E+01	0.291624E-01
16.93091	0.790864E+00	0.262583E-01
18.46884	0.635664E+00	0.180051E-01
21.54371	0.304522E+00	0.110807E-01
25.64118	0.220023E+00	0.119507E-01

E_x - 1.74 MeV

2.05304	0.448473E+01	0.233476E-00
3.07954	0.449617E+01	0.178225E-00
3.59278	0.406253E+01	0.137724E-00
5.13246	0.356801E+01	0.108804E-00
6.15886	0.269020E+01	0.747615E-01
7.18521	0.281288E+01	0.669303E-01
9.23775	0.149377E+01	0.304749E-01
12.31598	0.100483E+01	0.283014E-01
15.39334	0.602803E+00	0.170924E-01
16.93163	0.436537E+00	0.169742E-01
18.46963	0.371606E-00	0.112480E-01
21.54462	0.152689E+00	0.626486E-02
25.64226	0.137021E+00	0.868057E-02

Table A.I.3

List of the cross sections for the low-lying peaks in ^{153}Eu populated by the reaction ^{152}Sm(α,t)^{153}Eu.

E_x - 0.33 MeV

$\theta_{c.m.}$	$\frac{d\sigma}{d\Omega}$ (mb/sr)	uncertainty
2.05076	0.894261E+01	0.470453E+00
3.07612	0.777709E+01	0.333679E+00
3.58879	0.810093E+01	0.297834E+00
5.12676	0.724363E+01	0.218140E+00
6.15202	0.549819E+01	0.208856E+00
7.17724	0.526481E+01	0.228674E+00
9.22752	0.441155E+01	0.107924E+00
12.30238	0.144882E+01	0.520736E-01
15.37641	0.100489E+01	0.272429E-01
16.91306	0.724809E+00	0.230811E-01
18.44942	0.500601E+00	0.232380E-01
21.52118	0.207761E+00	0.613277E-02
25.61462	0.968758E-01	0.327384E-02

E_x - 0.70 MeV

2.05087	0.714199E+01	0.376146E+00
3.07629	0.682093E+01	0.293600E+00
3.58898	0.702889E+01	0.258772E+00
5.12704	0.537686E+01	0.163624E+00
6.15236	0.390307E+01	0.150005E+00
7.17764	0.298260E+01	0.130542E+00
9.22802	0.207984E+01	0.537349E-01
12.30305	0.121587E+01	0.439289E-01
15.37725	0.739249E+00	0.205363E-01
16.91397	0.569048E+00	0.188642E-01
18.45041	0.503077E+00	0.233508E-01
21.52234	0.177907E+00	0.530757E-02
25.61598	0.849553E-01	0.290088E-02

E_x - 1.24 MeV

$\theta_{c.m.}$	$\frac{d\sigma}{d\Omega}$ (mb/sr)	uncertainty
2.05103	0.650357E+01	0.342710E+00
3.07653	0.645866E+01	0.278414E+00
3.58927	0.654404E+01	0.241105E+00
5.12745	0.572333E+01	0.173742E+00
6.15285	0.451412E+01	0.172550E+00
7.17821	0.380572E+01	0.165936E+00
9.22875	0.323694E+01	0.806506E-01
12.30403	0.118550E+01	0.428658E-01
15.37846	0.841667E+00	0.231242E-01
16.91531	0.630282E+00	0.205257E-01
18.45186	0.455890E+00	0.212091E-01
21.52402	0.187885E+00	0.558329E-02
25.61796	0.974114E-01	0.329064E-02

Table A.I.4

List of the cross sections for the low-lying peaks in ^{155}Eu populated by the reaction ^{154}Sm(α,t)^{155}Eu.

E_x - 0.45 MeV

$\Theta_{c.m.}$	$\frac{d\sigma}{d\Omega}$ (mb/sr)	uncertainty
2.04991	0.878851E+01	0.456110E+00
3.07485	0.862911E+01	0.322827E+00
3.58731	0.842555E+01	0.268451E+00
5.12465	0.730640E-01	0.181385E+00
6.14950	0.604501E+01	0.159595E-00
7.17430	0.468832E-01	0.104706E-00
9.22373	0.347069E-01	0.756813E-01
12.29735	0.184127E-01	0.487455E-01
15.37016	0.125839E-01	0.317132E-01
16.90619	0.808307E-00	0.249131E-01
18.44195	0.580266E-00	0.157488E-01
21.51252	0.369121E-00	0.943611E-02
25.60440	0.178348E-00	0.758179E-02

E_x - 1.07 MeV

2.05010	0.721061E+01	0.374735E+00
3.07513	0.640937E-01	0.243225E+00
3.58763	0.662321E+01	0.211547E+00
5.12511	0.501571E+01	0.125550E+00
6.15004	0.415679E+01	0.116362E+00
7.17494	0.312811E+01	0.710726E-01
9.22455	0.233677E+01	0.524391E-01
12.29844	0.137189E+01	0.372813E-01
15.37151	0.939444E-00	0.248478E-01
16.90768	0.600797E-00	0.194993E-01
18.44357	0.526231E-00	0.144332E-01
21.51440	0.326253E-00	0.848949E-02
25.60662	0.150752E-00	0.645177E-02

E_x - 1.41 MeV

$\Theta_{c.m.}$	$\frac{d\sigma}{d\Omega}$ (mb/sr)	uncertainty
2.05020	0.100916E+02	0.523312E+00
3.07528	0.921399E+01	0.343787E+00
3.58781	0.963287E+01	0.306568E+00
5.12537	0.877497E+01	0.217177E+00
6.15035	0.698796E+01	0.181046E+00
7.17530	0.531314E+01	0.118170E-00
9.22502	0.342552E+01	0.747562E-01
12.29906	0.213073E+01	0.558008E-01
15.37228	0.126068E+01	0.317620E-01
16.90852	0.868165E+00	0.264640E-01
18.44448	0.637856E+00	0.171479E-01
21.51546	0.347524E+00	0.895984E-02
25.60787	0.179300E+00	0.762071E-02

Table A.I.5

List of the cross sections for the low-lying states in ^{145}Sm populated by the reaction ^{144}Sm(α, ^{3}He)^{145}Sm.

E_x - 0.00 MeV

$\Theta_{c.m.}$	$\frac{d\sigma}{d\Omega}$ (mb/sr)	uncertainty
2.05344	0.939480E+01	0.751903E+00
3.59348	0.719563E+01	0.555554E+00
5.13345	0.512893E+01	0.295486E+00
7.18660	0.237828E-01	0.638608E-01
9.23953	0.191915E-01	0.126708E+00
12.31835	0.130518E+01	0.868737E-01
15.39629	0.882477E+00	0.540684E-01
18.47315	0.577231E+00	0.324501E-01

E_x - 0.89 MeV

$\Theta_{c.m.}$	$\frac{d\sigma}{d\Omega}$ (mb/sr)	uncertainty
2.05372	0.189436E+02	0.129772E+01
3.59397	0.170768E-02	0.989287E+00
5.13416	0.160285E+02	0.628087E+00
7.18760	0.109832E+02	0.207133E+00
9.24080	0.834121E+01	0.310536E+00
12.32004	0.418045E+01	0.197802E+00
15.39840	0.216962E+01	0.960604E-01
18.47567	0.121522E+01	0.511432E-01

E_x - 1.00 MeV

$\Theta_{c.m.}$	$\frac{d\sigma}{d\Omega}$ (mb/sr)	uncertainty
2.05376	0.138172E+02	0.100732E+01
3.59404	0.114381E+02	0.749150E+00
5.13425	0.982404E+01	0.446523E+00
7.18772	0.618782E+01	0.128891E+00
9.24096	0.420009E+01	0.199708E+00
12.32025	0.203198E+01	0.116517E+00
15.39867	0.143926E+01	0.731623E-01
18.47598	0.899175E+00	0.423024E-01

E_x - 1.11 MeV

$\Theta_{c.m.}$	$\frac{d\sigma}{d\Omega}$ (mb/sr)	uncertainty
2.05379	0.107287E+02	0.829643E+00
3.59409	0.897526E+01	0.638960E+00
5.13433	0.655364E+01	0.343696E+00
7.18784	0.414948E+01	0.947993E-01
9.24111	0.321478E+01	0.170146E-00
12.32045	0.192388E+01	0.112275E-00
15.39891	0.105009E+01	0.600472E-01
18.47627	0.636578E+00	0.343630E-01

E_x - 1.42 MeV

$\Theta_{c.m.}$	$\frac{d\sigma}{d\Omega}$ (mb/sr)	uncertainty
2.05389	0.121919E+02	0.914235E-00
3.59427	0.110802E+02	0.733500E-00
5.13459	0.963437E+01	0.440678E-00
7.18819	0.662165E+01	0.136048E-00
9.24157	0.420695E+01	0.199904E-00
12.32106	0.233502E+01	0.128426E-00
15.39967	0.144441E+01	0.733129E-01
18.47718	0.818162E+00	0.399159E-01

Table A.I.6

List of the cross sections for the low-lying peaks in ^{149}Sm populated by the reaction ^{148}Sm(α,^{3}He)^{149}Sm.

E_x - 0.00 MeV

$\theta_{c.m.}$	$\frac{d\sigma}{d\Omega}$ (mb/sr)	uncertainty
3.07837	0.304937E+01	0.139831E+00
4.10445	0.295463E+01	0.104205E+00
5.13051	0.205349E+01	0.567599E-01
6.15652	0.160240E+01	0.401571E-01
7.18249	0.122699E+01	0.251332E-01
9.23425	0.962351E+00	0.250925E-01
12.31133	0.738937E+00	0.223527E-01
15.38755	0.458526E+00	0.190197E-01
18.46271	0.288550E+00	0.921225E-02
21.53660	0.172466E+00	0.685365E-02
25.63280	0.994559E-01	0.614317E-02

E_x - 0.29 MeV

$\theta_{c.m.}$	$\frac{d\sigma}{d\Omega}$ (mb/sr)	uncertainty
3.07851	0.771535E+01	0.343666E+00
4.10464	0.689284E+01	0.220492E+00
5.13074	0.582115E+01	0.148194E+00
6.15680	0.527021E+01	0.116099E+00
7.18281	0.461506E+01	0.771941E-01
9.23466	0.275270E+01	0.593349E-01
12.31187	0.147807E+01	0.388847E-01
15.38823	0.933753E+00	0.355167E-01
18.46353	0.611460E+00	0.159719E-01
21.53755	0.325350E+00	0.105230E-01
25.63391	0.138227E+00	0.797651E-02

E_x - 0.91 MeV

$\theta_{c.m.}$	$\frac{d\sigma}{d\Omega}$ (mb/sr)	uncertainty
3.07880	0.157584E+02	0.696216E+00
4.10502	0.159061E+02	0.490852E+00
5.13122	0.132043E+02	0.326861E+00
6.15737	0.128535E+02	0.272212E+00
7.18348	0.111060E+02	0.175669E+00
9.23552	0.735881E+01	0.145737E+00
12.31302	0.409798E+01	0.960621E-01
15.38966	0.210229E+01	0.757945E-01
18.46523	0.139435E+01	0.315868E-01
21.53953	0.809128E+00	0.212027E-01
25.63624	0.345337E+00	0.175460E-01

E_x - 1.41 MeV

$\theta_{c.m.}$	$\frac{d\sigma}{d\Omega}$ (mb/sr)	uncertainty
3.07904	0.673537E+01	0.300808E+00
4.10534	0.658091E+01	0.211592E+00
5.13162	0.546945E+01	0.139674E+00
6.15786	0.504499E+01	0.111456E+00
7.18404	0.435591E+01	0.732492E-01
9.23624	0.303069E+01	0.645750E-01
12.31398	0.144858E+01	0.382292E-01
15.39086	0.100251E+01	0.378902E-01
18.46666	0.686679E+00	0.174953E-01
21.54118	0.432749E+00	0.129590E-01
25.63820	0.176435E+00	0.975904E-02

E_x - 1.89 MeV

$\theta_{c.m.}$	$\frac{d\sigma}{d\Omega}$ (mb/sr)	uncertainty
3.07926	0.838529E+01	0.372955E+00
4.10565	0.880092E+01	0.277789E+00
5.13200	0.640398E+01	0.162305E+00
6.15831	0.611353E+01	0.133476E+00
7.18458	0.527801E+01	0.872711E-01
9.23693	0.355684E+01	0.744764E-01
12.31489	0.245601E+01	0.603198E-01
15.39198	0.108228E+01	0.406448E-01
18.46801	0.928072E+00	0.223410E-01
21.54274	0.493468E+00	0.143116E-01
25.64004	0.310270E+00	0.159356E-01

Table A.I.7

List of the cross sections for the low-lying peaks in ^{153}Sm populated by the reaction ^{152}Sm(α, ^{3}He)^{153}Sm.

$\theta_{c.m.}$	$\frac{d\sigma}{d\Omega}$ (mb/sr)	uncertainty
2.05090	0.102416E+02	0.603276E+00
3.07633	0.906122E+01	0.353168E+00
4.10173	0.837699E+01	0.260131E+00
5.12711	0.716956E+01	0.171091E+00
6.15244	0.620620E+01	0.163870E+00
7.17773	0.568266E+01	0.921182E-01
9.22814	0.346987E+01	0.105411E+00
11.27827	0.208079E+01	0.107703E+00
12.30321	0.182154E+01	0.668241E-01
15.37745	0.110091E+01	0.252345E-01
18.45065	0.619886E+00	0.246741E-01
21.52262	0.381175E+00	0.144080E-01
25.61631	0.161765E+00	0.662771E-02

E_x - 0.45 MeV

2.05102	0.411368E+01	0.246682E+00
3.07652	0.379997E+01	0.151881E+00
4.10199	0.286039E+01	0.943779E-01
5.12743	0.247113E+01	0.617667E-01
6.15283	0.211915E+01	0.609665E-01
7.17818	0.162408E+01	0.328511E-01
9.22872	0.116698E+01	0.386486E-01
11.27897	0.843666E+00	0.456048E-01
12.30398	0.572050E+00	0.226034E-01
15.37840	0.417812E+00	0.111654E-01
18.45179	0.269727E-00	0.113302E-01
21.52394	0.122151E+00	0.528947E-02
25.61786	0.589206E-01	0.277160E-02

$\theta_{c.m.}$	$\frac{d\sigma}{d\Omega}$ (mb/sr)	uncertainty
2.05118	0.524617E+01	0.312600E+00
3.07675	0.442340E+01	0.175740E+00
4.10229	0.394002E+01	0.126873E+00
5.12781	0.352769E+01	0.863754E-01
6.15329	0.306446E+01	0.848458E-01
7.17872	0.277617E+01	0.499764E-01
9.22940	0.168294E+01	0.536560E-01
11.27981	0.110909E+01	0.589410E-01
12.30489	0.948005E+00	0.359322E-01
15.37954	0.592376E+00	0.148037E-01
18.45315	0.316916E+00	0.131326E-01
21.52551	0.183802E+00	0.747640E-02
25.61972	0.815561E-01	0.362890E-02

E_x - 1.74 MeV

2.05142	0.935525E+01	0.551697E+00
3.07712	0.757184E+01	0.296194E+00
4.10279	0.746458E+01	0.232738E+00
5.12843	0.630210E+01	0.150917E-00
6.15402	0.528617E+01	0.140748E+00
7.17958	0.525925E+01	0.860097E-01
9.23051	0.295760E+01	0.905865E-01
11.28116	0.213594E+01	0.110465E-00
12.30636	0.171028E+01	0.628907E-01
15.38137	0.106771E+01	0.245561E-01
18.45533	0.668691E+00	0.265309E-01
21.52804	0.393980E+00	0.148564E-01
25.62271	0.166148E+00	0.679007E-02

Table A.I.8

List of the cross sections for the low-lying peaks in ^{155}Sm populated by the reaction ^{154}Sm(α, ^{3}He)^{155}Sm.

E_x - 0.36 MeV

$\Theta_{c.m.}$	$\frac{d\sigma}{d\Omega}$ (mb/sr)	uncertainty
3.07551	0.771134E+01	0.347681E+00
4.10064	0.667058E+01	0.177138E+00
5.12574	0.649644E+01	0.214996E+00
6.15081	0.583522E+01	0.130668E+00
7.17583	0.510746E+01	0.845865E-01
9.22570	0.365490E+01	0.972652E-01
12.29996	0.201858E+01	0.626209E-01
15.37341	0.120922E+01	0.421131E-01
18.44583	0.679156E+00	0.324934E-01
21.51702	0.371953E+00	0.269670E-01
25.60971	0.192716E+00	0.140096E-01

E_x - 0.95 MeV

3.07578	0.231876E+01	0.108349E+00
4.10100	0.193076E+01	0.555597E-01
5.12619	0.200459E+01	0.746850E-01
6.15134	0.181063E+01	0.541649E-01
7.17645	0.145301E+01	0.341452E-01
9.22650	0.118588E+01	0.374534E-01
12.30103	0.667097E+00	0.273141E-01
15.37473	0.372722E+00	0.199639E-01
18.44741	0.296577E+00	0.201062E-01
21.51886	0.161370E+00	0.133826E-01
25.61187	0.781403E-01	0.878584E-02

E_x - 1.71 MeV

$\Theta_{c.m.}$	$\frac{d\sigma}{d\Omega}$ (mb/sr)	uncertainty
3.07612	0.584248E+01	0.264486E+00
4.10146	0.515489E+01	0.138091E+00
5.12677	0.462919E+01	0.155858E+00
6.15204	0.464910E+01	0.107445E+00
7.17726	0.413011E+01	0.718262E-01
9.22754	0.266693E+01	0.728351E-01
12.30241	0.159069E+01	0.503897E-01
15.37645	0.966828E+00	0.351621E-01
18.44946	0.622419E+00	0.294727E-01
21.52124	0.338964E+00	0.244812E-01
25.61468	0.175894E+00	0.125730E-01

Table A.I.9

List of the cross sections for the elastic peak in the reactions $^{144,148,152,154}Sm(\alpha,\alpha)$.

Reaction : 144Sm(α, α)

$\Theta_{c.m.}$	$\frac{d\sigma}{d\Omega}$ (mb/sr)	uncertainty
2.05707	0.272708E+08	0.169513E+07
4.11406	0.137620E+07	0.207894E+05
6.17092	0.271450E+06	0.610790E+04

Reaction : 148Sm(α, α)

$\Theta_{c.m.}$	$\frac{d\sigma}{d\Omega}$ (mb/sr)	uncertainty
2.05552	0.319341E+08	0.282188E+06
4.11098	0.135084E+07	0.418867E+04
6.16629	0.431172E+06	0.296169E+04

Reaction : 152Sm(α, α)

$\Theta_{c.m.}$	$\frac{d\sigma}{d\Omega}$ (mb/sr)	uncertainty
2.05406	0.203998E+08	0.198348E+06
4.10805	0.284057E+07	0.127948E+05
6.16191	0.285452E+06	0.143480E+04

Reaction : 154Sm(α, α)

$\Theta_{c.m.}$	$\frac{d\sigma}{d\Omega}$ (mb/sr)	uncertainty
2.05336	0.285417E+08	0.270197E+07
4.10665	0.122332E+07	0.650193E+04
6.15981	0.323035E+06	0.160465E+04

Table A.I.10

List of the cross sections for the low-lying states in ^{209}Pb and ^{209}Bi populated by the ^{208}Pb(α, ^{3}He)^{209}Pb and ^{208}Pb(α,t)^{209}Bi reactions, respectively.

Reaction : ^{208}Pb(α, t)

E_x - 0.00 MeV

$\theta_{c.m.}$	$\frac{d\sigma}{d\Omega}$ (mb/sr)	uncertainty
2.03747	0.906507E+01	0.181519E+00
3.56555	0.874680E+01	0.209569E+00
5.09358	0.765519E+01	0.156860E+00
7.13086	0.686824E+01	0.155441E+00
9.16797	0.469830E+01	0.885019E-01
12.22324	0.214018E+01	0.741515E-01
15.27791	0.137032E+01	0.414727E-01
18.33181	0.863112E+00	0.266657E-01
20.36724	0.527128E+00	0.478893E-01

E_x - 0.90 MeV

$\theta_{c.m.}$	$\frac{d\sigma}{d\Omega}$ (mb/sr)	uncertainty
2.03768	0.122483E+02	0.218416E+00
3.56591	0.110324E+02	0.241578E+00
5.09409	0.842806E+01	0.168898E+00
7.13157	0.521543E+01	0.140698E+00
9.16889	0.302007E+01	0.749293E-01
12.22446	0.210666E+01	0.758019E-01
15.27941	0.108635E+01	0.382627E-01
18.33361	0.819410E+00	0.270161E-01
20.36923	0.491660E+00	0.469279E-01

E_x - 1.61 MeV

$\theta_{c.m.}$	$\frac{d\sigma}{d\Omega}$ (mb/sr)	uncertainty
2.03784	0.134244E+02	0.224974E+00
3.56619	0.142552E+02	0.270951E+00
5.09450	0.132588E+02	0.208024E+00
7.13214	0.117184E+02	0.204410E+00
9.16962	0.843299E+01	0.120002E+00
12.22543	0.447249E+01	0.108073E+00
15.28063	0.263663E+01	0.581577E-01
18.33506	0.171847E+01	0.379896E-01
20.37084	0.103754E+01	0.686065E-01

Reaction : ^{208}Pb(α, ^{3}He)

E_x - 0.00 MeV

$\theta_{c.m.}$	$\frac{d\sigma}{d\Omega}$ (mb/sr)	uncertainty
2.03761	0.437398E+01	0.257293E+00
3.05640	0.409202E+01	0.192871E+00
3.56579	0.391446E+01	0.134733E+00
5.09392	0.302042E+01	0.989002E-01
7.13133	0.229459E+01	0.279253E-01
9.16858	0.179242E+01	0.290914E-01
12.22404	0.164479E+01	0.274330E-01
15.27890	0.118602E+01	0.244193E-01
18.33299	0.931106E+00	0.251094E-01

E_x - 0.78 MeV

$\theta_{c.m.}$	$\frac{d\sigma}{d\Omega}$ (mb/sr)	uncertainty
2.03779	0.861024E+01	0.360904E+00
3.05667	0.903724E+01	0.286664E+00
3.56610	0.856022E+01	0.199259E+00
5.09437	0.695903E+01	0.150088E+00
7.13195	0.573258E+01	0.441371E-01
9.16938	0.399448E+01	0.434242E-01
12.22511	0.257312E+01	0.343083E-01
15.28023	0.179205E+01	0.300150E-01
18.33458	0.111714E+01	0.275020E-01

E_x - 1.42 MeV

$\theta_{c.m.}$	$\frac{d\sigma}{d\Omega}$ (mb/sr)	uncertainty
2.03794	0.138137E+02	0.457229E+00
3.05689	0.151901E+02	0.371618E+00
3.56636	0.147765E+02	0.261730E+00
5.09474	0.129063E+02	0.204371E+00
7.13247	0.117656E+02	0.632263E-01
9.17005	0.909001E+01	0.655045E-01
12.22600	0.575702E+01	0.513133E-01
15.28134	0.379570E+01	0.436767E-01
18.33590	0.228203E+01	0.393043E-01

APPENDIX II

PROGRAM ALGORITHMS and PROGRAM INPUT EXAMPLES.

The codes developed in this thesis were carried out for use on the VAX 11/750 and VAX 11/780 computers at the NSCL. All input data for programs and output data from programs were written to the disk of the VAX computer in the file format.

This appendix is separated into six sections. In the first section the program, SPECCAL is outlined in an algorithm format and a program input and output is also presented. The second section outlines in an algorithm format the program SMASHER and a program input and output is presented here. The third section gives and example of the data files needed to run the DWBA program DWUCK4 [Ku84]. The fourth section gives an example input and output of the data files needed to run the cross section code SIGCALC [St82]. In the fifth section, an example input and output is displayed to use the program WRITECHEX, which converts a spectrum which is expressed in terms of counts versus channel number to a spectrum expressed in terms of counts versus excitation energy. In the last section, an example input that was used to setup the 68K data aquisition program, used to collect data in the third experimental run.

A. CALIBRATION PROGRAM.

The calibration procedure is outlined in Chapter II. The program developed to calculate a set of calibrations for each reaction is called SPECCAL. As mentioned in Chapter II, the program fits a quadratic curve through a set of energy calibration points given by the mylar target and low lying states in the reaction of interest, if any exist. The algorithm of the program SPECCAL is given in Figure A.II.1.

The input data file required to run the program SPECCAL is presented here as a case of 96.9 MeV α particles bombarding mylar and ^{144}Sm. In this case, the input and output files obtain a calibration equation for the ^{145}Eu spectra at a laboratory angle of 2° and target angle of 2° for all spectra angles will be given. There are eight calibrated peaks positions corresponding to those in Figure II.8. The input and output sample files for this case is given in Tables A.II.1a and A.II.1b respectively.

Figure A.II.1

Calibration program algorithm

Program SPECCAL

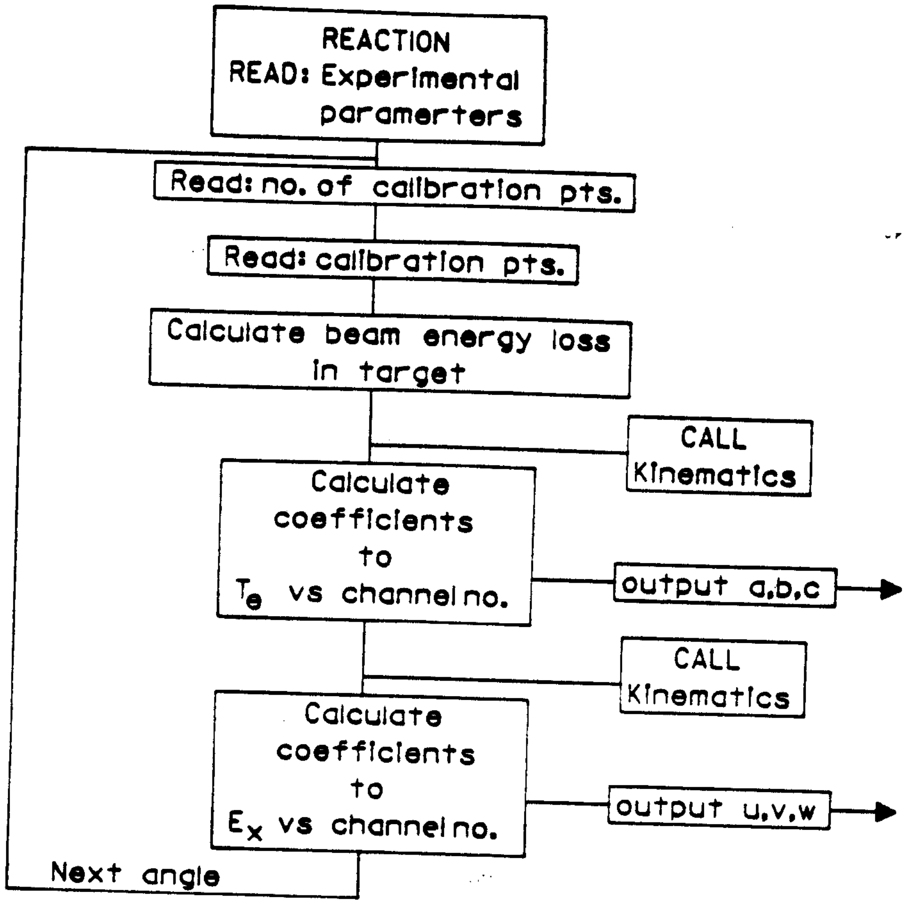

Figure A.II.1

Table A.II.1a

Calibration program input example.

```
Y
CHEXASMT
ASMATB
40
Y
Y
Y
144SM(4HE,T)
1.05                                          ← target thickness in mg/cm2
96.9                                          ← beam energy in MeV
Y
200.,900.
2                                             ← order of the polynomial fit.
8                                             ← number of calibration points.
1
252.009,0.066,2.,2.,1.046,0.,144SM            ← calibration information: chann.# etc.
261.153,0.128,2.,2.,1.046,0.3295,144SM
271.443,0.022,2.,2.,1.046,0.716,144SM
280.475,0.057,2.,2.,1.046,1.0419,144SM
329.810,0.019,2.,2.,0.88,0.,12C
360.510,0.016,2.,2.,0.88,0.,16O
449.293,0.012,2.,2.,0.88,3.547,12C
563.173,0.086,2.,2.,0.88,5.817,16O
2.,2.                                         ← Lab Θ, target Θ
252.009
261.153
271.443
280.475
329.810
360.510
449.293
563.173
640.880
722.009
735.538
0.
N
Y
77.,59.
N
N
(EOB)
```

Table A.II.1b

Calibration program output example.

```
    Fitting done with Pe vs Channel #
144SM(4HE,T)
 Pe=
 0.35171192E-04 x** 2 +
 -.16850402E+00 x** 1 +
 0.71584653E+03
 Te=
 0.10822408E-04 x** 2 +
 -.40519277E-01 x** 1 +
 0.89624286E+02
 X**2=0.13036918E+01 Abs error=0.11737251E-01 Rel error=0.15414309E-03
 Ex=
 -.11392478E-04 x** 2 +
 0.40756231E-01 x** 1 +
 -.94841775E+01
 Lab     C.M.      Te        Qval      Ex       Tp         DTp       Ch #         Reaction
angle   angle    [MeV]     [MeV]    [MeV]    [MeV]      [MeV]
 2.000   2.054    80.1718  -16.559   0.000   96.8587    0.0250   252.01 144SM(4HE,T)
                                                         rho delX =    1.046 mg/cm**2
 2.000   2.055    79.8404  -16.559   0.330   96.8587    0.0250   261.15 144SM(4HE,T)
                                                         rho delX =    1.046 mg/cm**2
 2.000   2.055    79.4517  -16.559   0.716   96.8587    0.0250   271.44 144SM(4HE,T)
                                                         rho delX =    1.046 mg/cm**2
 2.000   2.055    79.1238  -16.559   1.042   96.8587    0.0250   280.48 144SM(4HE,T)
                                                         rho delX =    1.046 mg/cm**2
 2.000   2.654    77.4336  -17.871   0.000   96.8483    0.0354   329.81 12C(4HE,T)
                                                         rho delX =    0.880 mg/cm**2
 2.000   2.497    76.3981  -19.214   0.000   96.8497    0.0340   360.51 16O(4HE,T)
                                                         rho delX =    0.880 mg/cm**2
 2.000   2.676    73.6106  -17.871   3.547   96.8483    0.0354   449.29 12C(4HE,T)
                                                         rho delX =    0.880 mg/cm**2
 2.000   2.523    70.2173  -19.214   5.817   96.8497    0.0340   563.17 16O(4HE,T)
                                                         rho delX =    0.880 mg/cm**2
.........................................................................................

                                                         rho delX =    1.046 mg/cm**2
 2.000   0.000    80.1004  -16.559   0.063   96.8587    0.0250   252.01 144SM(4HE,T)
 2.000   0.000    79.7807  -16.559   0.383   96.8587    0.0250   261.15 144SM(4HE,T)
 2.000   0.000    79.4230  -16.559   0.740   96.8587    0.0250   271.44 144SM(4HE,T)
 2.000   0.000    79.1110  -16.559   1.051   96.8587    0.0250   280.48 144SM(4HE,T)
 2.000   0.000    77.4378  -16.559   2.719   96.8587    0.0250   329.81 144SM(4HE,T)
 2.000   0.000    76.4232  -16.559   3.728   96.8587    0.0250   360.51 144SM(4HE,T)
 2.000   0.000    73.6039  -16.559   6.526   96.8587    0.0250   449.29 144SM(4HE,T)
 2.000   0.000    70.2374  -16.559   9.862   96.8587    0.0250   563.17 144SM(4HE,T)
 2.000   0.000    68.1013  -16.559  11.982   96.8587    0.0250   640.88 144SM(4HE,T)
 2.000   0.000    66.0107  -16.559  14.064   96.8587    0.0250   722.01 144SM(4HE,T)
 2.000   0.000    65.6759  -16.559  14.399   96.8587    0.0250   735.54 144SM(4HE,T)
 2.000   0.000    81.9533  -16.559  -1.800   96.8587    0.0250   200.00 144SM(4HE,T)
 2.000   0.000    61.9231  -16.559  17.960   96.8587    0.0250   300.00 144SM(4HE,T)
```

B. FITTING and SLICING PROGRAMS.

Chapter IV made reference to a slicing and fitting of DWBA ℓ-transfers using the χ^2_ν method. The program that performs these operations is called SMASHER. The algorithm of SMASHER is given in Figure A.II.2.

The program SMASHER was designed to calculate the spectroscopic factors (C^2S) by means of fitting a set of ℓ-transfer angular distributions calculated by DWUCK4 with the experimentally deduced angular distributions. The experimental angular distributions were calculated by either a slicing method or by gaussians.

The input example that its given here will use the typical case of slicing the ^{145}Sm spectra using the ^{144}Sm(α, ^{3}He) reaction. The slicing of 520 keV bin widths begins at 1.7 MeV and is concluded at about 14 MeV. The DWBA ℓ-transfers that were selected to fit this excitation energy region are the ℓ=3, 4, 5, 6 and 7 values. The input data file for this case is given in Table A.II.2 and is called ASMAHBF.DAT. To run the SMASHER program interactively one would type in:

```
ANALYS:: @SMASHER1 <cr>
```

The program then asks (with your response underlined):

```
What is the name of the *.DAT file to be run by SMASHER?

                                                  ASMAHBF <cr>
```

The output of the program write a set of output files of the calculation which contain the information from all of the fits and of the background calculation.

Figure A.II.2

Program algorithm for SMASHER.

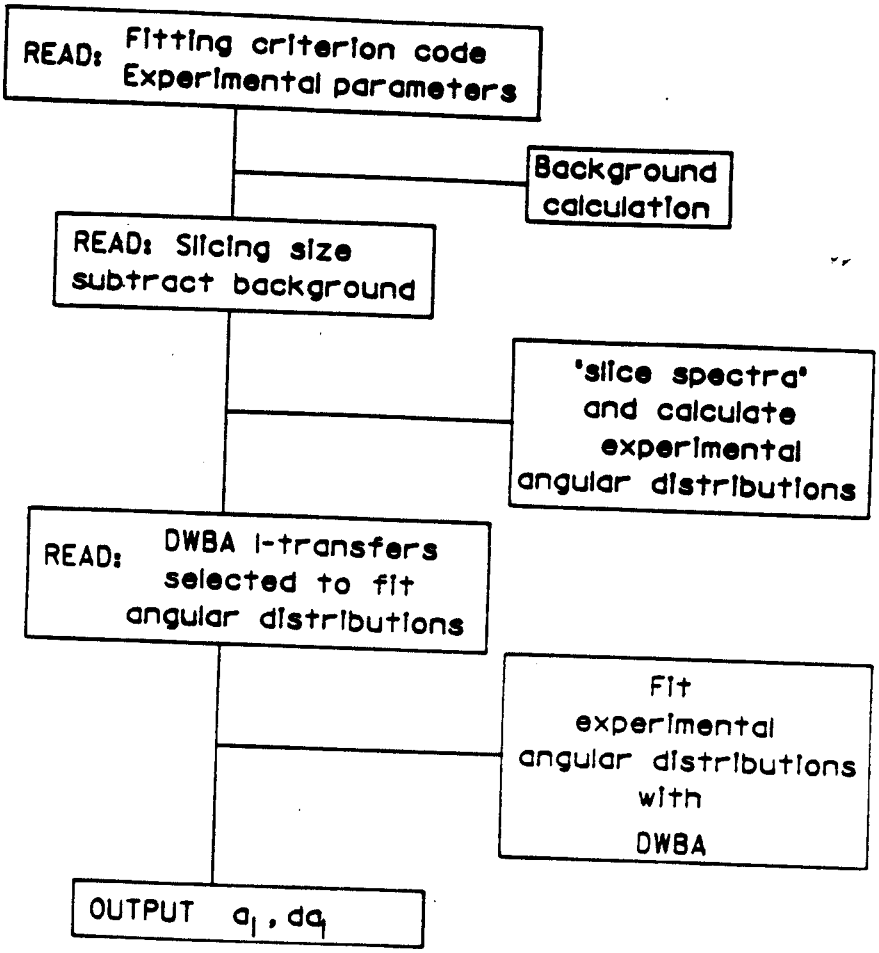

Program SMASHER

Figure A.II.2

Table A.II.2

Slicing and fitting program example

```
1
Y                                  ← turn on χ² fitting.
F
E
8                                  ← number of angles
[DUFFY.ALPHAHC.DATA]
ASMAHB                             ← spectra file name code
2.,2.                              ← lab Θ, target Θ
1.0
95.9415,15.77                      ← charge (μC), relative error (μC)
3.5,2.
1.0
144.8717,8.74
5.,2.
1.0
201.2146,5.35
7.,2.
1.0
354.1145,5.66
9.,2.
1.0
417.3974,50.95
12.,2.
1.0
344.9875,13.48
15.,2.
1.0
477.8960,24.08
18.,2.
1.0
571.2793,40.94
144SM(4HE,3HE)
96.9                               ← beam energy
1.05
.9647
0
1.6
 4                                 ← turn on α-breakup
7                                  ← turn on  - evaporation
0.99
5.,15.5
1
2
5.53,151.
7.,29.4                            ← match calculation at Ex=29 MeV
.185,.8
0
1.7                                ← start slicing at 1.7 MeV
520.                               ←
.17
2
5                                  ← number of DWBA l-transfers
3                                  ← l=3
4                                  ← l=4
5                                  ← l=5
6                                  ← l=6
7                                  ← l=7
ASMAHB
Y
[EOB]
```

C. DWBA PROGRAMS.

DWBA programs are made easy to run on the Vax 11/750 and 11/780 computers. The DWBA calculations needed for this thesis involve many cases of ℓ-transfers (ℓ = 0 → 7) and a long range of excitation energies (E_x= 0 → 15 MeV) for one reaction (see Chapter III). Setting up the data file for the DWUCK4 [Ku84] program involving many cases for one reaction and is very time consuming if this work was to be carried out by hand. This gave rise to the development of a program, called DWKREACT, that would make the setting up of the input data file for the DWUCK4 program very easy for the many cases involved. Hence, the DWBA inelastic calculations where performed using two different programs. The first program, called DWKREACT, would set up the input data file for the second program called DWUCK4. No algorithm of the DWKREACT is necessary because all it does is write to disk, in the format form, an input file for the DWUCK4 program. The typical case of an input file for DWKREACT is given in TABLE A.II.3. This is a typical case to calculate the $1h_{9/2}$, $1i_{11/2}$ and $1j_{15/2}$ at the excitation energies of 0.0 and 5.0 MeV using the optical parameters given in Table III.1.

Table A.II.3

DWBA program example

```
144Sm(4He,3He)145Sm  Woods-Saxon      42
100.      deepneut225.00000.0000
  0.      30.         0. 25    1.  -1.
C 1    2    3    4    5    6
 -1.   0.  -1.   0.  -1.   0.    1.4      1.4      0.0
-158.4      1.32      0.62      0.        -30.02      1.35      0.85
-125.4      1.18      0.86      0.        -17.2       1.55      0.77
  -1.       1.25      0.65      25.         0.        0.        0.
 3
 0 5 9 0 1 1
 0 613 0 1 1
 0 715 0 1 1
 2
  0.0
  5.0
-1
|EOB|
```

D. PROGRAM EXAMPLE FOR SIGCALC.

The program SIGCALC has been used throughout the NSCL to calculate cross sections using the experimental parameters and extracted peaks. The typical example that will be given here, is, the examination of three low lying peaks in ^{145}Sm obtained by the inelastic reaction of ^{144}Sm(α,^{3}He) with an α beam energy of 96.8 MeV. In particular, the three low lying peaks energies are; 0.0 MeV, 0.88 MeV and 1.17 MeV and cross sections are computed for eight angles that range from 2° to 18°. The name of the input file is ASMAHB3AC.DAT and is tabulated in Table A.II.4a.

SIGCALC is an interactive program in which one must input data file and type in what form the output must be in. Table A.II.4b tabulate the procedure to obtain lab cross sections by running the program on the VAX computer.

Table A.II.4a

SIGCALC program input example.

```
144SM(4HE,3HE)
 1          0.000
 2          0.882
 3          1.167
.  100.000       1.000      0.415      2.000
TARGET        .9647
   3        2.000       2.000  233.7312    1.00000    1.28000
   5        3.500       2.000  208.7160    1.00000    1.00000
   6        5.000       2.000  247.6758    1.00000    1.00000
   8        7.000       2.000  338.2842    1.00000    1.00000
  10        9.000       2.000  426.6666    1.00000    1.00000
  13       12.000       2.000  596.8626    1.00000    1.00000
  16       15.000       2.000  807.0090    1.00000    1.00000
  19       18.000       2.000 1023.1062    1.00000    1.00000
END
   195.80            1992.52          51.48             3       2
   220.92           13190.36         199.85             3       2
   229.09            4959.36         249.71             3       2
    -1.0                0.0            0.0              0       0
   200.62            3541.72          66.09             5       3
   224.38           13794.15         266.26             5       3
   232.12            9977.50         482.31             5       3
    -1.0                0.0            0.0              0       0
   200.39            2803.19          62.72             6       5
   224.18           12965.64         197.56             6       5
   231.70           19175.50         352.98             6       5
    -1.0                0.0            0.0              0       0
   200.51            2745.10          59.83             8       7
   224.53           15623.81         204.75             8       7
   231.83           22258.65         371.68             8       7
    -1.0                0.0            0.0              0       0
   200.69            2732.21          58.09            10       9
   225.08           13266.53         197.45            10       9
   232.13           18466.61         346.78            10       9
    -1.0                0.0            0.0              0       0
   200.79            1433.73          42.52            13      12
   233.31            8023.03         326.04            13      12
   226.04            5616.49         175.44            13      12
    -1.0                0.0            0.0              0       0
   202.38            1281.06          38.28            16      15
   227.74            6033.35         141.33            16      15
   235.58            3682.21         239.83            16      15
    -1.0                0.0            0.0              0       0
   203.39            1056.34          36.03            19      18
   228.97            3204.89         120.49            19      18
   236.53            4606.81         205.68            19      18
[EOB]
```

Table A.II.4b

SIGCALC program output example.

To run the program one types (the underlined terms):

```
ANALYS:: RUNDWSC <CR>
What is this input file name ?
ASMAH83AC.DAT <CR>


         MENU


  C   Start calculation
  F   List to file
  L   List to screen
  P   Plot
  R   Ratio to Rutherford
  S   Show complete data set
  D   List to DWUCK4 file

D <CR>
What is the name for the DWUCK4 file output ?
ASMAH83AC.OUT <CR>


         MENU


  C   Start calculation
  F   List to file
  L   List to screen
  P   Plot
  R   Ratio to Rutherford
  S   Show complete data set
  D   List to DWUCK4 file

C <CR>
SIGCALC is finished.
The results of the calculation are stored in the file called ASMAH83AC.OUT
```

E. PROGRAM EXAMPLE FOR WRITECHEX.

The program WRITECHEX was designed to convert a spectrum which was expressed in terms of counts versus channel number into a spectrum expressed in terms of counts versus excitation energy. This was carried out for all of the spectra that where sliced and used the calibration output of SPECCAL.

Table A.II.5 list the command file that was used on a VAX 11/750 or 11/780 computer for the typical case of converting spectra of the three angles of 2°, 9° and 18° obtained from the reaction $^{144}Sm(\alpha,t)$ using the 96.9 MeV beam. The name of this file is called CHEXASMT.COM. This command file requires file names of spectra to exist in the computer. These names are ASMATB02.SPC,ASMATB09.SPC and ASMATB18.SPC in the subdirectory called [DUFFY.ALPHAT.DATA]. To run this program on the VAX computer one types in (the underlined part):

```
ANALYS:: @CHEXASMT <cr>
```

The output from this program will write the corrected spectra to disk in the subdirectory called [DUFFY.ALPATC.DATA].

Table A.II.5

Program example for WRITECHEX

```
$ SET DEFAULT SYS$ANALYSIS:[DUFFY.ALPHATC.DATA]
$ RUN [DUFFY.PLOTS]WRITECHEX
.04                                          ← Bin size in keV
3                                            ← number of spectra to convert
-1.800, 17.960, 2                            ← Ex. energy inital, final, Θ
2                                            ← indicates a 2nd order polyn.
-0.1139247824E-04                            }
 0.4075623094E-01                            ← coef. of the polyn.
-0.9484177486E+01                            }
-1.800, 17.840, 9
2
-0.1132174469E-04
 0.4050301202E-01
-0.94522145 19E+01
-4.480, 15.280, 18
2
-0.8154951079E-05
 0.3722206994E-01
-0.1161539728E+02
ASMATB
[DUFFY.ALPHAT.DATA]
[DUFFY.ALPHATC.DATA]
[EOB]
```

F. PROGRAM EXAMPLE FOR THE 68K.

Table A.II.6 outlines the steps that are taken to program the 68K data aquisition program for the stripping reaction run.

Table A.II.6

Program example for the 68K

The following is an example for setting up the 68K Data Aquisition system. We will put 2 ADC (AD811's) in slot # 4 and 5 and 2 QDC's (2249W's) in slot # 6 and 7 in the 68K crate.

The first thing to do is to logon to your experiment acc#. Please type the following. And answer the questions asked.

```
$ @[DAQ.68K]VMEIT

→ Create a new command file?(Y/N).......... Y
  ( if N - type [experiment #].68K )
→ Create initial FNA's ? (Y/N) ............ Y

1 - F: 26 ← Enable LAM (see manual for AD811's)
    N: 4  ← Slot # on crate.
    A: 12 ← Address
 NAME: <CR>
      ............................... SAVE?: type ...Y
      ..... at the end it will ask CONTINUE?: type ...Y
Repeat for all FNA's, except at the competion. (see below)
2 - F: 11 ← Clear all registers (see manual for AD811's)
    N: 4
    A: 12

3 - F: 26
    N: 5  ←-----¦ Do the same for the rest of the ADC's ;
    A: 12       ¦
                ¦
4 - F: 11       ¦                5 - F: 26 ← See manual for 2249W's
    N: 5  ←-----                     N: 6
    A: 12                            A: 0
      .... at the completion of this pass. type N after CONTINUE!!
```

The bit part.

We are using only 2 bits. One is for the S320 events and the other one for the monitor (ΔE. E). One ΔE uses a 2249W and the other E uses the other 2249W one had more monitors for bits then adjust the appropriate parameters.

```
        ↓ Type this part.

Bit  1 1
Bit  2 1
Bit  3 0
       .
       .
       .
Bit 16 0
```

Table A.II.6 continued

```
Slots for bit 1 (Mask of LAM's) on left.  Slots for bit 2 on right.
        ↓ Type this part                          ↓ Type this part.

Slot  1 0                                 Slot  1 0
Slot  2 0                                 Slot  2 0
Slot  3 0                                 Slot  3 0
Slot  4 1                                 Slot  4 0
Slot  5 1                                 Slot  5 0
Slot  6 0                                 Slot  6 1
Slot  7 0                                 Slot  7 1
Slot  8 0                                 Slot  8 0
Slot  9 0                                 Slot  9 0
Slot 10 0                                 Slot 10 0
Slot 11 0                                 Slot 11 0
Slot 12 0                                 Slot 12 0
Slot 13 0                                 Slot 13 0
Slot 14 0                                 Slot 14 0
Slot 15 0                                 Slot 15 0
Slot 16 0                                 Slot 16 0

Now the next step is to load commands of Bit 1 in reverse order
Repeat the same procedure as above for programing the FNA's.
1 - F:0 ← Read command for AD811's (see manual)
    N:5 ← Slot #       4 - F:0                 7 - F:0
    A:0                    N:4 SAVE?:Y             N:4 SAVE?:Y
 NAME:<CR>                 A:5                     A:2
                       NAME:<CR>               NAME:<CR>
2 - F:0                5 - F:0                 8 - F:0
    N:4 SAVE?:Y            N:4 SAVE?:Y             N:4 SAVE?:Y
    A:7                    A:4                     A:1
 NAME:<CR>             NAME:<CR>               NAME:<CR>

3 - F:0                6 - F:0                 9 - F:0
    N:4 SAVE?:Y            N:4 SAVE?:Y             N:4 SAVE?:Y
    A:6                    A:3                     A:0
 NAME:<CR>             NAME:<CR>               NAME:<CR>
Don't forget to say N(no) after the CONTINUE? statement!

In reverse order load Bit 2.

1 - F:0
    N:6 SAVE?:Y
    A:1
 NAME:<CR>
2 - F:0
    N:6 SAVE?:Y
    A:0
 NAME:<CR>
```

Table A.II.6 continued

```
 All (event) cycles?  ................................. Y
ext step is to clear FNA's internally for each event cycle.}

 . F: 11 ← Clear command (see AD811 manual)
   N: 4  ← Slot #
   A: 12
AME: <CR>
 . F: 11
   N: 5 SAVE?: Y
   A: 12
NAME: <CR>
e sure that you type in N(no) for the CONTINUE statement.
o  FNA's  are  needed  to clear Slot # 6 which is for the 2249W's (QDC's).  The
lear is done externally.

. Do you want FNA's for the end of valid cycles only? ... N

. Save Run? (i.e. this pass?)  ......................... Y
```

REFERENCES

[Aa82] E.H.L. Aarts, R. Malfliet, S.Y. van der Werf and R.J. de Meijer, Nucl. Phys. **A380**, 465 (1982).

[Aa84] E.H.L. Aarts, R.A.R.L. Malfliet, R.J. de Meijer and S.Y. van der Werf, Nucl. Phys. **A425**, 23 (1984).

[Au70] N. Austern, "Direct Nuclear Reaction Theories" (John Wiley and Sons, 1970).

[Be69] P.R. Bevington, "Data Reduction and Error Analysis for the Physical Sciences", (McGraw Hill, 1969) p. 89

[Be79] G.F. Bertsch, P.F. Bortignon, R.A. Broglia and C.H. Dasso, Phy. Lett. 80B, 161 (1979).

[Be83a] G.F. Bertsch, P.F. Bortignon, R.A. Broglia and C.H. Dasso, Rev. Mod. Phys. 55, 287 (1983).

[Be83b] G.F. Bertsch, Scientific American, May 1983, page 70.

[Be86] G.F. Bertsch, private communication, 1986.

[Bl53] J.M. Blatt and V.F. Weisskopf, "Theoretical Nuclear Physics" (John Wiley and Sons, 1953) p. 324.

[Bo69] A. Bohr and B.R. Mottelson, "Nuclear Structure", Vol 1 (Benjamin,1969) p. 432.

[Bo75a] A. Bohr and B.R. Mottelson, "Nuclear Structure", Vol 2 (Benjamin,1975) p. 422.

[Bo75b] W. Booth and S. Wilson, Nucl. Phys. **A247**, 126 (1975).

[Co69] M. Conjeand, S. Harar and E.Thuriere, Nucl. Phys. **A129**, 10 (1969).

[Cr80] G.M. Crawley, in Proc. Int. Conf. on Structure of Medium-Heavy Nuclei, Osaka, Japan (1980) p. 590.

[Dj77] A. Djaloeis, J.P. Didelez, A. Galonsky and W. Oelert, Annual Report of Kernforschungsanlage Julich, 1977, p. 2.

[Fr77] E. Friedman, A. Moalem, D. Suraqui and S. Mordechai, Phys. Rev. **C15**, 1604 (1977).

[G1-1] Ref. [Co69,He74,Se77,We77,Cr80,Ge80,Sa81,Ga81, Ga83]

[G1-2] Ref. [Ga82b,Ga84,Ga85a,Ga85b]

[Ga81] S. Galès, Nucl. Phys. **A354**, 193c (1981).

[Ga82a] S. Galès, G.M. Crawley, D. Weber and B. Zwieglinski, Nucl. Phys. **A351**, 173 (1982).

[Ga82b] S. Galès, C.P. Massolo, S. Fortier, E. Gerlic, J. Guillot, E. Hourani, J.M. Maison, J.P. Schapira and B. Zwieglinski, Phys. Rev. Lett. **48**, 1593 (1982).

[Ga83] S. Galès, G.M. Crawley, D. Weber and B. Zwieglinski, Nucl. Phys. **A398**, 19 (1983).

[Ga84] S. Galès, Journal de Physique, C4, March 1984.

[Ga85a] S. Galès, C.P. Massolo, S. Fortier and J.P. Schapira, Phys. Rev. **C31**, 94 (1985).

[Ga85b] S. Galès, in Int. School of Nuclear Structure, Alushta, USSR Oct 1985, IPN Report IPNO-DRE/85-31.

[Ge70] C.F. Gerald, "Applied Numerical Analysis", (Addison-Wesley, 1970) p. 284.

[Ge80] E. Gerlic, G. Berrier-Ronsin, G. Duhamel, S. Galès, E. Hourani, H. Langevin-Joliot, M. Vergnes and J. Van de Wiele, Rhys. Rev **C21**, 124 (1980).

[Go72] U. Gotz, H.C. Pauli, K. Alder and K. Junker, Nucl. Phys. **A192**, 1 (1972).

[He74] W.H.A. Hessenlinck, B.R. Kooistra, L.W. Put, R.H. Siemssen and S.Y. van der Werf, Nucl. Phys. **A226**, 229 (1974).

[Ko74] D.G. Kovar, N. Stein and C.K. Bockelman, Nucl. Phys. **A231**, 266 (1974).

[Ko85] N. Koori, T. Ohsawa, S. Seki, H. Yokota, T. Yanabu, Y. Deschamps, E. Hourani, H. Langevin-Joliot, F. Reide and M. Roy-Stéphan, Phys. Rev. C31, 246 (1985).

[Ku69] P.D. Kunz, University of Colorado, program DWUCK4 (1969) unpublished.

[Ku84] P.D. Kunz, private communication, 1984.

[La82] H. Langevin-Joliot, E. Gerlic, J. Guillot, M. Sakai, J. van de Wiele, A. Devaux, P. Force and G. Landaud, Phys. Lett. 114B, 103 (1982).

[Ma69] M.H. Macfarlane, in Proceedings of the International Conference on Properties of Nuclear States, Montreal, 1969, p. 385.

[Ma76] L.A. Malov and V.G. Soloviev, Nucl. Phys. **A270**, 87 (1976).

[Ma77] M.J. Martin, Nucl. Data Sheets 22, 545 (1977).

[Ma86] L.A. Malov, N.D. Vinh and V.G. Soloviev, preprint (1986).

[Me85] R.J. de Meijer, Rev. Mod. Phys. <u>57</u>, 147 (1985).

[Mo71] E.J. Moniz, I. Sick, R.R. Whitney, J.R. Ficenec, R.D. Kephart and W.P. Trower, Phys. Rev. Lett. 26, 445 (1971).

[Ol65] G.G. Ohlsen, Nucl. Inst. and Meth. **37**, 240 (1965).

[Pe81] R. Perry, A. Nadasen, D.L. Hendrie, P.G. Roos and N.S. Chant, Phys. Rev. **C24**, 1471 (1981).

[Sa81] H. Sakai, R.K. Bhowmik, K. van Dijk, A.G. Drentje, M.N. Harakeh, Y. Iwasaki, R.H. Siemssen, S.Y. van der Werf and A. van der Woude, Phys. Lett. 103B, 309 (1981).

[Sa85] H. Sakai, R.K. Bhowmik, S. Brandenburg, J.H. van Dijk, A.G. Drentje, M.N. Harakeh, Y. Iwasaki, R.H. Siemssen, S.Y. van der Werf and A. van der Woude, Research Center for Nuclear Physics, Osaka University, RCNP85-1.

[Sc80] O. Scholten, M.N. Harakeh, J. van der Phicht, L.W. Put, R.H. Siemssen and S.Y. van der Werf, Nucl. Phys. **A348**, 301 (1980).

[Sc82] O. Scholten and N. Blasi, Nucl. Phys. **A380**, 509 (1982).

[Sc85] O. Scholten, private communication, 1985.

[Se77] M. Sekiguchi, Y. Shida, F. Soga, Y. Hirao and M. Sakai, Nucl. Phys. **A278**, 231 (1977).

[Se47] R. Serber, Phys. Rev. 72, 1008(1947).

[Se85] B. Seligmann, J. Ernst, J. Kleinfeller, K. Keller, L. Lassen, W. Lucking, R. Schreck and H. Gemmeke, Phys. Lett. 157B, 345 (1985).

[Sh85] B.M. Sherrill, Ph.D. Thesis (Michigan State University, Department of Physics, 1985), unpublished.

[So80] V.G. Soloviev, Ch. Stoyanov, and A. I. Vdovin, Nucl. Phys. **A342**, 261 (1980).

[St79] O. Straum, G. Lovhoiden, D.G. Burke, E.R. Flynn and J.W. Sunier, Z. Phys. **A293**, 75 (1979).

[St83] Ch. Stoyanov and A.I. Vdovin, Phys. Lett. 130B, 134 (1983).

[Tu80] J.K. Tuli, Nucl. Data Sheets **B29**, 533 (1980), A=145, and references therin.

[Va85a] H. van der Plicht, private communication, 1985.

[Va85b] A. Vander Molen, R. Au, R. Fox and T. Glynn, Nucl. Inst. and Meth. A236, 359 (1985).

[Vi70] C.M. Vincent and H.T. Fortune, Phys. Rev. **C2**, 782 (1970).

[Wa77] A.H. Wapstra and K. Bos, At. Data Nucl. Data Tables **19**, 215 (1977).

[We77] S.Y. van der Werf, M.N. Harakeh, L.W. Put, O. Scholten and R.H. Siemssen, Nucl. Phys. **A289**, 141 (1977).

[Wo72] P.B. Woollam, R.J. Griffiths, F.G. Kingston, C.B. Fulmer, J.C. Hafele and A. Scott, Nucl. Phys. **A179**, 657 (1972).

[Wu79] J.R. Wu, C.C. Chang, H.D. Holmgren and R.W. Koontz, Phys. Rev. **C20**, 1284 (1979)